SPATIOTEMPORAL ANALYSIS OF A TURBULENT THERMOACOUSTIC SYSTEM USING COMPLEX NETWORKS

A THESIS

submitted by

ABIN KRISHNAN

for the award of the degree

of

DOCTOR OF PHILOSOPHY

DEPARTMENT OF AEROSPACE ENGINEERING

INDIAN INSTITUTE OF TECHNOLOGY MADRAS

NOVEMBER 2018

विद्या ददाति विनयं विनयाद्याति पात्रताम् ।
पात्रत्वाद्धनमाप्रोति धनाद्धर्मं ततः सुखम् ॥

Knowledge makes you humble; humility gives you character; good character attracts wealth; from wealth (one does) good deeds; from that (comes) joy.

(Taken from *Vidya prashamsa*, Subhashita-ratna-bhandagara)

To amma, acha, abiloosu and bhajji

ACKNOWLEDGEMENT

ABSTRACT

KEYWORDS: Thermoacoustic instability; turbulent reactive flow; complex networks; vortex-vortex interaction; emergence; critical regions; passive control.

The interaction between unsteady combustion and the acoustic field in a combustor is inevitable in many confined engineering systems such as boilers, rocket engines, and gas turbine engines. Such an interaction manifests as high amplitude self-excited oscillations when the energy added from the unsteady combustion to the acoustic field of the confinement overcomes the acoustic losses in the system. This phenomenon is known as thermoacoustic instability. We encounter thermoacoustic instability in simple household devices such as boilers and heat exchangers, gas turbine engines used for propulsion and power generation as well as in high-end rocket engines, ramjets and afterburners used in defence applications. Thermoacoustic instability engenders violent vibrations which damage the sensors, increases thermal stresses to combustor walls, induce fatigue failure of components, trigger flame blow-off and flashback, leading to costly shutdowns or catastrophic failure of the engine components and probably the entire mission. Even after decades of active research, understanding the physical mechanisms underlying the spontaneous excitation of self-sustained oscillations as well as their mitigation continues to attract researchers from all over the world.

Most of the early studies examined the temporal dynamics of the acoustic pressure and the global heat release rate oscillations during the transition to thermoacoustic instability from a state of stable combustor operation (also known as combustion noise in the community). These studies led to two major findings in the case of turbulent

combustors. The first one is the discovery of an intermediate state, called intermittency, between the states of combustion noise and thermoacoustic instability. The second one is the description of the onset of thermoacoustic instability as a mutual synchronization between the acoustic field and the reactive flow in the turbulent combustor. Further, the phenomenon of thermoacoustic instability involves the complex and highly non-linear interplay of three main subsystems, namely the acoustic field, the hydrodynamics and the flame dynamics, leading to rich spatiotemporal dynamics during the transition to thermoacoustic instability. Thus, the analysis of the spatiotemporal dynamics leading to thermoacoustic instability is vital in unmasking the underlying mechanisms and devising efficient control strategies for its mitigation.

A turbulent flow induces a large number of degrees of freedom to a thermoacoustic system. The rich spatiotemporal dynamics exhibited by a turbulent thermoacoustic system is a result of the interaction amongst many processes such as molecular mixing, turbulent transport, chemical kinetics and acoustic waves operating over a range of length and time scales. This prompts us to consider a turbulent thermoacoustic system as a complex system. Complex network is one of the efficient approaches to study complex systems. The present thesis investigates the spatiotemporal dynamics of a turbulent thermoacoustic system during the intermittency route to thermoacoustic instability using complex networks.

In turbulent combustors, the transition from a state of stable operation (i.e., combustion noise) to the unstable state (thermoacoustic instability) occurs via intermittency. During stable combustion, the acoustic power production happens in a spatially incoherent manner. In contrast, during thermoacoustic instability, the acoustic power production

happens in a spatially coherent manner. In the present study, we investigate the spatiotemporal dynamics of acoustic power sources during the intermittency route to thermoacoustic instability. To that end, we perform simultaneous acoustic pressure measurement, high-speed chemiluminescence and high-speed particle image velocimetry (PIV) in a backward facing step combustor with a bluff body stabilized flame at different equivalence ratios. We examine the spatiotemporal dynamics of acoustic power sources by constructing time-varying spatial networks during the different dynamical states of combustor operation. We uncover that as the turbulent combustor transitions from combustion noise to thermoacoustic instability via intermittency, small fragments of acoustic power sources observed during combustion noise, nucleate, coalesce and grow in size to form large clusters at the onset of thermoacoustic instability. This nucleation, coalescence and growth of small clusters of acoustic power sources occur during the growth of pressure oscillations during intermittency. On the contrary, during the decay of pressure oscillations during intermittency, these large clusters of acoustic power sources disintegrate into small ones. We use network measures such as the link density, the number of components and the size of the largest component to quantify the spatiotemporal dynamics of acoustic power sources as the turbulent combustor transits from combustion noise to thermoacoustic instability via intermittency.

We characterize the vorticity interactions occurring during the different dynamical states of combustion noise, intermittency and thermoacoustic instability by constructing time-varying weighted spatial networks based on Biot-Savart law. Biot-Savart law gives the magnitude of the velocity induced by vortices at different locations in the flow field. We observe that the topology of the network is scale-free during combustion noise

as well as during the periodic and aperiodic epochs of intermittency. However, we find that the network topology oscillates between random and scale-free behaviour during an acoustic cycle of thermoacoustic oscillations. Thus, as the turbulent thermoacoustic system transitions from combustion noise to thermoacoustic instability, we observe that the topology of the vorticity network changes from scale-free to an oscillation between random and scale-free.

Next, a spatial network is constructed, representing each of the three dynamical regimes of combustor operation, based on the correlation between the time series of local velocity obtained from PIV. Network centrality measures enable us to identify critical regions of the flow field during combustion noise, intermittency and thermoacoustic instability. We find that during combustion noise, the bluff body wake turns out to be the critical region that determines the dynamics of the combustor. As the combustor dynamics transitions to thermoacoustic instability, the bluff body wake loses its significance in determining the flow dynamics and two regions emerge as the most critical regions controlling the spatiotemporal dynamics during thermoacoustic instability. These regions are (a) the region on top of the bluff body and (b) the region on top of the bluff body shaft, just downstream of the dump plane.

Finally, we perform passive control experiments with an aim to suppress thermoacoustic oscillations by injecting air micro-jets at the top and the bottom walls of the combustor. We obtain efficient suppression with micro-jet injection at the critical regions identified by the spatial network analysis, as mentioned above. We could achieve 85% suppression in p'_{rms} with injection at the region on top of the bluff body shaft. Hence, we find that complex network analysis provides a smart and effective way

to mitigate thermoacoustic instability by identifying the ideal locations for the passive control injection, which we otherwise obtain after innumerable time consuming and expensive trials.

TABLE OF CONTENTS

LIST OF FIGURES

5.1 The spatial distribution of the node strengths of (b) the $p'\dot{q}'$ network and (c) the vorticity network at the corresponding time instants (A, B, C and D) marked on (a) the time series of fluctuating pressure during *combustion noise*. The blue region in the spatial distribution of the node strength of the acoustic power $(p'\dot{q}')$ network represents local acoustic power sinks. The colourbar in (b) represents the magnitude of the node strength, which indicates the average acoustic power produced in the neighbourhood of a node. The spatial distribution of the node strength shows that acoustic power production happens in small disconnected fragments during combustion noise. In the vorticity network (c), the node strength indicates the average vorticity in the neighbourhood of a node. Positive values of node strength represents vorticity distribution in the anti-clockwise direction whereas, negative node strength indicates the vorticity distribution in the clockwise direction. Velocity vectors are superimposed on the vorticity network to understand the flow field better. Small vortices are present in the outer shear layer as well as they are being shed from the tip of the bluff body. The grey colour rectangles in the subplots represent the bluff body. 80

5.2 The spatial distribution of the node strengths of (b) the acoustic power network and (c) the vorticity network at the corresponding time instants (A, B, C, D and E) marked on (a) the time series of oscillating pressure during *thermoacoustic instability*. The spatial distribution of the node strength of the acoustic power network indicates that during thermoacoustic instability, the acoustic power production occurs in large clusters. The high values of positive node strength of the vorticity network coincide with the centre of the coherent structure formed downstream of the dump plane. The maximum acoustic power production occurs when the coherent structure impinges on the top wall of the combustor (C). The 82

magnitude of acoustic power production during thermoacoustic instability is almost three orders of magnitude higher than that during combustion noise as indicated by the node strength of the acoustic power network.

5.3   The spatial distribution of the node strengths of (b) the acoustic power network and (c) the vorticity network at the corresponding time instants (A, B, C, D and E) marked on (a) the time series of fluctuating pressure during the *aperiodic regime of intermittency*. The acoustic power production happens in small fragmented clusters as in the case of combustion noise.   85

5.4   The spatial distribution of the node strengths of (b) the acoustic power network and (c) the vorticity network at the corresponding time instants (A, B, C, D and E) marked on (a) the time series of fluctuating pressure during the *periodic regime of intermittency*. The acoustic power production occurs in large clusters as in the case of thermoacoustic instability. However, unlike the case during thermoacoustic instability, the coherent structure impinges the rear-end tip of the bluff body. After impingement, the coherent structure disintegrates into small vortices that convect over the top of the bluff body.   86

5.5   The spatial distribution of the node strengths of (b) the acoustic power network and (c) the vorticity network at the corresponding time instants (A, B, C, D, E and F) marked on (a) the time series of fluctuating pressure during the *growth of pressure oscillations observed during intermittency*. As the thermoacoustic system transits from low amplitude aperiodic oscillations to high amplitude periodic oscillations during intermittency, the acoustic power sources nucleate, coalesce and grow in size and strength of acoustic power production also increases.   87

root mean square (rms) value of the acoustic pressure as the thermoacoustic system transits from combustion noise to thermoacoustic instability via intermittency. The dashed vertical lines divide the parameter space, i.e., the equivalence ratio (φ), into regimes of combustion noise, intermittency and thermoacoustic instability respectively.

the dump plane (b, B to D). Regions with very high node strength coincides mainly with regions of high vorticity in these coherent structures. The power law exponents (d) suggest that the vorticity network during a high amplitude periodic burst is scale-free.

6.4   The spatial distribution of (c) the node strength (s) of the vorticity network at different time instants (A-E) of an acoustic cycle (a) during thermoacoustic instability. The velocity vectors and the vorticity field corresponding to the points is shown in (b). The magnitude of the vorticity field and the node strength is one order of magnitude higher than that during combustion noise. Regions with high node strength corresponds to regions with high vorticity in the coherent structure (A and B) as well as in the large vortex shed from the tip of the bluff body (C and D). The power law exponents (d) suggest an oscillation between random and scale-free networks during thermoacoustic oscillations.

7.1   The schematic of the flow field divided into three distinct regions. 'A' represents the wake of the dump plane. The region between the outer shear layer (O.S.L) and inner shear layer (I.S.L) is marked as region 'B' and the bluff body wake is indicated as 'C'. This distinction helps one for the better description of the distribution of network measures in the flow field.

7.2   Spatial distribution of degree, local clustering coefficient, betweenness centrality and closeness centrality during combustion noise, intermittency and thermoacoustic instability. During combustion noise, the wake of the bluff body emerges as the critical region. At the onset of thermoacoustic instability, the wake of the bluff body loses its importance and the shear zone emerges as the critical region.

A3   The variation of link density at different values of threshold Pearson's correlation coefficient for combustion noise, intermittency and thermoacoustic instability. We chose 0.25 as the threshold Pearson's correlation coefficient for network construction as at this value of Pearson's correlation coefficient, the variation in link density across the three states of combustor operation is maximum. Maximum variation in link density ensures maximum variation in the spatial distribution of network properties thus helping us to discern the critical regions during the three states of combustor operation.   150

ABBREVIATIONS

FDF	flame describing function
FTF	flame transfer function
FWHM	full width at half maximum
LPG	liquefied Petroleum Gas
NOx	oxides of nitrogen
PIV	particle image velocimetry
PLIF	planar laser induced fluorescence
R.O.I	region of interest
rms	root mean square
SLPM	standard litre per minute
w.c.c	weighted closeness centrality
w.l.c.c	weighted local clustering coefficient

NOTATIONS

Upper-case Roman

A_{ij}	Element of an adjacency matrix
C_i	Clustering coefficient of a node i
R_{ij}	Element of a recurrence matrix
R_p	Pearson's correlation coefficient
E	Efficiency of a network
L	Characteristic path length of a network
G	Gain
H	Hurst exponent
$P(k)$	Degree distribution
T	Transitivity of a network
$X(t)$	Phase space vector
Re	Reynolds number

Lower-case Roman

$\dot{m}_a$	Mass flow rate of air
$\dot{m}_f$	Mass flow rate of the fuel
$\dot{q}'$	Unsteady heat release rate fluctuation
$\dot{q}'_{rms}$	Root mean square value of heat release rate fluctuation
b_i	Betweenness centrality of a node i
c_i	Closeness centrality of a node i
d_{ij}	Shortest path between the nodes i and j
k_i	Degree of a node i
n_i	Neighbourhood of a node i
$\hat{p}$	Pressure amplitude
p'	Acoustic pressure fluctuation
$p'\dot{q}'$	Local acoustic power source
p'_{rms}	Root mean square value of acoustic pressure fluctuation

$\bar{q}$	Mean heat release rate
s_i	Node strength of a node i
$\hat{u}$	Velocity amplitude
$\bar{u}$	Upstream flow velocity
u'	Velocity fluctuation
$u_{i \rightarrow j}$	Velocity induced by fluid element at node i on another one at node j
v_a	Velocity of the air
v_j	Velocity of the jet
w_{ij}	Weight of the link between nodes i and j
x_f	Flame location
N	Number of clusters in a network
S	Size of the largest cluster in a network
e	An edge of the network
f	Frequency
i	A node of the network
n	Number of nodes of the network

Greek

$\emptyset$	Phase
γ	Power law exponent
ε	Recurrence threshold
φ	Equivalence ratio
ϵ	Threshold for connectivity in local acoustic power network
ρ	Link density of a network
ω	Vorticity

Miscellaneous

$|x|$	Absolute value of x
$\|*\|$	Euclidean norm

CHAPTER 1

INTRODUCTION

In most practical applications, such as in power generation and aerospace industries, combustion happens in a confined space. Inherently, these combustion processes are unsteady and unsteady combustion tends to drive the acoustic modes of the confinement (Hegde, Reuter and Zinn 1988). As a consequence, combustors are susceptible to the phenomenon of thermoacoustic instability (also known as combustion instability), which occurs when a positive feedback is established between the acoustic field and the heat release rate oscillations (Figure 1.1). Thermoacoustic instability, which is characterized by large amplitude pressure oscillations, can lead to the failure of system components due to increased mechanical and thermal stresses (McManus, Poinsot and Candel 1993; Candel 2002, Lieuwen and Yang 2005, Juniper and Sujith 2018). Lord Rayleigh (1878) explained that acoustic energy is added to the system if the heat release rate fluctuations occur in phase with the pressure oscillations. When the acoustic driving overcomes the damping present in the system, the combustor dynamics transitions to thermoacoustic instability (Putnam 1971).

The coupling amongst acoustics, hydrodynamics and flame dynamics during thermoacoustic instability leads to complex spatiotemporal dynamics. The complex behaviour of a thermoacoustic system, involving different length and time scales, arises due to different factors such as molecular mixing, turbulence, chemical kinetics, acoustic and flame-flow interactions. Hence, the analysis of the spatiotemporal

dynamics leading to thermoacoustic instability is vital in understanding the underlying mechanisms and devising control strategies for its mitigation.
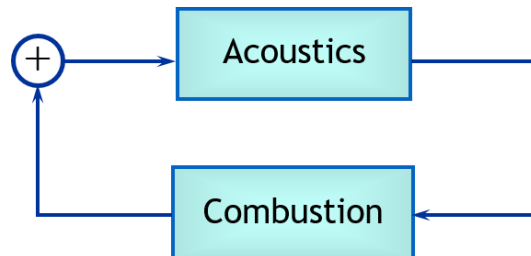
Figure 1.1: A schematic diagram showing the positive feedback loop between the acoustic field and the unsteady heat release rate oscillations, which is a necessary condition for the occurrence of thermoacoustic instability. When the acoustic driving overcomes the damping in the system, onset of thermoacoustic oscillations set in.

Early studies focused on the transition from stable combustion (known as combustion noise (Strahle 1971) in the community) to unstable combustion (thermoacoustic instability) by primarily examining the acoustic pressure measurements at different regimes of combustor operation. Traditionally, the transition to thermoacoustic instability is considered as a Hopf bifurcation (Lieuwen 2002). This viewpoint works well for laminar combustors. However, for turbulent combustors, this description may be incomplete.

In a turbulent combustor, the transition from a state of combustion noise to thermoacoustic instability occurs via a dynamical state called intermittency (Nair, Thampi and Sujith 2014; Gotoda *et al.* 2014; Domen *et al.* 2015; Sampath and Charavarthy 2016; Wilhite *et al.* 2016; Kheirkhah *et al.* 2017; Ebi *et al.* 2017). Combustion noise is characterized by low amplitude aperiodic pressure oscillations. The emergence of high amplitude periodic pressure oscillations, also known as limit cycle oscillations, marks the onset of thermoacoustic instability. Intermittency, the in-

between state, has the signature of both combustion noise and thermoacoustic instability. It is characterized by bursts of high amplitude periodic oscillations sandwiched between regimes of low amplitude aperiodic fluctuations, in an apparently random manner.

Intermittency can be viewed, in simple terms, as a tug of war between the acoustic driving and the acoustic damping present in the system. As the acoustic driving wins over the damping, the growth of the acoustic pressure oscillations occurs and whenever the damping overtakes the driving, these high amplitude acoustic pressure oscillations start to decay. It is this competition between the acoustic driving and the damping, which leads to the emergence of bursts of high amplitude seemingly periodic oscillations in the background of low amplitude aperiodic pressure fluctuations during intermittency. The presence of intermittency en route to thermoacoustic instability has enabled researchers to device precursors (Nair *et al.* 2012), which will be discussed in section 1.5.1.2.

Recently, synchronization theory has been used to explore the coupling between the acoustic pressure and the unsteady heat release rate fluctuations during the intermittency route to thermoacoustic instability (Pawar *et al.* 2017). They described the transition to thermoacoustic instability as a mutual synchronization of two non-identical oscillators namely, the acoustic field of the combustor and the heat release rate oscillations. During intermittency, the authors observed intermittent phase synchronization, wherein the oscillators are synchronized during the periodic epochs and desynchronized during the aperiodic epochs of their oscillations.

In the past, there have been studies that examined the spatiotemporal dynamics during the transition to thermoacoustic instability. Most of these studies, however, focused on the spatiotemporal dynamics only during combustion noise and thermoacoustic instability. These studies elucidated the emergence of large-scale coherent structures at the onset of thermoacoustic instability and the modification of the flame dynamics by these flow structures (Rogers and Marble 1956; Smith and Zukoski 1985; Poinsot *et al.* 1987; Schadow and Gutmark 1992; Coats 1996; Renard *et al.* 2000, Shanbhogue 2008; Schwing, Sattelmayer and Noiray 2011; Emerson *et al.* 2012).

Recently, there have been a few studies that focussed on the spatiotemporal dynamics during the intermittency route to thermoacoustic instability. Mondal *et al.* (2017), by calculating the instantaneous phase between the acoustic pressure and the unsteady heat release rate fluctuations, examined the spatial distribution of the acoustic power sources in the flow field during the three different dynamical states of combustor operation, namely combustion noise, intermittency and thermoacoustic instability. During combustion noise, the authors observed that the acoustic power production occurs in a spatially incoherent manner. In contrast, during thermoacoustic instability, the acoustic power production occurred in a spatially coherent manner over large regions. However, during intermittency, both incoherent and coherent patches of acoustic power sources coexisted simultaneously, resembling a chimera-like state.

Most of the aforementioned studies focussed on the flow and flame dynamics during thermoacoustic instability. These studies emphasized the formation of large coherent structures during thermoacoustic instability. However, there does not seem to be any study, till date, which brought to light the relative importance of different regions in a turbulent reactive flow field in determining the spatiotemporal dynamics during the

intermittency route to thermoacoustic instability. Also, till date, studies have not focussed on describing how the emergence of large regions of spatially coherent acoustic power sources occur at the onset of thermoacoustic instability from a state of spatially incoherent acoustic power production observed during combustion noise. The present study tries to find answers to the above questions by examining the spatiotemporal dynamics during the intermittency route to thermoacoustic instability in a turbulent combustor using complex networks.

Control of thermoacoustic instability, despite decades of research, still attracts the attention of researchers. There are two different approaches that aim at the mitigation of thermoacoustic instability, namely active and passive control. Active control uses a closed-loop feedback mechanism involving electro-mechanical components, which, in turn, adds complexity to the design of combustors. Hence, the feasibility of active control in practical combustors is limited. Passive control involves either increasing the dissipation of acoustic energy using acoustic liners, baffles and Helmholtz or quarter wave resonators or reducing the efficiency of acoustic driving by changing the injector geometry and the flame dynamics. Passive control measures, compared to that of active control, are simple and hence find applications in real combustors. However, most of the passive control strategies are decided based on a multitude of trials. These trials are very time consuming, cost-intensive and hence unprofitable. In the present work, we propose a smart and efficient way to mitigate thermoacoustic instability by identifying the ideal location for injection of micro-jets to suppress thermoacoustic oscillations, using the framework of network analysis.

1.1   HISTORICAL OVERVIEW OF THERMOACOUSTIC INSTABILITY

About ten years after the discovery of hydrogen, in 1777, Higgins reported the first observation of sound by a flame (Higgins 1802). He was demonstrating the production of water from the burning of hydrogen. A musical tone was heard when he lowered a vertical glass tube, closed at the upper end, over the flame. Sondhauss (1850), performed a systematic investigation of sound production by heat. He conjectured a relation between the time period of oscillations and the dimension of the apparatus but, could not give an explanation for the production of sound.

In 1859, Rijke performed experiments in a vertical tube, open at both ends, with a piece of metallic gauze stretching across the lower part of the tube (Rijke 1859). The gauze was heated until it became red hot. He heard an audible sound, which lasted for a few seconds as soon as the flame was withdrawn. When the wire gauze was continuously heated by an electric current, the sound sustained. He suggested that the production of sound was related to the through draught created by the heating of the air packet near the wire gauze. This explanation was too simplistic and could not satisfactorily give the reason for the production of sound.

Today, this simple apparatus, known as the Rijke tube, serves as a prototypical system to study the interaction of sound and flame. This field of science is now popularly known as thermoacoustics and the systems used for their study are called thermoacoustic systems.

Lord Rayleigh, in 1878, formulated a criteria, which explained how acoustic waves could be excited and sustained by heat addition (Rayleigh 1878). Today, this is known

as the Rayleigh criteria and is considered as the necessary condition for the occurrence of thermoacoustic instability. Rayleigh's criteria in his own words is stated as follows:

"If the heat be periodically communicated to, and abstracted from, a mass of air vibrating (for example) in a cylinder bounded by a piston, the effect produced will depend upon the phase of the vibration at which the transfer of heat takes place. If heat be given to the air at the moment of greatest condensation, or taken from it at the moment of greatest rarefaction, the vibration is encouraged. On the other hand, if heat be given at the moment of greatest rarefaction, or abstracted at the moment of greatest condensation, the vibration is discouraged."

The dawn of jet and rocket propulsion rekindled the phenomenon of production of sound by a flame. Thermoacoustic instability was encountered for the first time in solid and liquid rocket motors in the late 1930's and early 1940's. In the 1950's, high-frequency thermoacoustic oscillations, known as screech, were reported in high-performance combustion systems such as afterburners and ramjet engines (Culick 2006). Thermoacoustic instability received the greatest limelight during the cold war when the race was on to send a man to the moon; the failure of F1 engine during the Apollo programme in the 1960's being an important case study (Oefelein and Yang 1993). Thermoacoustic instability in gas turbine engines started to receive attention in recent years due to the stringent environmental regulations to reduce NOx emissions, which is a major atmospheric pollutant. Oxides of nitrogen are formed when burning of fuel happens in rich or near stoichiometric conditions. One of the popular approaches to reduce NOx emissions is to operate the gas turbine engines in lean premixed pre-vapourized (LPP) condition (Correa 1993). In lean conditions, the flame is highly

unstable and hence these gas turbine engines are also prone to thermoacoustic instability (Lieuwen and Yang 2005).

Combustion in these systems involves very high power densities of the order of GW/m^3. A small fraction of this energy is sufficient to excite and sustain large amplitude acoustic waves inside the combustion chamber (Sujith, Juniper and Schmid 2016). These self-excited oscillations have many undesirable consequences such as increased structural vibrations, increased heat transfer, flame blow out, flashback and in extreme cases the sudden failure of components or space mission failures (Suresh 1998). Thermoacoustic oscillations, in general, has been identified in these combustion systems in various modes – longitudinal (Culick 2006), transverse (O'Connor, Acharya and Lieuwen 2015) and azimuthal (Worth and Dawson 2013). Even after decades of research, understanding the origin, control and prediction of these thermoacoustic instabilities still continues to attract researchers from all over the world.

1.2   WHAT CAUSES THERMOACOUSTIC INSTABILITY?

Thermoacoustic instability occurs when the heat release rate oscillations are in phase with pressure oscillations, which is now popularly known as the Rayleigh's criteria. It is the unsteady heat release rate that feeds the acoustic field. In the case of solid rocket motors, it is the unsteady burn rate of the propellant, which mainly causes the unsteady heat release (Culick and Yang 1995). When the unsteady heat release rate occurs in phase with the acoustic oscillations, energy is added to the acoustic field. Large amplitude pressure oscillations will arise in solid rocket motors if the acoustic driving overcomes the damping in the system. The relevant dynamics that cause unsteady heat release rate oscillations in combustion systems are enlisted below.

1.2.1 Flame Area Fluctuations

In a premixed flame, the heat release rate is proportional to flame surface area. A laminar flame may become unstable and wrinkle under instabilities such as the Darrieus-Landua instability (Landau 1944) and thermal-diffusive instabilities (Shivashinsky 1977). Wrinkling significantly increases the flame surface area and hence the reaction rate. When the oscillating heat release rate is in phase with the acoustic oscillations, a positive feedback loop is established. Due to this, energy is added to the acoustic field, which on overcoming the damping present in the system, manifests as large amplitude periodic pressure oscillations.

Flieifl *et al.* (1996) observed analytically that a laminar flame behaves as a high pass filter. This means that high-frequency velocity perturbations pass through the flame without significantly altering the heat release rate. Whereas, the low-frequency oscillations, strongly wrinkles the flame and thus, has a pronounced effect on the heat release rate oscillations. Shanbhogue (2008) performed a detailed experimental investigation of the response of bluff body stabilized flames to longitudinal acoustic forcing. The disturbances in the flame front, in response to the external forcing, propagated along the flame at a velocity of the order of the mean velocity. The spacing between the flame structures increased with the increase in the velocity of the approach flow. Downstream of the flame holder, the flame response increased, reached a maximum and then decayed. This behaviour of the flame is a function of the amplitude and frequency of forcing. For identical excitation, it was observed that flame response (the flame front fluctuations) was higher for lower frequencies and the decay rate was faster for higher frequencies. As the amplitude of excitation was increased, the flame front fluctuations also increased but the response decreased with an increase in the

frequency which shows that the flame behaves as a low pass filter to external forcing. The key processes controlling the flame response were identified as (i) flame anchoring, (ii) excitation of the flame front wrinkles by the oscillating velocity field and (iii) flame propagation normal to itself. The first two factors control the growth rate while the decay rate is controlled by the flame propagation as it smoothens the wrinkles. The influence of the flame surface area variations on thermoacoustic instability was experimentally demonstrated by Santavicca and co-workers (1999, 2000, and 2003). They used OH-PLIF imaging to characterize the flame area changes during thermoacoustic instability.

1.2.2   Equivalence Ratio Fluctuations

Equivalence ratio fluctuations are identified as one of the major causes of unsteady heat release rate oscillations, especially at lean conditions. This is due to the fact that the gradient of the chemical reaction time with respect to equivalence ratio increases remarkably as the flame gets leaner (Zukoski 1978). The chemical reaction time is inversely proportional to the reaction rate. Hence, a small variation in the equivalence ratio at lean conditions can lead to large fluctuations in the heat release rate oscillations. Lieuwen, Neumeier and Zinn (1998), using a well-stirred reactor model, demonstrated this high sensitivity of reaction rate to equivalence ratio oscillations at lean conditions.

Equivalence ratio fluctuations arise mainly because of the fluctuation in the fuel and air mass flow rates (Richards and Janus 1997; Lieuwen and Zinn 1998; Richards, Janus and Robey 1999; Lieuwen *et al.* 2001). Acoustic perturbations travel upstream from the combustion chamber and modulate the air and fuel flow rates leading to equivalence ratio fluctuations. These disturbances convect downstream into the combustion zone

resulting in fluctuating heat release. A feedback loop is thus created, leading to the onset of thermoacoustic instability.

1.2.3   Role of Coherent Structures

Many of the early studies have focussed on the emergence of coherent structures at the onset of thermoacoustic instability. Kaskan and Noreen (1955) reported the shedding of vortices downstream of a single flame holder during the high-frequency transverse mode thermoacoustic instability. Elias (1959) observed shedding of coherent vortices from the tips of multiple flame holders during higher modes of transverse thermoacoustic instability. Rogers and Marble (1956), through their experimental study, presented a mechanism for high-frequency oscillations usually observed in afterburners and ramjets. They observed periodic shedding of vortices from the flame holder lip with the same frequency as the thermoacoustic oscillations. They attributed the formation of these vortices to the flow divergence induced by the transverse velocity fluctuations during thermoacoustic instability. The role of high magnitude velocity fluctuations in the formation of large coherent structures during thermoacoustic instability has been reiterated by the study of Smith and Zukoski (1985) and Poinsot *et al*. (1987). These studies pointed out the importance of unsteady combustion within the large vortices in sustaining thermoacoustic instability. Smith and Zukoski (1985), through their study in a dump combustor, observed that the heat release rate fluctuations and the acoustic pressure fluctuations at the dump plane are in phase during the initiation of vortex formation, until the vortex has grown, propagated downstream and impinged against the combustor wall. Ken, Trouve and Daily (1991), through a systematic study in a model ramjet combustor, showed that the resonant time period during thermoacoustic instability is determined by the sum of vortex convection time

inside the combustor and the acoustic feedback time in the inlet. A review of thermoacoustic instability related to vortex shedding can be found in Schadow and Gutmark (1992), Coats (1996) and Renard *et al.* (2000).

1.2.4 Oscillatory Spray Dynamics

Spray dynamics plays a vital role in driving thermoacoustic instability in liquid fuelled combustors. Interaction of the fuel spray with the acoustic oscillations may result in fluctuations in atomization, vaporization and mixing which in turn lead to equivalence ratio fluctuations. Experimental studies have shown that spray-acoustic interaction alters the droplet diameter, terminal velocity, vaporization, burning rates (Sujith *et al.* 1997, 2000; Ghenai, Smith and Karagozian 2001; Chisty 2005).

Tong and Sirignano (1989) considered the effect of droplet thermal inertia on driving thermoacoustic instability using droplet vaporization models. They considered droplet vaporization as the rate determining process. Other processes such as atomization, mixing and chemical reaction were assumed very rapid. Hence the combustion response was approximated by the vaporization response. They observed that when the vaporization rate oscillations were in phase with acoustic pressure oscillations, the combustor became unstable. The effect of fuel atomization on thermoacoustic instability was investigated both theoretically and experimentally by Anderson *et al.* (1998). They observed that periodic atomization had a greater effect on driving thermoacoustic instability when compared to continuous atomization.

1.3   HOW TO CONTROL THERMOACOUSTIC INSTABILITY?

Control of thermoacoustic instability is very much essential to augment the stable operational regimes of an engine. In principle, we can mitigate thermoacoustic instability by (1) eliminating the coupling between the unsteady heat release rate fluctuations and the acoustic field in the combustor, (2) increasing the damping in the system and (3) introducing anti-sound to suppress the limit cycle oscillations and (4) secondary fuel injection. Suppression of thermoacoustic instability is classified into two categories – active control and passive control. In this section, we shall examine the principles and application of these two approaches.

1.3.1   Active Control of Thermoacoustic Instability

Active control uses external excitation, such as acoustic forcing and/or fuel modulation, to mitigate thermoacoustic instability. The main components of this strategy are the following – (1) sensor (2) controller and (3) actuator. Active control can be exercised with feedback (closed-loop control) and without feedback (open-loop control). In closed-loop control, the sensor monitors the real-time performance of the combustor. Based on this, the controller provides the necessary control action which is exercised through the actuator. In open loop control, the controller output is pre-defined and the actuator is applied without any feedback. A review of active control of thermoacoustic instability is presented in McManus *et al.* (1993) Candel (2002) and Dowling and Morgans (2005).

Ffowcs-Williams and his co-workers (1984) reported the first experimental application of active control. They used the concept of "anti-sound" – the elimination of large

amplitude limit cycle oscillations by means of destructive acoustic interference. The basic principle involves the characterization of the limit cycle oscillations and then use that information to produce a secondary source of sound. This secondary source of sound would be in anti-phase with the limit cycle oscillations. They exercised the use of the anti-sound concept in Rijke burners (Heckl 1988). Using the concept of anti-sound, Paschereit *et al*. (1998, 1999 and 2000) investigated closed-loop active control in a gaseous-fuelled swirl stabilized combustor.

In real engines, where the energy density is very high, implementing this technique of anti-sound would be impractical due to the relatively large amount of power required to drive the control actuators. Hence, control strategies based on the manipulation of energy sources seems more effective. Langhorne, Dowling and Hooper (1990) reduced the pressure oscillations in a model laboratory combustor by injecting secondary fuel. Just 3% fuel addition was found to be sufficient to control thermoacoustic instability. Open-loop control of thermoacoustic instability using relatively low-frequency modulation of the fuel flow was demonstrated by Richards *et al.* (1999) and Lubarsky and his co-workers (2003, 2004) in laboratory scale swirl stabilized combustors.

Conrad *et al.* (2003) developed a "smart" liquid fuel injector that can modify the fuel burning time by changing the spray characteristics so that the acoustic and reaction time scales does not match. In contrast to most of the active control techniques, this approach requires only a one-time modulation of the combustion process to attain the suppression of thermoacoustic instability.

1.3.2 Passive Control of Thermoacoustic Instability

Passive control involves either increasing the dissipation of acoustic energy using acoustic liners, baffles or Helmholtz or quarter wave resonators (Culick and Kuentzmann, 2006) or reducing the efficiency of acoustic driving by changing the injector geometry and the flame dynamics. Compared to active control of thermoacoustic instability, passive control measures are simple and hence find application in real combustors. Unlike active control measures, they are effective only in a narrow range of frequencies (Huang and Yang 2009).

Acoustic dampers such as Helmholtz resonators and quarter wave tubes suppress limit cycle oscillations by absorbing the incident wave intensity. We can maximize the dissipation of acoustic energy by tuning the resonator (changing the geometrical parameters) in such a way that its natural frequency matches the frequency that has to be damped. These have been used in annular and can-annular gas turbine engines (Krebs *et al* 2005, Lepers *et al.* 2005).

Steele *et al*. (2000) mitigated thermoacoustic instability in a gas turbine engine by changing the axial location of the fuel injector. A change in the axial location of the injector affects the travel time of the fuel to the flame front leading to a mismatch in the time scale of heat release rate oscillation with respect to the pressure perturbations. Gutmark *et al.* (1989) showed that a triangular cross section for the inlet, instead of a circular cross-section, suppressed thermoacoustic instability in a dump combustor. Combustion along the corner of the triangular inlet happened in a smooth and random manner due to the increased small-scale turbulence. In contrast, combustion along the flat side of the triangular inlet happened in a periodic coherent manner due to the

shedding of periodic coherent structures along the flat side. Schadow *et al.* (1990) incorporated a multi-step dump having several backward facing steps to enhance small-scale turbulence and prevent large-scale coherent structures to mitigate thermoacoustic instability in a single step dump combustor. Paschereit and Gutmark (2006) employed miniature vortex generators in the inlet of the swirlers and at the exit of the burner circumference to interfere with the rollup of vortices by inducing streamwise vorticity to suppress high-frequency thermoacoustic instability. High-frequency thermoacoustic instability in afterburners can be suppressed to an extent by using perforated flame holders and by placing perforated shrouds above the flame holders to prevent the shedding of large-scale coherent structures that are characteristics of screeching combustion (Koffel, Smolak and Trout 1956).

Paschereit *et al.* (2006) suppressed thermoacoustic instability in a swirl-stabilized combustor by stabilizing the vortex breakdown in the wake of an extended pilot lance. Williams *et al.* (2016) achieved passive control of thermoacoustic instability at elevated pressures by placing a porous inert material at the dump plane of a swirl-stabilized lean premixed combustor. Noiray *et al.* (2007) suppressed thermoacoustic instability in a laminar multiple flame burner by increasing the thickness of the perforated plate on which multiple flames were stabilized. Here, the acoustic damping of the inlet duct increased with the thickness of the perforated plate. Noiray *et al.* (2009) demonstrated a novel strategy of controlling thermoacoustic instability, in the same multiple flame burner as discussed previously, by using dynamic phase converters. Diaphragms are arranged in a staggered manner in the feeder line of adjacent burners to induce out-of-phase flame oscillations to prevent the coupling of the global heat release rate with the pressure perturbations. Surendran *et al.* (2017), in a numerical study, modelled the heat exchanger, an integral part of domestic boilers, both as an acoustic scatterer as well as

16

a heat sink and observed that increasing the inlet flow rate would increase the stable regime of operation of the boiler.

Atlay *et al.* (2010) used steady microjet air injection near the flame anchoring zone in a dump combustor to mitigate thermoacoustic instability. The authors employed both normal as well as axial air injection modes to suppress low and high-frequency thermoacoustic instability respectively. Iyengar *et al.* (2012) employed a novel concept of flash atomization to reduce the high amplitude of pressure oscillations in water injected gas turbine engines. Recently, Samarasinghe *et al.* (2017) used fuel staging to suppress thermoacoustic instability of swirl stabilized flames in a multi-nozzle can combustor. Recently, Deshmukh and Sharma (2018) employed a simple way to suppress thermoacoustic oscillations in a horizontal Rijke tube with a co-axial premixed gas burner. They radially injected steady air (1-3% of the total mass flow) from a ring around the burner into the flame and where able to obtain 30dB reduction in the limit cycle oscillations.

Engineers do not want a thermoacoustic system to operate in the unstable regime. Hence, the stability analysis of a thermoacoustic system is of paramount importance to predict the stable regimes of operation and to understand the basic mechanisms that lead to thermoacoustic instability. In the next section, we shall deal with this aspect of thermoacoustic instability.

1.4. THEORETICAL ANALYSIS OF THERMOACOUSTIC INSTABILITY: A BRIEF OVERVIEW

Traditionally, researchers used linear stability analysis to predict the unstable frequency as well as the growth rate of thermoacoustic oscillations. However, linear stability analysis does not take into account the non-linearity associated with the flame-acoustic interaction and hence cannot predict the asymptotic non-linear states such as limit cycle, quasiperiodicity and chaos as well as the amplitude of the limit cycle oscillations. This discrepancy paved the way for non-linear stability analysis of thermoacoustic systems. In this section, we shall briefly examine the various linear and non-linear approaches used in the stability analysis of thermoacoustic systems.

1.4.1 Linear Stability Analysis of Thermoacoustic Systems

In linear stability analysis, we examine the evolution of infinitesimally small perturbations given to a system to examine whether the system is linearly stable or not. If a perturbation grows exponentially, we say that the system is linearly unstable. If all the given perturbations decay exponentially, we say the system is linearly stable.

For a system without any source of energy, such as a flame, the acoustic field is represented by the classical wave equation (Dowling and Williams 1983; Rienstra and Hirschberg, 2003). The solutions to the wave equation are obtained by representing the acoustic oscillations as harmonic waves, i.e. $p' = R(\hat{p}e^{i\omega t})$ and $u' = R(\hat{u}e^{i\omega t})$. Here, R represents the real part of a complex number. Substituting these expressions for, say acoustic pressure, in the wave equation, we obtain the Helmholtz equation. Solving the

Helmholtz equation, with appropriate boundary conditions, we obtain the acoustic mode shape and the corresponding eigenfrequency.

However, for a thermoacoustic system, the wave equation is inhomogeneous due to the presence of the flame. The presence of the flame brings in a discontinuity in the analysis. This difficulty is overcome by assuming that the heat release happens in a compact zone (Dowling 1995). This assumption is valid for Rijke-type burners. The jump conditions in the acoustic variables across the flame are then obtained by integrating the linearized governing equations across the compact zone (flame location). We then observe that the acoustic pressure is continuous across the compact heat release zone. However, the acoustic velocity jumps across the compact heat release zone. The effect of a distributed heat release zone and various flow parameters such as the mean flow and the drag on the frequency of thermoacoustic oscillations in a simple geometry is systematically analysed by Dowling (1995).

The eigenfrequencies, thus obtained are in general complex numbers. The real part of the eigenfrequency determines the frequency of oscillations and the imaginary part determines the growth or decay rate. For a system with no sources and/or sinks of energy, the imaginary part of the eigenfrequency is zero. However, due to the presence of a flame, which acts as a source of acoustic energy, the imaginary part of some of the eigenfrequencies may be negative depending upon the system configuration. A negative value of the imaginary part of the eigenfrequency indicates exponential growth of the acoustic oscillations.

The form of coupling between the heat input and the unsteady flow has a vital effect on the frequency of oscillations. Crocco and Cheng (1956) provided a linearized model for

19

the interaction of the unsteady heat release rate and the acoustic field, known as the $n -$ τ model or the sensitive time lag hypothesis. It is given by,

$$\dot{q}' \propto n[u'(x_f, t - \tau)] \tag{1.1}$$

According to this model, the unsteady heat release rate fluctuation is proportional to the acoustic velocity fluctuation at the flame location (x_f) delayed by a time lag τ. Here, n is a non-dimensional scaling factor known as the interaction index. The lag includes the convection time needed by the fuel to travel the distance from the fuel injection location to the flame front, the time required for the fuel-air mixture to mix with hot products and the ignition delay. The model has been used extensively to study combustion instabilities in liquid propellant rocket motors (Culick 1988).

1.4.1.1 Flame Transfer Function Approach

One of the traditional approaches to study flame dynamics is the use of flame transfer functions. In this approach, the heat release rate response of the flame is related to the incoming acoustic perturbations as a function of the excitation frequency f, for a fixed amplitude of input perturbation. It is defined as the ratio of the relative variations of the global heat release rate to the relative perturbation velocity at the base of the flame:

$$FTF(f) = \frac{\dot{q}'/\bar{q}}{u'/\bar{u}} \tag{1.2}$$

The flame transfer function can be represented in terms of the gain $G = |FTF|$ and phase $\emptyset = \arg(FTF)$ as,

$$FTF(f) = G(f)e^{i\emptyset(f)} \tag{1.3}$$

Bloxsidge, Dowling and Langhorne (1988) investigated experimentally the response of a premixed turbulent flame, stabilized in the wake of a bluff body, to weak harmonic sound waves. They developed an empirical model, which described the linear fluctuations in heat release rate as a function of the flow velocity and performed a linear stability analysis for a ducted flame. The predicted frequencies and mode shapes were in good agreement with Langhorne's (1988) low Mach number experiments. The linear theory was also successful to a good extent for higher Mach number flows (Macqisten and Dowling 1993) and complex geometries (Macquisten and Dowling 1995).

Fleifil *et al.* (1996) developed a kinematic model to describe the dynamic response of a laminar premixed flame stabilized on the rim of a pipe to both uniform and non-uniform velocity fluctuations. They showed that the magnitude of the heat release rate oscillations and its phase with respect to the velocity perturbations depend primarily on the flame Strouhal number, which is the ratio of the dominant frequency times the tube radius to the laminar burning velocity. Using this non-dimensional number, they observed that high-frequency perturbation passes through the flame while low frequencies lead to a strong response, indicating a low pass filter flame response. These observations were in good agreement with the experiments of Perry and Blackshear (1993).

Ducruix, Durox and Candel (2000) extended the model of Fleifil *et al.* (1996) to include the effect of the flame cone angle and experimentally verified their observations. Schuller, Durox and Candel (2003) analytically derived a unified model for the transfer functions of laminar conical and V-flames. Their model, based on the linearized *G* equation for an inclined flame, includes the effect of convective perturbations propagating upstream of the flame. They showed that the angle between the flame and

the mean flow direction is critical in determining the dynamics of inclined flames. The conical flame behaves as a low pass filter; insensitive to the low amplitude incident velocity perturbations. In contrast, the V-flame behaves as an amplifier in a preferred range of frequencies and hence is more susceptible to thermoacoustic instability.

A thermoacoustic system can be represented as a network of acoustic elements. Each element of the system namely, the air/fuel supply, flame, combustion chamber, exit nozzle etc. is described by a linear relation associating the acoustic quantities on both sides of the system. The transfer functions of each of these elements can be combined to form a system of linear equations. The eigenvalues of the system thus obtained determines the stability of the system and the corresponding eigenfunctions describe the acoustic mode shapes. Extensive studies in the area of network modeling have been done by Paschereit and co-workers (Paschereit and Polifke 1998; Paschereit *et al.* 1999; Schuermans *et al.* 2000).

Flame transfer function approach has been applied to simple experiments (Paschereit *et al.* 1999, Sattelmayer 2003, Noiray *et al.* 2006, 2007) and practical configurations taking into account their geometrical and flow complexities (Krebs *et al.* 2005, Raux *et al.* 2005).

1.4.2 Non-Linear Stability Analysis of Thermoacoustic Systems

Linear stability analysis predicts the growth rate of infinitesimally small perturbations, which grow exponentially if the system is linearly unstable. However, in reality, when a combustor becomes unstable, the amplitude of oscillation saturates at a limit cycle.

Many studies have been put forward to account for this non-linear behaviour of thermoacoustic oscillations.

In solid propellant rocket engines, Culick and co-workers used non-linear acoustics to describe the unsteady gas dynamics and provided a theoretical explanation for the phenomenon of saturation of amplitude during limit cycle oscillations (Yang, Kim and Culick 1990, Culick 1994, Jahnke and Culick 1994, Burnley and Culick 1999). They, however, could not provide an explanation for the 'triggering' of instability.

In gas turbine combustors, studies by Peracchio and Proscia (1998) and Lieuwen (2002) emphasized the importance of non-linearities associated with the flame dynamics rather than that associated with non-linear gas dynamics as the determining factor in the analysis of limit cycle oscillations. Many experimental studies also reported the saturation of heat release rate oscillations during thermoacoustic instability (Lieuwen and Neumeier 2002; Lee and Santavicca 2003; Balachandran *et al.* 2005; Bellows *et al.* 2007; Birbaud *et al.* 2007). Recently, Sirignano (2015) presented a review on the driving mechanisms for thermoacoustic instability with focus on nonlinear gas dynamics.

1.4.2.1 Nonlinear Describing Function Approach

Studies have utilized the describing function approach from nonlinear control theory to account for the saturation of amplitude during the limit cycle oscillations (Kochenburger 1950). This approach, known as the flame describing function (FDF) in combustion parlance, is a modified version of the flame transfer function. The main idea is to define a transfer function which depends both on the frequency and the

amplitude of input forcing. Henceforth, we obtain growth rates and eigenfrequencies which depend on the frequency (f) as well as the amplitude of perturbation $|u'|$ impinging on the flame. It is defined as:

$$FDF(f, |u'|) = \frac{\dot{q}'/\bar{q}}{u'/\bar{u}} = G(f, |u'|)e^{i\emptyset(f,|u'|)} \tag{1.4}$$

Dowling (1997) used the describing function analysis to estimate the limit cycle amplitudes. She extended the model of Bloxsidge *et al.* (1988) to include non-linearities. The main non-linearity considered was that of the 'saturating' nature of the heat release rate. Their prediction of the limit cycle amplitude was in good agreement with the experimental work of Langhorne (1988).

Noiray *et al.* (2008), developed a flame describing function approach to investigate the non-linear stability of burners. Their theoretical results were in good agreement with their experiments. They were also able to demonstrate the phenomenon of mode switching (jump in the dominant frequencies) and triggering apart from predicting the amplitude and frequency of limit cycle oscillations.

1.4.2.2 Triggering and Non-Normality

Stability of a system may change when a control parameter is varied. When a small smooth change in the control parameter results in a sudden qualitative change in system behaviour, we say that the system has undergone a bifurcation (Strogatz 1994). A thermoacoustic system loses its stability and becomes unstable (reaches limit cycle oscillations) through Hopf bifurcation, which is of two types, namely supercritical and subcritical Hopf bifurcation (figure 1.2). In supercritical Hopf bifurcation, as soon as the control parameter crosses the critical value, small amplitude limit cycle oscillations

24

are observed. The amplitude of the limit cycle oscillations gradually increases and then saturates with a further increase in the control parameter. In subcritical Hopf bifurcation, the thermoacoustic system suddenly becomes unstable as the control parameter crosses its critical value. Hence, the subcritical transition to instability is always much more dramatic and potentially very dangerous in thermoacoustic systems.
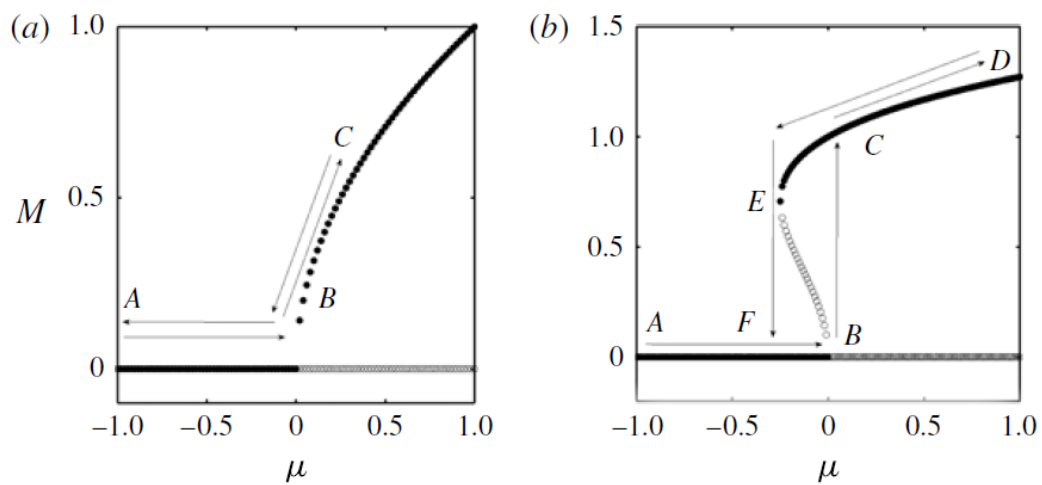
Figure 1.2: The variation of the measure M with respect to a control parameter μ for (a) supercritical and (b) subcritical Hopf bifurcation. In super critical bifurcation, as the control parameter crosses the Hopf point (B), low amplitude stable limit cycle oscillations are observed. However, for a subcritical bifurcation, large amplitude limit cycle oscillations are seen as soon as the system becomes unstable. The region $BCEF$ in (b) shows the bistable zone. Reproduced with permission from Gpalakrishnan and Sujith (2015).

Sub-critical transition to thermoacoustic instability has been extensively studied in Rijke tubes (Matveev 2003, Mariappan *et al* 2010, Subramanian, Sujith and Wahi 2013). The bifurcation plot of a sub-critical transition to instability can be divided into three regions: (a) a globally stable regime where perturbations of any magnitude decay in time, (b) a bi-stable zone where the system can reach either a steady state or limit cycle oscillations depending upon the magnitude of the initial perturbation and (c) a

globally unstable region where an infinitesimally small amplitude perturbation causes the system to reach limit cycle oscillations. A bi-stable zone is a characteristic feature of the subcritical transition to instability.

In the bi-stable zone, a system transitions to the stable limit cycle oscillations if the amplitude of the initial perturbation is above a threshold. This phenomenon is referred to as triggering. Triggering instability has been observed in solid rocket motors (Dickinson 1962; Mitchell, Crocco and Sirignano 1969) and liquid rocket motors (Culick 2006, Urbano *et al.* 2016).

Wicker *et al.* (1996) described the threshold required for triggering as the unstable limit cycle. They observed that the phase and the frequency of the initial pulse are the two important factors determining the phenomenon of triggering. They also remarked that for triggering to occur most of the pulse energy should be contained in the fundamental acoustic mode. One cause for triggering is the background noise inherent in the system. Noise-induced transition to thermoacoustic instability has been studied numerically by Waugh, Geuss and Juniper (2011), Waugh and Juniper (2011) and experimentally by Jagadeesan and Sujith (2012) in a Rijke tube. Gopalakrishnan and Sujith (2015) experimentally studied the effect of noise on the hysteresis width in a Rijke tube.

Thermoacoustic systems are non-normal in nature (Sujith, Juniper and Schmid 2016). Non-normal systems are characterized by non-orthogonal eigenvectors. Hence, such systems can exhibit transient growth of oscillations even when the eigenvalues indicate linear stability. In the subcritical zone, triggering can occur if the transient growth of oscillations crosses the threshold amplitude. Hence, a non-modal analysis of a thermoacoustic system is indispensable.

26

Nicoud *et al.* (2007) showed that in the presence of unsteady heat release or complex impedance boundary conditions, the eigenvectors of a thermoacoustic system are non-normal. Balasubramanian and Sujith (2008*a*) brought to light the non-normal behaviour of a confined diffusion flame model. The unsteady diffusion flame in a Burke-Schumann type geometry was studied by the infinite rate chemistry model. The flame response to acoustic velocity perturbations was found to be non-linear and non-normal. They used the Galerkin technique to simulate the one-dimensional acoustic model. They observed that the coupled combustion-acoustic system is non-linear and non-normal. Non-normality has been reported in Rijke tube (Balasubramanian and Sujith 2008*b*, Juniper 2011) and premixed flame burners (Subramanian and Sujith 2011). The fact that traditional controllers based on classical linear stability analysis fail due to the transient growth of oscillations highlights the importance of non-normality in thermoacoustic systems (Kulkarni, Balasubramanian and Sujith 2011).

In the next sections, we examine the new approaches used by researchers for the analysis of thermoacoustic systems, namely dynamical systems theory and complex systems theory. We first focus on the results from the application of tools from dynamical systems theory.

1.5   DYNAMICAL SYSTEMS APPROACH

A system whose dynamics changes with time is called a dynamical system. Such systems are described by a set of difference equations (for discrete systems) or differential equations (for continuous systems). Dynamical systems theory deals with the long-term qualitative behaviour of a system. In this section, we shall see a brief

overview of the application of dynamical systems theory to characterize the different non-linear behaviour of thermoacoustic systems.

Jahnke and Culick (1994), using numerical continuation methods observed that limit cycle oscillations are not the only asymptotic state of a thermoacoustic system. They, for the first time, reported that the system could undergo pitchfork and torus bifurcation and exhibit quasiperiodic oscillations. Quasiperiodicity is characterized by the presence of two incommensurate dominant frequencies. Quasi-periodic oscillations were later observed in experiments on a premixed laboratory combustor (Sterling 1993). Period doubling route to chaos has been reported in numerical studies (Lie and Turan 2009; Datta *et al.* 2009).

Kabiraj and co-workers (Kabiraj and Sujith 2012; Kabiraj *et al.* 2012; Kabiraj, Sujith and Wahi 2012) performed a systematic bifurcation analysis in a laminar premixed burner. They observed that the onset of thermoacoustic instability occurs via a Hopf bifurcation. On further change in the control parameter (the flame location), they observed quasiperiodicity and intermittency prior to flame blowout. This was the first reported observation of intermittency in a thermoacoustic system. They were also the first to report the route to chaos in a thermoacoustic system. They characterized these different dynamical states using bifurcation plots, phase space reconstruction and recurrence plots obtained from the acoustic pressure and the flame dynamics using high-speed chemiluminescence imaging respectively. Later, these findings were reported in numerical studies (Kashinath, Hemchandra, and Juniper 2013; Kashinath, Waugh, and Juniper 2014; Orchini, Illingworth and Juniper 2015).

28

Since the present study deals with experiments in a turbulent combustor, we shall now focus on the temporal and spatiotemporal dynamics of turbulent thermoacoustic systems.

1.5.1 Temporal Dynamics of Turbulent Thermoacoustic Systems

In this section, we first examine the route to thermoacoustic instability in a turbulent thermoacoustic system. We then discuss the various precursors developed by researchers based on the analysis of acoustic pressure measurements. Finally, we discuss the recent findings based on the analysis of coupled interaction of acoustic pressure and global heat release rate oscillations using the framework of synchronization theory.

1.5.1.1 Transition to Thermoacoustic Instability

In order to understand the transition from combustion noise to thermoacoustic instability, researchers have used tools from dynamical systems theory. Early studies in this direction considered the onset of thermoacoustic instability as a loss of stability of a fixed point via Hopf bifurcation (Lieuwen 2002; Ananthakrishnan, Deo and Culick 2005). This description works very well for laminar systems. However, for turbulent combustors, this description is incomplete.

The time domain analysis of thermoacoustic oscillations in turbulent combustors has also been studied from a stochastic viewpoint. In this approach, the background turbulent fluctuations in the combustors are modelled using noise terms. Lieuwen and Banaszuk (2005) considered the effect of modeling the background turbulent

fluctuations both as an additive and parametric excitation sources on the combustor's stability boundaries. Clavin *et al.* (1994) modelled the effect of turbulence on heat release rate as a parametric noise that appeared in the wave equation as a multiplicative noise term. The Fokker-Planck equation for the evolution of the transition probability density function for the amplitude of pressure oscillation predicted erratic bursts, as observed in liquid rocket motors. Recently, Noiray and Schuermans (2013*a*) modelled combustion noise as additive white noise and analyzed supercritical bifurcations using stochastic differential equations. Using the same approach, Noiray and Schuermans (2013*b*) explained the switching between the standing and spinning azimuthal thermoacoustic modes in annular combustors.

Nair *et al.* (2013) remarked that the low amplitude aperiodic pressure oscillation characterizing stable combustion (also known as combustion noise in the community) in a turbulent combustor is not exactly 'noise' in the usual sense. Through a series of tests of determinism, the authors suggested that combustion noise is deterministic and displays a chaotic behaviour. Later, Tony *et al.* (2015), through a more detailed surrogate analysis, confirmed that combustion noise is indeed deterministic chaos. These studies show that the low amplitude aperiodic pressure oscillations generated in a turbulent reactive flow field characterizing stable combustion do not correspond to a stable fixed point.

Nair, Thampi and Sujith (2014) observed that in a turbulent combustor, the transition from combustion noise to thermoacoustic instability occurs via a dynamical state known as intermittency. Figure 1.3 shows the time series of acoustic pressure obtained during combustion noise, intermittency and thermoacoustic instability in a bluff body stabilized combustor used in the present study. Combustion noise is characterized by

30
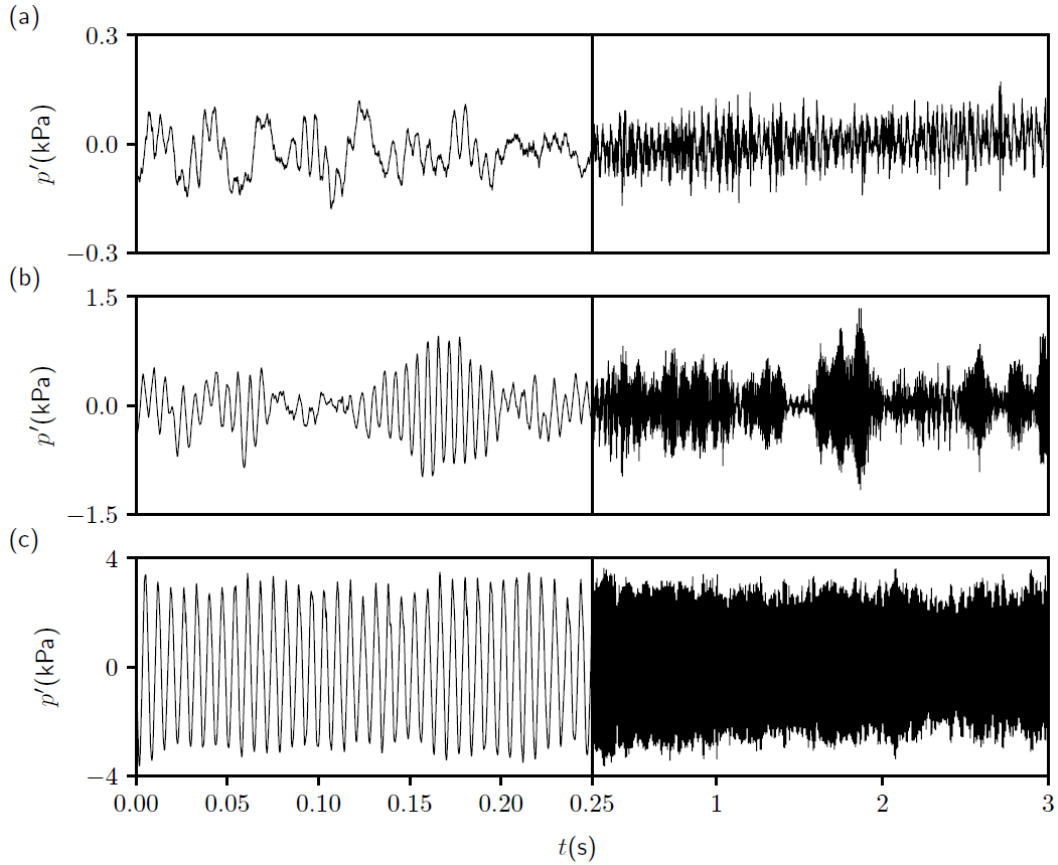
Figure 1.3 The time series of acoustic pressure obtained from the experiments performed on the setup used in the present thesis during (a) combustion noise ($\varphi = 0.97$), (b) intermittency ($\varphi = 0.81$) and (c) thermoacoustic instability ($\varphi = 0.62$). During combustion noise, the pressure fluctuations have low amplitude and are aperiodic in nature. During intermittency, we observe high amplitude bursts of seemingly periodic oscillations embedded amidst epochs of low amplitude aperiodic fluctuations. Thermoacoustic instability is characterized by high amplitude periodic oscillations with a frequency of 142 Hz. The equivalence ratio is reduced by keeping the fuel flow rate constant and increasing the air flow rate.

low amplitude aperiodic pressure fluctuations. In contrast, thermoacoustic instability is characterized by high amplitude periodic pressure oscillations. Intermittency is characterized by high amplitude bursts embedded amidst epochs of low amplitude aperiodic oscillations, in an apparently random manner. These intermittent oscillations are represented as homoclinic orbits in phase space (Nair and Sujith 2013). Many other researchers also observed the intermittency en route to thermoacoustic instability in

31

turbulent combustors (Gotoda *et al.* 2014; Domen *et al.* 2015; Sampath and Charavarthy 2016; Wilhite *et al.* 2016; Kheirkhah *et al.* 2017; Ebi *et al.* 2018). A review of the same can be found in Pawar and Sujith (2018). Intermittency is also observed en route to lean blow out in turbulent combustors (Gotoda *et al.* 2011, 2012, 2014; Unni and Sujith 2015).

Combustion noise is known to have a broad amplitude spectrum with shallow peaks near the acoustic modes of the duct (Chakravarthy *et al.* 2007). This shows the presence of multiple time scales in the temporal dynamics characterizing combustion noise. Fractal theory can be used to describe such a dynamics spread over multiple orders of temporal magnitude (Montroll and Schlesinger 1982; Schlesinger 1987).

Fractals are complex patterns that are self-similar across different scales. Self-similarity and fractal dimension are the two important properties of fractals. Self-similarity implies that if we zoom into a fractal object many times, we find the same shape at every step. Fractal dimension is a non-integer dimension which characterizes the space-filling capacity of a fractal. Fractal dimension tells us how a fractal scales differently from the space in which it is embedded. A fractal time series has a fractal dimension between one and two. A time series is multifractal if it has interwoven subsets with different fractal dimensions (Frisch and Parisi 1985). Fully developed turbulence is an example of a multifractal system (Sreenivasan 1991).

Nair and Sujith (2014) showed that the acoustic pressure fluctuations characterizing combustion noise displays scale invariance. This implies that the time series looks similar on many different scales of observation. The scaling properties of the fractal time series is determined by a constant called Hurst exponent (H). If $p(t)$ is a fractal

time signal, then $p(ct) = p(t)/c^H$, where c is a scaling constant, is another fractal time signal. Certain signals exhibit complex scaling dynamics that cannot be described by a single fractal dimension. Such scaling behaviour involves multiple generalized Hurst exponents signifying the presence of varying fractal dimensions. Such signals are called as multifractal signals. Using multifractal detrended fluctuation analysis (Kantelhardt *et al.* 2001, 2002), Nair and Sujith (2014) also showed that the aperiodic low amplitude pressure fluctuations characterising combustion noise is multifractal. On the other hand, thermoacoustic instability has an amplitude spectrum characterized by narrow peaks. This implies that the dynamics is characterized by processes involving few time scales. Thus, as the turbulent thermoacoustic system transitions from combustion noise to thermoacoustic instability, multifractality in the temporal dynamics disappears.

1.5.1.2 Precursors to an Impending Thermoacoustic Instability

The ability to forewarn an impending thermoacoustic instability is very useful for the gas turbine industry to save millions of dollars in their maintenance. Several measures have been put forward by researchers to forewarn an impending thermoacoustic instability. Lieuwen (2005) characterized the damping present in the system by calculating the autocorrelation function of the acoustic pressure. He showed that the onset of thermoacoustic instability happens when the damping coefficient is zero. Nair and co-workers (2012, 2013, 2014*a*, 2014*b*) came up with a number of precursors, namely the recurrence rate, the time spent by the system in the aperiodic regime of pressure oscillations, the Shannon entropy, the Hurst exponent and the 0-1 test for chaos, obtained by using tools from dynamical systems theory and non-linear time series analysis. A smooth variation in these parameters was observed due to the presence of intermittency between the states of combustion noise and thermoacoustic

33

instability. Unni *et al.* (2015) used measures from symbolic time series analysis to predict an impending thermoacoustic instability. Using the phenomenon of critical slowing down near a bifurcation point, Gopalakrishnan *et al.* (2016) used indicators such as variance and conditional heteroscedasticity as early warning measures. Recently, Murugesan and Sujith (2015) and Godavarthi *et al.* (2017) used measures from complex network theory to foretell an impending thermoacoustic instability. Details of these network measures will be discussed in Chapter 2.

1.5.1.3 Description of Thermoacoustic Instability Using Synchronization Theory

Until now, most of the studies in the temporal domain were concerned with either the acoustic pressure or heat release rate measurements separately. But, we know that thermoacoustic instability is a result of the coupled interaction between the acoustic field and the unsteady heat release rate fluctuations (Rayleigh criteria). Recently, using the framework of synchronization theory, Pawar *et al.* (2017) described the transition to thermoacoustic instability as mutual synchronization of two non-identical oscillators namely, the acoustic field of the combustor and the heat release rate fluctuations. During combustion noise, the acoustic pressure and the heat release rate fluctuations are desynchronized with each other. On the contrary, during thermoacoustic instability, these oscillators exhibit synchronized periodic oscillations. During intermittency, they observed intermittent phase synchronization, wherein these two oscillators are synchronized during the periodic epochs and desynchronized during the aperiodic epochs of their oscillations. They also discovered two types of limit cycle oscillations namely, a weakly correlated and the other a strongly correlated limit cycle oscillations. They used a statistical measure from recurrence theory to characterize the synchronization behaviour of the acoustic pressure and the heat release rate oscillations.

Using this measure, they demonstrated that the weakly correlated limit cycle oscillations correspond to phase synchronization and strongly correlated limit cycle oscillations correspond to generalized synchronization. Hence, using the framework of synchronization theory, they gave a new description to the onset of thermoacoustic instability i.e., the turbulent combustor dynamics transitions from a desynchronized state to a synchronized state (generalised synchronization) through intermittent phase synchronization and phase synchronization. The same route to thermoacoustic instability is observed in a swirl-stabilized combustor (Pawar *et al.* 2018). Chiocchini *et al.* (2018) developed a precursor to an impending thermoacoustic instability using synchronization theory.

1.5.2   Spatiotemporal Dynamics of Turbulent Thermoacoustic Systems

In the past, there have been studies that examined the spatiotemporal dynamics during the transition to thermoacoustic instability. Most of these studies, however, focused on the spatiotemporal dynamics only during combustion noise and thermoacoustic instability. These studies elucidated the emergence of large-scale coherent structures during thermoacoustic oscillations and the modification of the flame dynamics by these flow structures (Rogers and Marble 1956; Smith and Zukoski 1985; Poinsot *et al*. 1987; Schadow and Gutmark 1992; Coats 1996; Chakravarthy *et al.* 2007; Shanbhogue 2008; Steinberg *et al.* 2010; Schwing, Sattelmayer and Noiray 2011; Emerson *et al.* 2012).

Recently, there have been a few studies that focussed on the spatiotemporal dynamics during the transition to an impending thermoacoustic instability. Unni and Sujith (2017) investigated the flame dynamics during the intermittency route to thermoacoustic instability in a turbulent combustor with a bluff body stabilized flame. During

combustion noise, the flame is stabilized along both the outer and the inner shear layer by the recirculation zone downstream of the dump plane and the stagnation point flow upstream of the bluff body respectively. During the periodic epochs of intermittency, the flame, stabilized along both the outer and inner shear layers, oscillates in a periodic fashion. A roll-up of the flame along the outer shear layer occurs due to the periodic shedding of ring vortices from the dump plane. During the aperiodic epochs of intermittency, the flame tip oscillates in an aperiodic manner. On the contrary, during thermoacoustic instability, a stronger roll-up of the outer shear layer occurs due to the emergence of periodic large-scale coherent structures downstream of the dump plane, imparting a strong periodic behaviour to the flame front.

Researchers used the framework of synchronization theory to study the spatiotemporal dynamics of the turbulent reactive flow field in a bluff-body stabilized (Mondal *et al.* 2017) and a swirl stabilized combustor (Pawar *et al.* 2018) during the intermittency route to thermoacoustic instability. They, by calculating the instantaneous phase between the acoustic pressure and the unsteady heat release rate oscillations, examined the spatial distribution of acoustic power sources in the flow field during the three different dynamical states of combustor operation. During combustion noise, the authors observed that the acoustic power production occurs in a spatially incoherent manner. In contrast, during thermoacoustic instability, the acoustic power production occurred in a spatially coherent manner over large regions. However, during intermittency, both incoherent and coherent patches of acoustic power sources coexisted together. Kheirkhah *et al.* (2017), following a similar procedure, observed that the phase difference between the acoustic pressure and the unsteady heat release rate fluctuations changes during the growth and the decay of pressure oscillations during intermittency.

Recently, George *et al.* (2018) using the framework of pattern formation, described the onset of thermoacoustic instability as the emergence of mutually sustained patterns, namely, the standing wave pattern in the acoustic field, the large-scale flow pattern in the flow field and the localized coherent patterns of the flame. They observed that the emergence of order happens via the interaction between the subsystems through the aforementioned spatiotemporal patterns.

1.6   COMPLEX SYSTEMS APPROACH TO THERMOACOUSTIC INSTABILITY: A NOVEL APPROACH

A turbulent flow induces a large number of degrees of freedom to the thermoacoustic system. The thermoacoustic system in a turbulent combustor involves the interplay of a number of processes such as molecular mixing, turbulent transport, chemical kinetics and acoustic waves operating over a wide range of length and time scales. The complex interaction of these processes over such large number of degrees of freedom gives rise to a rich spatiotemporal dynamics, with multifractal and chaotic behaviour on one hand (during combustion noise) and ordered periodic behaviour on the other hand (during thermoacoustic instability). This prompts us to consider the thermoacoustic system in a turbulent combustor as a complex system.

Complex systems approach is a new approach in the science of studying how the interaction among the constituent parts gives rise to the collective behaviour of a system (Bar-Yam 1997). This approach is providing a new perspective on the understanding of the physical, biological, ecological and social universe. One of the efficient tools to study such complex systems is complex network (Barabasi 2011). In complex network theory, the components of a complex system are considered as nodes and the

interactions between the nodes are represented as links. The discovery of small world networks (Watts and Strogatz 1998) and scale-free networks (Barabasi and Albert 1999) paved the way for the birth of complex network theory.

Based on ideas from graph theory and statistical physics, complex network theory allows a detailed and quantitative investigation of the interplay between network topology and dynamics on the interacting elements (Albert and Barabasi 2002). Researchers are now trying to understand how an enormous network of interacting dynamical systems behaves collectively, given their individual dynamics and coupling architecture. Complex network theory has found applications in different frontiers of science and engineering such as brain research, epidemics, climatology, sociology, economics, physiology, computer science and transport engineering (Strogatz 2001; Barabasi 2003; Boccaletti *et al*. 2006; Donges *et al.* 2009; Newman 2010; Barthelemy 2011). We shall discuss more about complex networks and its application in detail in Chapter 2.

Recently, complex network theory has found applications in the analysis of thermoacoustic systems. Murugesan and Sujith (2015), using the visibility algorithm (Lacasa 2008) to construct networks from the time trace of pressure, brought to light the scale-free nature of combustion noise. They observed that as a turbulent combustor transits from combustion noise to thermoacoustic instability, the topology of the network changes from scale-free to regular, reflecting the emergence of order from disorder. Okuno, Small and Gotoda (2015) used cycle networks and phase space networks to show the high dimensional nature of thermoacoustic instability. Godavarthi *et al.* (2017) used recurrence networks to study the topology of the phase space corresponding to the different dynamical states of combustor operation. Gotoda *et al.*

(2017) showed the presence of a small-world nature in the recurrence network constructed from the combustion state close to lean blow-out.

Most of the above mentioned analysis were performed by constructing networks from a time series. Spatial networks (Barthelemy 2011), where the spatial information of the structure of the network is taken into account, gives a better understanding of the system under study. Time-varying spatial networks further provides a deeper insight into the evolution of complex systems. In the present work, we use complex networks to investigate the spatiotemporal dynamics of a turbulent thermoacoustic system.

1.7   INTERIM SUMMARY AND MOTIVATION

Thermoacoustic instability refers to the phenomenon of generation of self-excited high amplitude periodic acoustic pressure oscillations due to the positive feedback between the acoustic pressure and the unsteady heat release rate fluctuations in the combustion chamber. Thermoacoustic instability is a plaguing problem in the aerospace and power generation industry as it leads to a reduced life of system components due to increased mechanical and thermal stresses and in some cases, cause mission failures and engine failures leading to a loss of revenue to the tune of millions of dollars. Understanding the mechanism and the control of thermoacoustic instability has been a topic of intense research for decades.

The use of dynamical systems theory and tools from nonlinear time series analysis has helped us to characterize the transition to an impending thermoacoustic instability and other nonlinear asymptotic states. The route to chaos, the multifractal signature of combustion noise and the intermittency route to thermoacoustic instability in a turbulent

thermoacoustic system are the major discoveries using the dynamical systems approach. One major application of these findings is the successful development of precursors to an impending thermoacoustic instability (Nair *et al*. 2012). Recently, the analysis of the coupled temporal behaviour of the acoustic pressure and the global heat release rate oscillations using synchronization theory reported the onset of thermoacoustic instability as a mutual synchronization between the acoustic field in the combustion chamber and the turbulent reactive flow (Pawar *et al.* 2017).

Most of these studies, however, focus on the temporal dynamics of a thermoacoustic system. The phenomenon of thermoacoustic instability involves a complex interplay amongst the acoustic field, the hydrodynamics and the flame dynamics leading to rich spatiotemporal dynamics. Traditionally, most of the spatiotemporal analysis of a thermoacoustic system focussed on the flame and the flow diagnostics only during combustion noise and thermoacoustic instability. These studies reported the periodic emergence of coherent structures during thermoacoustic oscillations. However, the vortical interaction leading to the emergence of coherent structures during the intermittency route to thermoacoustic instability needs to be analysed. Also, the critical regions in the flow field that control the spatiotemporal dynamics of a thermoacoustic system are yet to be identified and investigated.

The spatiotemporal analysis of intermittency route to thermoacoustic instability has not received much attention until recently. Mondal *et al.* (2017) observed that the spatiotemporal dynamics during intermittency resembles a chimera-like state because of the simultaneous presence of patches of synchronous periodic oscillations and asynchronous aperiodic oscillations in the turbulent reactive flow field. They observed that during combustion noise the acoustic power production happens in small

fragmented clusters and during thermoacoustic instability it happens in large clusters of spatially coherent regions. How this emergence of large clusters of spatially coherent regions of acoustic power production occurs at the onset of thermoacoustic instability is still unresolved.

Complex network has emerged as a popular tool for the spatiotemporal analysis of complex systems such as the human brain and the climate. In the present study, we use complex network theory to investigate the spatiotemporal dynamics during the intermittency route to thermoacoustic instability in a turbulent combustor.

1.8   OBJECTIVES AND OVERVIEW OF THE THESIS

The objectives of the present work are enlisted below:

1. To analyse the spatiotemporal evolution of acoustic power sources during the intermittency route to thermoacoustic instability and examine how the emergence of large clusters of spatially coherent regions of acoustic power sources happens at the onset of thermoacoustic instability.

2. To characterize the vortical interaction during the different dynamical states of combustor operation.

3. To identify the critical regions in the turbulent reactive flow field that controls the dynamics of a thermoacoustic system during combustion noise, intermittency and thermoacoustic instability.

4. To mitigate thermoacoustic instability by injecting micro-jets at the critical regions identified in step 3 during thermoacoustic instability.

The outline of the rest of the thesis is briefly described as follows. We introduce the basic concepts and application of complex network theory in **Chapter 2**. In this chapter, we shall see how to construct a network from a time series. We shall also examine spatial networks and time-varying spatial networks. In **Chapter 3**, we discuss the

details of the experimental setup, which is a bluff body stabilized turbulent combustor with a backward facing step at the inlet of the combustion chamber. All the findings of this thesis are based on the different experimental studies performed on this setup. The various techniques used to acquire the spatiotemporal data is also detailed in this chapter.

In **Chapter 4**, we discuss the spatiotemporal dynamics of the turbulent flow field during combustion noise, intermittency and thermoacoustic instability. In **Chapter 5**, we examine the spatiotemporal evolution of acoustic power sources as the thermoacoustic system transitions from combustion noise to thermoacoustic instability via intermittency. This study examines the spatial emergence of large regions of coherent acoustic power sources at the onset of thermoacoustic instability from a state of incoherent acoustic power production during combustion noise. To that end, we construct time-varying weighted local acoustic power and vorticity networks. In **Chapter 6**, we characterize vorticity interaction during the intermittency route to thermoacoustic instability. We construct time-varying weighted vorticity networks based on Biot-Savart law.

In **Chapter 7**, we perform a spatial network analysis using the correlation between the time series of velocity obtained from the analysis of particle image velocimetry. The study helps in identifying the critical regions in the flow field during different dynamical states of combustor operation. In **Chapter 8**, we introduce a "smart" way to mitigate thermoacoustic instability. We suppress thermoacoustic oscillations by injecting micro-jets at the critical locations identified in **Chapter 7**. The conclusions of the present work and the scope for future work are outlined in **Chapter 9**.

CHAPTER 2

COMPLEX NETWORKS

Networks are ubiquitous in nature. Social networks, transportation networks, the network of neurons in our brain, the Internet, the World Wide Web, protein-protein interaction network, mobile networks and a network of research collaborators are only a few examples. All these systems involve the interaction of a large number of components. A system where a large number of interacting elements gives rise to a collective behaviour, such as the emergence of an unexpected pattern in a flock of birds or a school of fish, is called a complex system (Bar-Yam 1997). In recent years, complex networks have emerged as the most promising tool to study complex systems. The importance of complex networks is very well reflected in the words of Albert Barabasi, a pioneer in the field (in his commentary in *Nature Physics*, 2011): *"Therefore, if we are ever to have a theory of complexity, it will sit on the shoulders of network theory."* In this chapter, we shall briefly explore the world of complex networks.

2.1 BASIC CONCEPTS

Network theory is built upon ideas from graph theory and statistical physics. In network theory, the components of a system are represented as nodes and their interactions are represented as links between the nodes. Mathematically, the interactions among the

nodes of a network are represented by a square matrix, known as the adjacency matrix

A. Suppose there are n nodes and e edges in a network, then the elements of A are given

by:

$$A_{ij} = \begin{cases} 1 & if\ i \neq j \\ 0 & if\ i = j \end{cases} \qquad (2.1)$$

where $i, j = \{1, 2, 3,..., n\}$ are the nodes of the network. Here, 1 denotes the existence

of a link between the nodes and 0 the absence. The adjacency matrix is a symmetric

matrix for undirected networks. A network is called a directed network if directionality

is associated with the edges. Say, e_{ij} represents a link from i to j. Then for a directed

network, $e_{ij} \neq e_{ji}$. In the standard definition of a network or a graph, self-loops or

multiple edges between nodes are not considered. Graphs with self-loops or multiple

edges between the nodes are called multigraphs (Wasserman and Faust 1994, Bollobas

1998). The present study, however, does not involve such graphs.
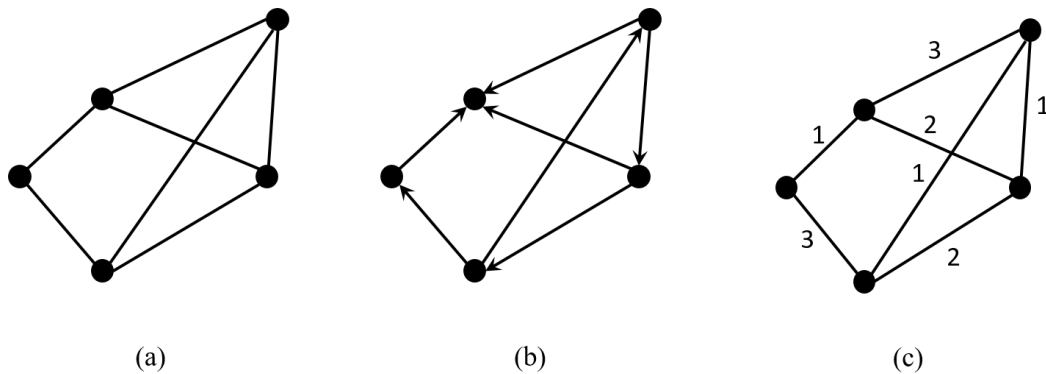
Figure 2.1: Graphical representation of (a) an undirected network, (b) a directed network and (c) a weighted network.

A weighted network is a network which takes into account the strength of the interaction

between the nodes. For example, in an airline network, the weight (w_{ij}) of a link could

be the average number of passengers transported between two airports (nodes of the

network) per year. For a weighted network, all the ones in the adjacency matrix is replaced with the corresponding weights.

Graphically, a node is represented as a dot and a line joining two dots represents the link. Figure 2.1 shows the pictorial representation of (a) an undirected network, (b) a directed network and (c) a weighted network having $n = 5$ nodes and $e = 7$ edges.

2.1.1   Network Measures

Network measures are used to characterize and quantify the topological features of a network. They are derived directly or indirectly from the adjacency matrix. We shall first look at some network measures that highlight the importance of a single node in the network. These are called network centrality measures. Here, we shall discuss the three most popular ones, which are used in the present study, namely, degree, betweenness centrality and closeness centrality. Details of other centrality measures such as page rank centrality, eigenvector centrality, katz centrality are presented in Newman (2010).

The degree, k_i, of a node i is the number of connections or neighbours of the node. Using the elements of the adjacency matrix, degree of a node is defined as:

$$k_i = \sum_{j=1}^{n} A_{ij} \tag{2.2}$$

A value of 0 implies that the node is an isolated node. The maximum value of the degree for a node is $n - 1$. If every node is connected to all other nodes of the network, then each node will have a degree $k = n - 1$. Such a graph is called a complete graph. A node having a higher degree than others is expected to have a stronger influence on the

functioning of the network. For example, in social networks such as Instagram, an account with maximum followers signifies the popularity of that individual – the person may be a film star, sports icon or political leader.

The degree distribution, $P(k)$, of a network characterises the underlying topology of the network. It gives the fraction of nodes with degree k or the probability that a randomly chosen node has a degree k. A random network, where the nodes are arbitrarily connected to each other, has a Poisson degree distribution ($P(k) = e^{-\langle k \rangle} \frac{\langle k \rangle}{k!}$, where $\langle k \rangle$ is the average degree). On the contrary, the degree distribution of a regular network, such as a rectangular lattice, has just a point in the degree distribution as the number of neighbours of all the nodes are identical, except for the nodes at the boundary of the lattice.

Like degree, another measure that highlights the importance of a node is betweenness centrality (b_i). It is defined as the sum of the ratios of the number of shortest paths between any two nodes passing through a particular node to the total number of shortest paths between those two nodes:

$$b_i = \sum_{j,k \in n, j \neq k} \frac{d_{jk}(i)}{d_{jk}} \tag{2.3}$$

where, d_{jk} is the number of shortest paths between j and k ; $d_{jk}(i)$ is the number of shortest paths between j and k passing through the node i. To understand the concept of betweenness centrality, let us consider a football (soccer) team. A football team has three primary positions namely, defenders, midfielders and forwards. The job of the midfielders is to move the ball from the defenders to the forwards. Thus, we can hypothesise that midfielders will have high betweenness centrality. Physically, b_i of a node indicates the extent of information passing through the node i, if we assume that

46

the information travels through the shortest paths in the network. In a study on the Indian summer monsoon, Malik *et al.* (2012) used complex networks to characterise extreme rainfall events. Using betweenness centrality, they identified the moisture transport pathways assuming that moisture transport happens through the shortest path lengths of the network.

Another node centrality measure is closeness centrality (c_i) which measures the inverse of the mean shortest path length from a node to all other nodes. If the shortest path between a node i to all other nodes j connected to it is $d(i,j)$, then closeness centrality is given by

$$c_i = \sum_{j \in n, j \neq i} 2^{-d(i,j)}$$
(2.4)

Closeness centrality is used to identify the nodes which could reach all other nodes quickly. Closeness centrality can be considered as the inverse of farness, which in turn is the sum of distances to all other nodes. Physically, c_i gives the measure of the speed of information propagation in the network. For example, if any disturbance is given to a node with the highest c_i, the disturbance will travel to other nodes in a minimum amount of time. Tang (2012) used the idea of closeness centrality to contain the spread of mobile malware.

All the above measures characterises a single node of a network and assign a real number to the node. We shall now see a measure that looks at the neighbourhood of the immediate neighbours of a node. It is called the local clustering coefficient (C_i). It characterises the interconnectivity of the neighbours of a node and is defined as follows:

$$C_i = \frac{2e_i}{k_i(k_i - 1)}$$
(2.5)

47

where, e_i is the number of links between the neighbours of the node i and $k_i(k_i - 1)/2$ is the maximum number of links possible among the neighbours. The range of C_i is $0 \leq C_i \leq 1$. A value of 0 implies that the neighbours of the node are not connected to each other. Such situations arise in graphs that are trees (which has no closed loops of any kind) or a square lattice (which has no closed triangles). On the contrary, a value of 1 implies that each neighbour is connected to every other neighbour of the node. For a complete graph, the local clustering coefficient is one for all the nodes. Mostly, local clustering coefficient is used along with the degree to get an idea of the connectivity of the immediate neighbourhood of a node. A node with high degree and high local clustering coefficient implies that the node is having a large number of neighbours and the neighbours are interconnected among themselves. For example, in social networks, individuals with common friends are likely to be friends with each other.

Finally, we shall examine some network measures which characterize an entire network. The first measure is the average of all the local clustering coefficients of a network, which is called the global clustering coefficient or simply the clustering coefficient (C). Another similar measure, but not identical, is the transitivity (T) of a network. In simple terms, it takes into account the number of triangles in the network and is quantified as (Newman 2003):

$$T = \frac{3 \times number\ of\ triangles\ in\ the\ network}{number\ of\ connected\ triples\ of\ nodes} \tag{2.6}$$

where a connected triple means a collection of three nodes which may or may not form a closed triangle. Since each complete triangle with three nodes contributes three connected triangles, a factor of three is place in the numerator. This also ensures $0 \leq T \leq 1$. Transitivity is also defined as:

$$T = \frac{6 \times number\ of\ triangles\ in\ the\ network}{number\ of\ paths\ of\ length\ two} \tag{2.7}$$

where the path is any sequence of links which connect consecutive nodes of the network. Transitivity, compared to clustering coefficient, is mostly used in sociology.

The shortest path between two nodes is very crucial when it comes to efficient and swift transfer of information or goods from one location to another. Hence, the shortest paths characterise the internal structure of a network. The shortest paths of a network are represented in the form of a square matrix in which the entry d_{ij} is the shortest path from node i to node j. The largest value of d_{ij} is known as the diameter of the network. In other words, it is the shortest distance between the two most distant nodes of a network. The network diameter indicates the size of the network. The average of the shortest paths between all pairs of nodes is called the average shortest path length or the characteristic path length (L). This measure gives the typical separation between two nodes of a network:

$$L = \frac{1}{n(n-1)} \sum_{i,j=1,i \neq j}^{n} d_{ij} \tag{2.8}$$

If there are disconnected components in the network, then L diverges. One way to circumvent the issue is to consider only the pairs of nodes that are part of the largest connected component (Watts and Strogatz 1998). An alternative option is to consider the harmonic mean of the shortest paths and to define a new measure, called the efficiency (E) of the network, as (Latora and Marchiori 2001):

$$E = \frac{1}{n(n-1)} \sum_{i,j=1,i \neq j}^{n} \frac{1}{d_{ij}} \tag{2.9}$$

The characteristic path or the efficiency indicates how the transfer of goods or information takes place in the network. Lower the value of L (higher the value of E), the faster the transfer of goods or information in the network. In short, the efficiency of a network measures how fast and efficiently can we transfer information between two nodes of the network.

Some of the aforementioned network measures are used to characterise the topology of complex networks. In the next section, we shall look at the two most famous network topologies namely, small-world and scale-free networks.

2.2   SMALL-WORLD AND SCALE-FREE NETWORKS

The discovery of small-world networks (Watts and Strogatz 1998) and scale-free networks (Albert and Barabasi 1999) opened up a floodgate of research on complex networks. These two seminal papers are recognised among the top ten most cited papers in physical science by Thompson-Reuters during the decade after their publication (Barabasi 2016). In this sub-section, we shall see what these networks are and what their significances are.

2.2.1   Small-World Networks

"Six degrees of separation" is a popular phrase used to refer to the "small-world" nature of the world we live. According to this idea, a person can reach any other person on the planet at most through six steps (Barabasi 2003). This is surprising given the fact that the world population is around six billion. Similarly, The World Wide Web, which has around a billion web pages, has 19 degrees of separation as the web pages are typically

19 clicks from one another (Albert, Jeong and Barabasi 1999). The internet, which has hundreds of thousands of routers, has a separation of around 10. In a cell, with thousands of chemicals, any pair of chemicals can be connected by three steps. What causes this "small-world" behaviour in such huge networks? Watts and Strogatz came up with an explanation in 1998.

Watts and Strogatz introduced the first small-world network model (Watts and Strogatz 1998). They initially considered a ring lattice with n nodes and k connections per node. They then rewired each link randomly with probability p. In this manner, they were able to tune the topology of the network from regular ($p = 0$) to random ($p = 1$). As $p \to 0$, L varies linearly with n, whereas, for $p \to 1$, L varies logarithmically with n. For a small increase in p, $L(p)$ drops significantly. This is due to the introduction of a few long-range links or 'short-cuts' during rewiring. The rewiring procedure has a highly nonlinear effect on L as it not only contracts the distance between the nodes it connects but also their immediate neighbourhood, neighbourhoods of neighbourhoods and so on. However, a link rewired from a clustered neighbourhood to another node has almost a linear effect on the clustering coefficient C. Hence, for a small change in p, $C(p)$ practically remains unchanged even though $L(p)$ plummets. Consequently, for a broad range of intermediate values of p, $C(p)$ is high and $L(p)$ is very low. Such networks are called small-world networks. In a small-world network, the average shortest path length, L, depends logarithmically on the network size N. This model is now popularly known as Watts-Strogatz small-world network model. Alternate approaches based on the addition of links instead of rewiring have been reported to construct small-world networks (Monasson 1999; Newman 2000; Davidsen *et al.* 2002).

In a random network, the nodes are randomly connected. Most of the nodes have the same number of connections, which is characterised by the average degree of the network. The degree distribution is Poisson in nature. Since the nodes are randomly connected, the average shortest path length and the global clustering coefficient of the network is very low. On the contrary, in a regular network, all the nodes have the same number of neighbours. For example, in a 2-D rectangular lattice, each node has four neighbours (not taking into account the nodes at the boundary). The global clustering coefficient and the average shortest path length is very high for a regular network. A small-world network is a network which has the signature of both a random network (very small characteristic path length) and a regular lattice (very high clustering coefficient).

The small-world network topology is observed in many real world networks such as brain networks, power grids, the network of film actors, food webs, metabolic reaction networks, protein-protein interaction networks and scientific co-authorship networks (Boccaletti *et al.* 2006). Due to the unique combination of high clustering and low characteristic path length, the dynamical systems with small-world architecture display efficient signal processing capabilities, efficient information transfer, fast spread of epidemics and enhanced synchronizability better than regular networks.

2.2.2 Scale-Free Networks

Most of the real world large networks around us, such as the internet, the World Wide Web, the network of people connected by e-mails, citation networks, protein-protein interaction network, metabolic networks of E.coli, network of Hollywood actors, sexual relationship among people, research collaboration networks and functional brain

networks are neither random nor regular (Barabasi and Bonabeau 2003). These networks have a highly inhomogeneous connectivity pattern. While most of the nodes have only a handful of connections, there are a few nodes (known as hubs) with extremely large connections. Due to the coexistence of nodes with widely different connections, these networks lack a characteristic 'scale' and hence are known as scale-free networks. The degree distribution of a scale-free network follows a power law behaviour, $P(k) \sim k^{-\gamma}$ and the power law exponent (γ) is mostly observed to be between 2 and 3 (Barabasi 2016).

Why are most of the networks around us scale-free? Barabasi and Albert (1999) came up with a simple model, now popularly known as the BA model, to explain this. The model was designed to demonstrate the formation of the World Wide Web. The key ingredients in the model are (a) growth and (b) preferential attachment. Here, growth signifies the expansion of the network with the addition of new nodes. This is an important factor as most of the real world networks grow. Preferential attachment signifies the tendency of a new node to link to a node that is highly connected. This was based on the observation that in the World Wide Web, the web pages (nodes) with a large number of hyperlinks (links) acquire new links at higher rates than those with lesser hyperlinks. These two mechanisms also explain the existence of hubs. As new nodes tend to connect to the more connected nodes, these 'popular' nodes acquire more links over time than the less connected nodes. This "rich get richer" phenomenon mostly favours the early nodes, which are more likely to become hubs eventually.

Hubs are vital for the functioning of scale-free networks. Random removal of a considerable number of nodes from a scale-free network does not affect the overall functionality of the network. However, if we remove a fraction of these hubs, the entire

network disintegrates. Let us consider the U.S national highway and the U.S airline network to understand the concept better (Barabasi and Bonabeau 2003). In the highway network, the cities are the nodes and the highways connecting them are the links. In the airline network, the airports are the nodes and if a direct flight exists between two airports, then they are connected. Since all the major cities of U.S also have an airport, the spatial location of the nodes of both the networks are identical. However, there is a significant difference in the topology of the networks. The highway network is a random network as most of the cities have roughly the same number of highways going through them. Thus, the highway network is characterised by a peaked degree distribution (Barabasi and Bonabeau 2003).

On the contrary, there are a few airports such as Chicago, Denver, Atlanta and New York which have direct flights to almost all other U.S airports. These airports are thus the hubs of the airline network. Now, if due to some untoward incidents some of the highways gets blocked, then the road network disintegrates into fragments. Whereas, the shutdown of even a large number of airports, which have less connectivity does not disrupt the airline connectivity among the cities. However, the closure of a few critical airports (hubs) shall adversely affect the airline connectivity. Hence, scale-free networks are resilient against random failures but are extremely vulnerable to targeted attacks. Hubs are thus nick-named as the Achilles' heel of scale-free networks.

It is the presence of hubs which is responsible for the quick spread of infectious diseases such as AIDS, the spread of fashion or fads in society and the spread of computer viruses on the Internet. This is because in a scale-free network a threshold for the propagation of contagion throughout a population is absent (Pastor-Satorras and Vespignani 2001). The presence of hubs can also be of advantage. Drug delivery

targeting the hubs of the cell metabolic network can lead to the effective cure of diseases such as cancer. Immunization of hubs will be highly efficient to contain the spread of diseases as opposed to the traditional approach of random immunization.

The ubiquity of scale-free networks does not imply that all networks are scale-free. The U.S highway network, the power grid, the neural network of *C.elegans* worm and networks encountered in material science (they are regular lattices) are some examples where the scale-free property is absent.

A brief introduction to the basics ideas of complex networks concludes here. Next, we shall see how to construct complex networks from experimental data. In the present study, we construct complex networks from spatiotemporal data. Before jumping into the construction of networks from spatiotemporal data, we shall see how to construct a network from a time series and its application in the field of fluid mechanics including thermoacoustics.

2.3   COMPLEX NETWORKS FROM A TIME SERIES

There are various ways to construct a network from a time series. In this section, we shall examine the two most popular approaches followed for the construction of a network from a time series namely, (a) the visibility algorithm and (b) the recurrence network. There are other approaches namely, transition networks, cycle networks, correlation networks and *k*-nearest neighbour networks. A comparison of these different approaches is presented in Donner *et al.* (2010).

2.3.1 Visibility Algorithm

In this approach, the individual observations of a time series, $x(t)$, are considered as the nodes of a network (Lacasa 2008 *et al*.). Any two nodes, $x(t_a)$ and $x(t_b)$ are connected if a straight line can be drawn between them without intersecting any intermediate data point $x(t_c)$,

$$\frac{x(t_a) - x(t_c)}{t_a - t_c} > \frac{x(t_a) - x(t_b)}{t_a - t_b} \qquad (2.10)$$

The network, thus derived, will be undirected since the visibility condition is symmetric. The visibility algorithm is invariant under rescaling as well as translation of both the horizontal and the vertical axes of the time series. A periodic time series gives a regular network and a random time series gives a random network. A fractal time series gives rise to a scale-free network, where the power law exponent can be related to the Hurst exponent (Lacasa *et al.* 2009). A slightly modified version of the above algorithm, called the horizontal visibility graph, has been developed by Luque *et al.* (2009), which can be used to distinguish a chaotic time series from an uncorrelated random time series (series of independent identically distributed random variables).

Liu, Zhaou and Yuan (2010) constructed complex networks from the time series of energy dissipation rates in a fully developed three-dimensional turbulent flow using the visibility algorithm. They observed a power law behaviour in the degree distribution. Charakopoulos *et al.* (2014) used the visibility algorithm to characterise the various dynamical regimes of a heated vertical jet flow. They constructed a network from the time series of temperature measured experimentally at the boundary of the jet, near the jet axis and in the intermediate region. The topology of the network looked different in these three dynamical regimes.

Murugesan and Sujith (2015) introduced complex networks into the field of thermoacoustics. They investigated the topology of the networks constructed, using the visibility algorithm, from the acoustic pressure measurements during combustion noise, intermittency and thermoacoustic instability in turbulent combustors with different flame stabilisation mechanisms. During combustion noise, the network obtained from the low amplitude aperiodic pressure fluctuations is scale-free. The power law behaviour indicates the scale-invariance of combustion noise. Scale-invariance of combustion noise generated from an open turbulent flame can be obtained from the spectral analysis (Abugov and Obrezov 1978; Rajaram and Lieuwen 2009). However, for combustion noise generated in a confinement, the property of scale-invariance cannot be unmasked due to the presence of peaks corresponding to the acoustic modes of the confinement. Hence, for the first time, Murugesan and Sujith (2015) unravelled the scale invariance of combustion noise generated from a confinement with the help of complex networks. At the onset of thermoacoustic instability, they observed a regular network. Hence, the transition from combustion noise to thermoacoustic instability is reflected in the network topology as a transition from scale-free to regular. However, they could not differentiate between intermittency and combustion noise as the network constructed from intermittency was also scale-free. This shortcoming was overcome with the use of recurrence network, which will be discussed in the next section.

Okuno, Small and Gotoda (2015) used cycle networks and phase space networks to characterize thermoacoustic oscillations. They observed high-dimensionality in the dynamics of thermoacoustic oscillations with a possible presence of power-law behaviour. They also reported small-world like nature in the cycle networks constructed from pressure fluctuations during thermoacoustic instability. However, Gotoda *et al.*

(2017) showed that the recurrence network corresponding to thermoacoustic instability does not show small world characteristics.

Murugesan and Sujith (2016) used network measures as precursors to an impending thermoacoustic instability. They used network properties such as global clustering coefficient, average shortest path length, network diameter and global efficiency to characterise the topology of complex networks obtained using the visibility algorithm as the turbulent combustor transitions from combustion noise to thermoacoustic instability via intermittency. They observed that the network properties capture the changes in the combustor dynamics well before the rise in the root mean square values of the acoustic pressure during the transition from combustion noise to thermoacoustic instability.

2.3.2 Recurrence Network

Recurrence network is based on the concept of recurrences in the phase space, which is a fundamental dynamical property of deterministic dynamical systems (Donner *et al.* 2010). We can reconstruct the phase space from a time series using the Taken's embedding theorem (Takens *et al.* 1981). The two essential parameters required for phase space reconstruction are the optimum time delay and the minimum embedding dimension (Abarbanel 1996). The optimum delay is chosen as the first minimum of the average mutual information (Fraser and Swinney 1986) and the minimum embedding dimension is calculated based on the modified method of false nearest neighbours obtained using Cao's algorithm (Cao 1997).

In a recurrence network, the state space vectors in the reconstructed phase space are considered as the nodes. Two nodes are connected if the distance between them, computed using the Euclidean norm, is below a threshold ε. The recurrence matrix (R) encapsulates the recurrences occurring in the phase space,

$$R_{ij} = \theta(\varepsilon - \|X(t_i) - X(t_j)\|) \tag{2.11}$$

where $X(t_i)$ and $X(t_j)$ are the phase space vectors, ε is the recurrence threshold, i and j refers to the time instant and θ is the Heaviside function. The adjacency matrix (A) is obtained from the recurrence matrix as follows:

$$A_{ij} = R_{ij} - \delta_{ij} \tag{2.12}$$

where δ_{ij} is the Kronecker delta.

Since recurrence network is based on the concept of recurrence in phase space, it characterises the geometry of the attractor. This property has been explored by researchers recently in the area of thermoacoustic instability. Godavarthi *et al.* (2017) used recurrence networks to study the topology of the phase space corresponding to different dynamical states of a turbulent combustor. They characterised the following dynamical states namely, combustion noise, intermittency prior to thermoacoustic instability, thermoacoustic instability, intermittency post thermoacoustic instability and low amplitude oscillations prior to lean blowout by constructing recurrence networks from the time series of acoustic pressure measurements. The topology of the recurrence networks at these states resembles the structure of the attractor characterising the particular dynamical state. They observed power law scaling in the degree distributions of combustion noise and oscillations prior to lean blowout. The network measures, such as betweenness centrality and characteristic path length, were able to detect the transitions from combustion noise to thermoacoustic instability as well from

thermoacoustic instability to lean blowout. Hence, they conjectured that these measures could be used as early warning signals. Gotoda *et al.* (2017) used recurrence network to unravel the small-world nature of oscillations prior to lean blowout.

2.4 SPATIAL NETWORKS

Most of the real world complex systems have nodes and edges embedded in space. Transportation networks, internet, social and contact networks, power grids and neural networks are all examples where spatial information is relevant and just studying the network topology without considering the spatial information of the nodes gives incomplete and sometimes misleading results. Characterising and understanding the structure and dynamics of spatial networks is thus vital in obtaining deeper insights in the study of complex systems (Barthelemy 2011).

Recent years have seen a tremendous application of complex networks to study the spatiotemporal dynamics of climate systems. Scientists used measures such as Pearson's correlation coefficient and mutual information between time series to quantify the degree of statistical interdependence of different spatial regions (Donges *et al*. 2009). Tsonis and Roebber (2004) constructed a correlation based climate network from the global temperature field. They observed that the overall dynamics of the global climate system is the result of the interaction between two interweaved subnetworks: one operating in the tropics and the other at higher altitudes with the equatorial network acting as the agent connecting the two hemispheres. Malik *et al*. (2012) used a nonlinear synchronization measure, known as event synchronization (Quiroga, Kreuz and Grassberger 2002), to construct a spatial network for the spatiotemporal analysis of extreme monsoonal rainfall over South Asia. The network properties used in this study

helped to visualize the structure of the extreme rainfall fields, identification of water vapour pathways and moisture sinks. The methodology of spatial network construction using event synchronization has also been used to predict extreme floods in the eastern Central Andes (Boers *et al*. 2014).

Molkenthin *et al.* (2014) performed a spatial network analysis of prototypical flows and an ocean flow in the tropical Pacific region. In the case of prototypical flows, the authors solved the advection-diffusion equation and used the resulting temperature field to calculate the statistical interdependence between any two nodes in the flow field. They used a continuous analytical analogue of Pearson correlation to compute the correlation matrix. In the case of the real flow, they calculated the correlation matrix from the sea surface temperature using standard correlation. The analysis unravelled the relationship between the underlying velocity field and complex network measures. High values of degree coincided with high values of the velocity field and high values of betweenness centrality marked the transition zones between regions of different magnitude or direction of the underlying velocity field. The above study, however, was restricted only to stationary flows. Tupikina *et al.* (2016) extended this analysis to a meandering flow model with a time dependent velocity field. Taira, Nair and Brunton (2016) used the concept of Biot Savart law to construct a spatial network based on vortical interactions in a two dimensional decaying isotropic turbulent field obtained from direct numerical simulation. A weighted scale-free network characterizes the resulting vortical interaction network. Scarsoglio, Iacobello and Ridolfi (2016) constructed a correlation network from kinetic energy time series on a three dimensional forced isotropic turbulent field obtained from direct numerical simulation. They identified coherent patterns in the flow field using network properties.

Singh *et al*. (2017) extended the application of spatial network analysis to turbulent reactive flows. The authors developed a visibility algorithm for spatially embedded nodes for characterizing turbulent flames. The authors observed that the hubs of the network coincided with the folds in the flame front, which was attributed to the interaction of the flame front with turbulent eddies. Also, the flame front network was resilient against a random removal of nodes but susceptible to a targeted removal of hubs, thus opening up a possibility of control of turbulent flames using network theory.

In Chapter 4, we perform spatial network analysis in a turbulent combustor with a bluff body stabilized flame, based on the correlation between the time series of local velocity obtained from particle image velocimetry. We are able to identify the critical regions in the flow field using network centrality measures, during combustion noise, intermittency and thermoacoustic instability.

2.5   TIME-VARYING SPATIAL NETWORKS

In the aforementioned spatial network analysis discussed so far, the temporal evolution of the system under study was not taken into account. However, real world complex systems inherently evolve over time. Unless and until we do not take into account the dependence of time, the analysis and hence the understanding of spatiotemporal dynamics of complex systems will remain incomplete. In network theory, time-varying network analysis accounts for this dynamical nature of connectivity (Tang *et al*. 2010; Nicosia *et al*. 2012; Holmes and Saramaki 2012).

Let us consider the example of one of the most complicated complex systems - the human brain. The brain has two modes of connectivity namely, structural and functional

(Sporns 2011). Structural connectivity refers to the anatomical white matter fibres connecting different brain regions. For a healthy adult, this remains relatively constant over short time scales (seconds to minutes). Variations occur with the brain's natural development and aging or due to some diseases.

On the contrary, functional connectivity refers to the connectivity amongst different locations based on the statistical relationship between the brain signals. Functional connectivity is highly dynamical in nature (changes in tens or hundreds of milliseconds) since it depends upon the response of the brain to various stimuli and tasks. Hence, we can say that the structural brain network is static when compared to the functional brain network. Time-varying spatial network analysis is one of the popular tools which is used extensively in the area of brain research to analyse the dynamical functional connectivity of brain networks (Valencia *et al*. 2008; Dimitriadis *et al*. 2010; Doron *et al*. 2012; Cabral, Kringelbach and Deco 2017).

In Chapter 5, we perform time-varying spatial network analysis to examine the spatiotemporal dynamics of acoustic power sources during the different dynamical states of combustor operation. In time-varying network studies, the time series of an observable is divided into different windows or segments and a spatial network is constructed in each of these segments. However, in the present study, we construct a spatial network at each instant of time.

CHAPTER 3

ACQUISITION OF THE SPATIOTEMPORAL DATA

In this chapter, we shall discuss the experimental setup and the various measurement techniques used for the present study. We perform experiments on a laboratory-scale backward facing step combustor. We systematically vary the control parameter (equivalence ratio (φ)) and study the spatiotemporal dynamics at different dynamical states of combustor operation. To that end, we perform simultaneous pressure, OH* chemiluminescence and particle image velocimetry at different equivalence ratios.

3.1   TARA: THE EXPERIMENTAL RIG

The experimental setup, christened as **TARA** (**T**hermo-**A**coustic **R**ig for **A**xial Instability) consists of a settling chamber, a burner of 40 mm diameter and a combustion chamber of cross section 90 mm × 90 mm and length 1100 mm. The experimental setup is the same as the one used in the study of Nair and Sujith (2014) and Unni and Sujith (2017). The schematic of the experimental setup is shown in figure 3.1.

Air enters the test section through the settling chamber. A blow down mechanism is used to supply air from high pressure tanks. The air is passed through moisture separator before entering the settling chamber. It has to be noted that the air is not preheated in any of the experiments performed for the current study. The settling chamber is

provided to reduce the fluctuations in the inlet air. The fuel used in the experiments is liquefied petroleum gas (LPG, 40% Propane and 60% Butane) and it is introduced radially into the combustion chamber via four holes, each of diameter 1.7 mm, using a central shaft. The fuel injection location is 160 mm upstream of the bluff body. The partially premixed air - fuel mixture is spark ignited in the recirculation zone at the dump plane using an 11 kV ignition transformer. A circular disk of diameter 47 mm and a thickness of 10 mm is used for flame stabilization.
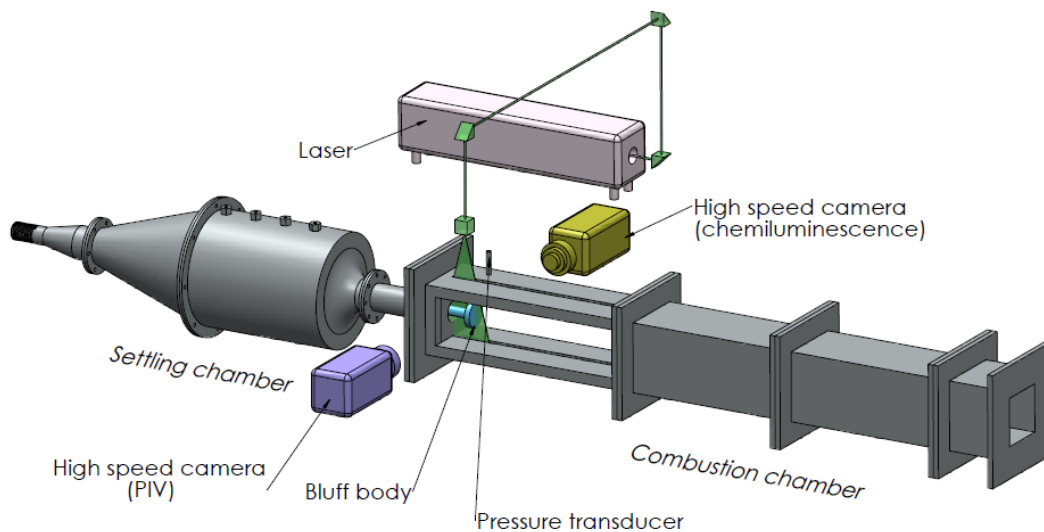
Figure 3.1: The schematic of the bluff body stabilized turbulent combustor used in the current study. The combustor's design is adapted from Komarek and Polifke (2010).

3.2   MEASUREMENTS

Mass flow controllers are used to measure and control the supply of fuel and air into the combustion chamber (Alicat Scientific, MCR Series, 100 SLPM model for fuel flow, 2000 SLPM for air flow; uncertainty is $\pm$ (0.8% of reading + 0.2 % of full scale). In the current study, we fix the fuel flow rate ($\dot{m}_f$) and gradually increase the air flow rate ($\dot{m}_a$), thus decreasing the equivalence ratio ($\varphi = (\dot{m}_f/\dot{m}_a)_{actual}$ /

$\left(\dot{m}_f/\dot{m}_a\right)_{stochiometry}$). The flow conditions are maintained such that the reactive flow is turbulent (Re ranges from 1.9×10^4 to 3×10^4, with an uncertainty ranging from ± 314 to ± 400). We measure the unsteady pressure (p') using a piezoelectric transducer (PCB 103B02, with a sensitivity of 223.4 mV/kPa and an uncertainty of ± 0.15 Pa), which is located at a distance of 20 mm from the dump plane. We acquire the acoustic pressure measurement for three seconds with at a sampling frequency of 10,000 Hz. A pair of quartz windows (400 mm $\times$ 90 mm $\times$ 10 mm) is provided in the side walls of the combustion chamber to facilitate optical diagnostics.

We capture the OH* chemiluminescence using a high-speed camera (CMOS, Phantom - v 12.1). The images are captured at a frame rate of 2000 Hz with a resolution of 800 $\times$ 600 pixels. We chose 500 μs as the exposure time. A ZIESS camera lens of focal length 50 mm, at f/2 aperture, is affixed to the camera. The measurement domain used for the current study has a physical dimension of 59 mm $\times$ 33 mm. The resolution of the measurement domain is 743 $\times$ 416 pixels. The above region is located at 28 mm downstream of the dump plane. An optical bandpass filter, with a peak at 308 nm and 12nm FMHW, is placed in front of the camera lens to capture the OH* chemiluminescence .We capture around 5000 images at different equivalence ratios as the thermoacoustic system transitions to thermoacoustic instability.

We obtain the Mie scattering images for the high speed PIV as follows. The flow is seeded with TiO_2 (Kronos make - product - 1071) particles of diameter 1 μm. We chose this size of the seeding particle such that it faithfully follows the fluid flow. However, the test section windows get clouded if we run the experiments for a long duration. Hence, at each run of an experiment, we record the data only for one or two equivalence

ratios. The flow is illuminated with a single cavity double pulsed Nd:YLF laser (Photonics) with a wavelength of 527 nm. The duration of a laser pulse is 110 ns. The repetition rate of each of the two pulses is 2000 Hz. We direct the laser beam towards the test section utilizing a combination of right angle prisms and a pair of convex lenses of focal length 500 mm and 50 mm, respectively. We use a spherical lens of focal length 600 mm and a cylindrical lens of focal length -16 mm to expand the laser beam into a sheet of thickness 2 mm. The laser sheet enters the test section through a narrow slit (400 mm length × 5 mm width) made up of quartz, located on top of the combustion chamber. The laser pulses have a time delay of 15-25 μs for different operating conditions of the combustor. This makes the maximum particle displacement between the two laser pulses to be roughly in the range of 4 to 7 pixels. Also, we make sure that the particle displacement is not more than $1/4^{th}$ of the length of the interrogation window (Raffel *et al*. 2007). We chose these parameters to prevent the loss of in plane particles during the analysis of PIV. We use another high-speed camera (CMOS, Photron FASTCAM SA4) to obtain the Mie scattering images. A ZEISS camera lens of 100 mm focal length, at f/5.6 aperture, is affixed to the camera. The camera is synchronized with the laser. We can operate the camera with a maximum resolution of 1024 × 1024 pixels. We capture the Mie scattering image pairs at a frame rate of 1000 Hz. The measurement domain of length 59 mm and width 33 mm, located at the centre span of the bluff body, covers a region of 968 × 541 pixels on the sensor. We place a bandpass optical filter (peak at 527 nm) in front of the camera to filter the flame and other background luminosity. The light scattered from the seeding particles is approximately spread over two pixels. We ensure a medium particle image density for all the flow rates.

We use PIVview software (Manual 2014) to process the Mie scattering images. We use a cross-correlation algorithm along with a least square gauss fit peak search scheme to calculate the velocity vectors (Raffel *et al*. 2007). We use a grid refining multi-pass approach for the cross-correlation algorithm. For high equivalence ratios (low flow rates), we started the multi-pass analysis with a grid area of 192×192 pixels and ended with a grid area of 32×32 pixels. We chose an overlap of 50% overlap between the interrogation windows. However, for lower equivalence ratios (higher flow rates), we started the analysis with a grid area of 192×192 pixels. The analysis ended with a grid area of 48×48 pixels after following four passes. This helped us to minimize the in-plane loss of correlation. We chose an overlap of 65% between the interrogation windows for these cases. Ideally, for the analysis of PIV, the pixel displacement has to be $1/4^{th}$ of the length of the interrogation windows. However, due to the medium seeding particle density, we could not reduce the area of the interrogation windows to achieve the ideal pixel displacement. Further reduction in the area of the interrogation window results in large number of outliers. We could not increase the seeding density as the quartz windows get clouded in a short period of time. The area of the grid and the percentage overlap is chosen such that we obtain, for all flow rates, the velocity field of roughly the same resolution. The vector spacing is around 1 mm for all the cases.

To detect the spurious vectors, we used post processing algorithms after following the above procedure. We detected the spurious vectors using two approaches namely, the maximum displacement test and the vector difference filter (Raffel *et al.* 2007). For the maximum displacement test, we need to choose appropriate thresholds for different equivalence ratios. The bulk flow velocity, at each equivalence ratio, is used as a reference to choose the thresholds. In the approach using vector difference filter, the

vector differences (only the magnitude) of a given vector to its neighbours (nearest eight neighbours) are calculated. If the vector difference is greater than one pixel, the given vector is considered as a spurious vector (Raffel *et al*. 2007). Following the above procedure, the number of spurious vectors detected were <1 % of all the velocity vectors. We then used bilinear interpolation to replace these spurious vectors. For the above procedure, estimation accuracies of the order of $1/10^{th}$ to $1/20^{th}$ of a pixel are acceptable for a grid area of 32×32 pixels, obtained from 8 bit images. In the present study, for high equivalence ratios, where the area of the interrogation window is 32×32 pixels, the uncertainty in velocity is roughly between 1.25 - 2.5% calculated using subpixel resolution (Raffel *et al*. 2007). However, for lower equivalence ratios, the uncertainty in velocity measurements could increase to 5% due to the use of 48×48 interrogation windows. For the current study, we present the data obtained from simultaneous acoustic pressure measurements, high speed flame imaging and PIV measurements at three different equivalence ratios corresponding to combustion noise ($\varphi = 0.98$), intermittency ($\varphi = 0.82$) and thermoacoustic instability ($\varphi = 0.63$) respectively.

CHAPTER 4

SPATIOTEMPORAL DYNAMICS OF THE TURBULENT REACTIVE FLOW FIELD

Before going into the investigation of spatiotemporal dynamics of the turbulent thermoacoustic system using network analysis, we shall first examine spatiotemporal dynamics of the turbulent reactive flow field. We obtain instantaneous velocity and vorticity field from the analysis of PIV. In this chapter, we shall investigate the velocity and vorticity fields of the turbulent reactive flow during combustion noise, intermittency and thermoacoustic instability.

4.1 SPATIOTEMPORAL DYNAMICS OF THE FLOW FIELD DURING COMBUSTION NOISE

During combustion noise, the fuel flow rate and air flow rate are maintained at 30 SLPM and 480 SLPM respectively ($\varphi = 0.98$). The low amplitude aperiodic pressure fluctuations characterizing combustion noise is depicted in figure 4.1 along with some instantaneous snapshots of the vorticity field superimposed on the velocity field corresponding to the points (a-e) marked on the pressure signal. The flow exiting the burner section enters the combustion chamber and gets deflected due to the presence of the bluff body. It further recirculates in the wake of both the bluff body and the dump plane. However, the magnitude of velocity in the wake of the bluff body is higher when

compared to that in the wake of the dump plane. During combustion noise, small vortices are shed in a random manner from the tip of the bluff body.
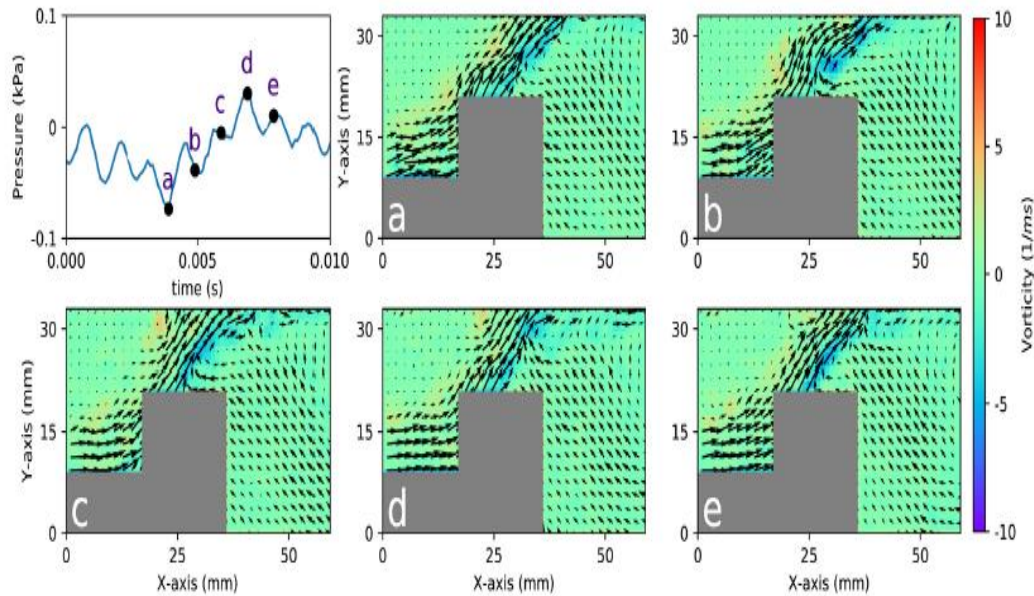
Figure 4.1: Instantaneous snapshots of the vorticity field superimposed on the velocity field corresponding to the points a-e marked on the time series of fluctuating pressure during combustion noise.

4.2 SPATIOTEMPORAL DYNAMICS OF THE FLOW FIELD DURING INTERMITTENCY

During intermittency, the air flow rate is increased to 570 SLPM, keeping the fuel flow rate constant ($\varphi = 0.82$). The flow dynamics during the aperiodic (figure 4.2a-c) and periodic regime (figure 4.2d-i) during intermittency is illustrated in figure 4.2. Compared to combustion noise, two major differences are observed in the flow dynamics during intermittency, specifically, during the periodic regime. Firstly, there is formation of coherent structures in the wake of the dump plane during periodic epochs of intermittency which is absent during the aperiodic epochs. Secondly, the

71

vortices shed from the tip of the bluff body is larger when compared to the ones shed during combustion noise and aperiodic regime of intermittency.
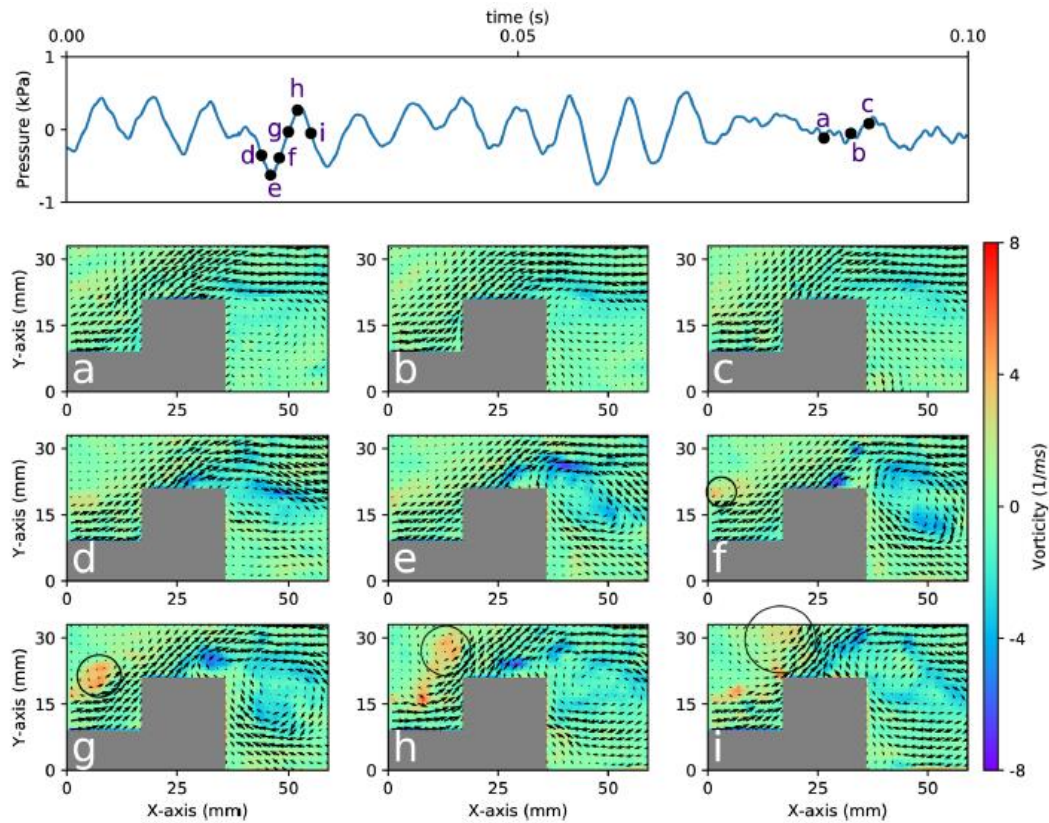
Figure 4.2: Instantaneous snapshots of the vorticity field superimposed on the velocity field during intermittency. During the aperiodic epoch of intermittency, large coherent structures are not observed [(a) – (c)]. However, during the periodic part of intermittency, we observe large coherent vortices in the flow field [(f) – (i)]. The black circles mark the vortices formed downstream of the dump plane convecting towards the combustor top wall.

4.3   SPATIOTEMPORAL DYNAMICS OF THE FLOW FIELD DURING THERMOACOUSTIC INSTABILITY

During thermoacoustic instability, we maintain the air flow rate at 750 SLPM and the fuel flow rate at 30 SLPM ($\varphi = 0.63$). The high amplitude periodic pressure fluctuations, with a frequency of 143 Hz, along with the instantaneous snapshots of the

72

flow field corresponding to one cycle of the periodic oscillation are shown in figure 4.3. We notice the periodic formation of large coherent structures in the wake of the dump plane similar to what is reported in earlier studies (Schadow and Gutmark 1992). These coherent structures convect downstream and impinge on the top wall of the combustor, enhancing fine scale mixing of unburned gases and hot radicals and leading to periodic bursts of high heat release rate oscillations.
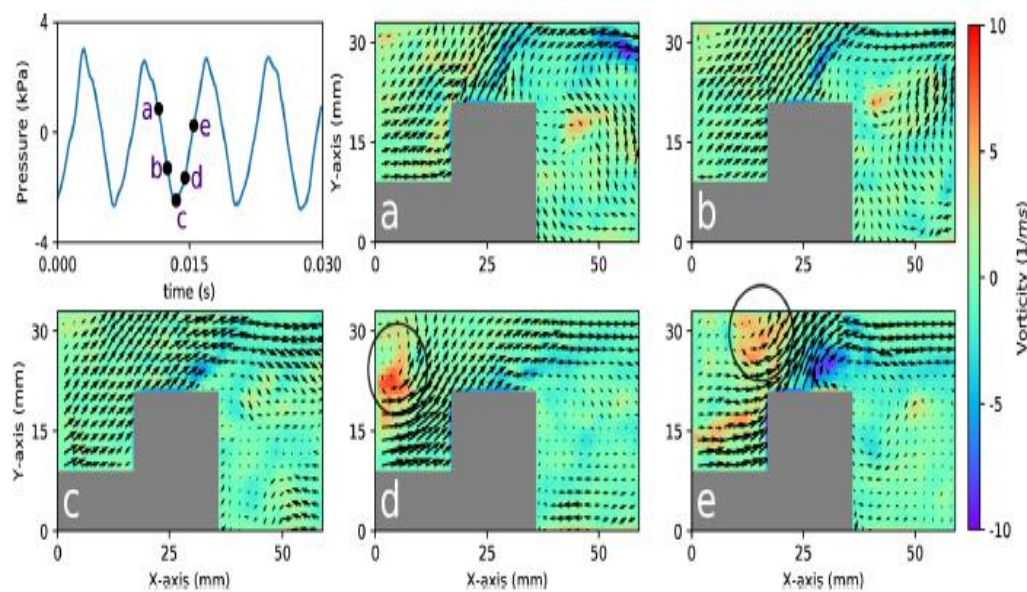
Figure 4.3: Instantaneous snapshots of the vorticity field superimposed on the velocity field corresponding to the points a-e marked on the time series of fluctuating pressure during one cycle of thermoacoustic instability.

4.4 THE AVERAGE FLOW FIELD

The acoustic power produced locally can be indicated by the distribution of the acoustic power production index (R_{xy}) of the reactive flow field defined as

$$R_{xy} = \int_0^t p'\dot{q}'(x,y)\, dt \qquad (4.1)$$

73
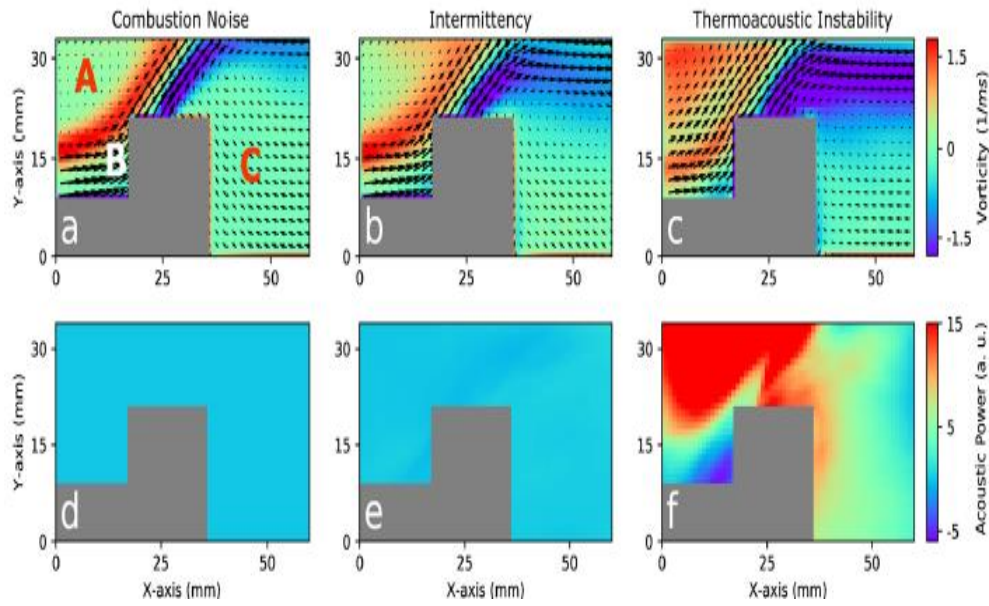
Figure 4.4: Average vorticity field superimposed on the average velocity field [(a), (b) and (c)] and the average acoustic power production index field [(d), (e) and (f)] during combustion noise, intermittency and thermoacoustic instability. During thermoacoustic instability, regions of high acoustic power production coincide with regions of high average vorticity present in the wake of the dump plane upstream of the bluff body.

where p' is the acoustic pressure and $\dot{q}'(x, y)$ is the unsteady heat release rate at the point (x, y). The average vorticity field superimposed on the average velocity field and R_{xy} during combustion noise, intermittency and, thermoacoustic instability are shown in figure 4.4. During combustion noise, in the average flow field, we observe that there are two shear layers present in the flow field – the outer shear layer marked by red colour and the inner shear layer marked by blue colour. These shear layers divide the flow field into three regions, namely, region A – wake of the dump plane, region B-the region between the outer and inner shear layer, called as shear zone and region C-the bluff body wake. Note that high average Rayleigh Index field during thermoacoustic instability coincides with high average vorticity field in the wake of the dump plane. In

the next chapter, we further explore this link by analysing the reactive flow field at the different dynamic regimes using time-varying spatial network analysis.

4.5   CONCLUSIONS

We examined the spatiotemporal dynamics of the flow field based on the analysis of PIV. We observed that during combustion noise, small vortices are shed from the tip of the bluff body. During thermoacoustic instability, we observe the periodic formation of large coherent structures downstream of the dump plane. During intermittency, we observe the signatures of both combustion noise and thermoacoustic instability. During the aperiodic epoch of intermittency, small vortices are shed from the tip of the bluff body and during the periodic epoch, we observed formation of coherent structures downstream of the dump plane.

CHAPTER 5

ON THE EMERGENCE OF LARGE CLUSTERS OF ACOUSTIC POWER SOURCES AT THE ONSET OF THERMOACOUSTIC INSTABILITY

During stable combustion, the acoustic power production happens in a spatially incoherent manner. In contrast, during thermoacoustic instability, the acoustic power production happens in a spatially coherent manner. In the present chapter, we investigate the spatiotemporal dynamics of acoustic power sources during the intermittency route to thermoacoustic instability using complex networks. We examine the spatiotemporal dynamics of acoustic power sources by constructing time-varying spatial networks during the different dynamical states of combustor operation.

5.1 NETWORK CONSTRUCTION

In order to study the spatiotemporal evolution of acoustic power sources, we perform simultaneous high-speed chemiluminescence (OH^*) imaging of the combustion zone, near the dump plane of the combustor, along with the acoustic pressure measurement at different equivalence ratios during the transition from combustion noise to thermoacoustic instability via intermittency. The OH^* chemiluminescence serves as a marker for the heat release rate from the flame as the OH^* intensity depends upon the chemical reaction rate (Hurle *et al.* 1968; Nori and Sietzman 2008). Even though the flow field is three dimensional inside the combustor, we analyse it in a two dimensional plane focussed on the central plane of the combustor, with a depth of focus of 9 mm.

The raw images of resolution 800 pixels $\times$ 600 pixels are cropped to a physical dimension of 57 mm $\times$ 33 mm, located at a distance of 28 mm downstream of the dump plane. We chose this region for the spatiotemporal analysis as it depicts interesting flow and flame dynamics during the different regimes of combustor operation (Unni and Sujith 2017).

We measure the unsteady pressure $p'(t)$ at a point near the dump plane. Nair (2014) has reported that the pressure variation across the combustion zone, in the present experimental setup, is very small. Hence, we assume the pressure to be constant in the measurement domain, at a given instant of time. In order to characterise the spatiotemporal evolution of acoustic power sources during a dynamical state of combustor operation, we multiply the unsteady heat release rate field $\dot{q}'(x, y, t)$, obtained from the OH^* chemiluminescence images, with the unsteady pressure at the corresponding time instant. In this manner, we obtain a series of 5026 $p'\dot{q}'$ images for a particular state of combustor operation. This is repeated for different equivalence ratios as the combustor transits from combustion noise to thermoacoustic instability via intermittency.

Each pixel of the $p'\dot{q}'$ image represents a local acoustic power source if the value of $p'\dot{q}'$ is positive or a local acoustic power sink if the value of $p'\dot{q}'$ is negative or zero. For the time-varying spatial network analysis, we consider each pixel of the $p'\dot{q}'$ image to be a node. Two nodes are connected if and only if the values of $p'\dot{q}'$ at these two nodes are positive. As we connect only those nodes where $p'\dot{q}'$ are positive, we track the spatiotemporal evolution of only the acoustic power sources. Since the turbulent combustor is a fluid mechanical system where energy transfer takes place locally amongst the fluid elements mainly due to convection, we consider only the nearest

neighbours n_i of a node (the distance between the nodes should not exceed $\sqrt{2}$) when establishing a link. This implies that a node can have a maximum of only eight links. The average value of $p'\dot{q}'$ at the two connecting nodes (i.e., where $p'\dot{q}'$ is positive and the distance between the nodes is less than or equal to $\sqrt{2}$) is considered as the weight of the link between them. In this manner, we construct 5026 time-varying weighted spatial networks for each equivalence ratio.

In order to characterize the spatiotemporal evolution of acoustic power sources, we use one of the basic weighted network measures - the node strength (Boccaletti *et al*. 2006). Node strength (s) of a given node i, is defined as the sum of the weights of the links of a node. It is given by

$$s_i = \sum_{j \in n_i} w_{ij} \tag{5.1}$$

where, i and j represent nodes of the network, w_{ij} the weight of the link connecting i and j and n_i represent the neighbourhood of the node i. A node having higher node strength implies that the links of the given node carry higher weights. Since, in the present study, the weight of the link refers to the average value of $p'\dot{q}'$ at the two connecting nodes, regions of high node strength represents regions of high local acoustic power production.

Apart from the acoustic power network (the network constructed from $p'\dot{q}'$ images), we also construct time-varying weighted spatial networks from the vorticity field, obtained from the analysis of PIV at each equivalence ratio. The interrogation windows used in the analysis of PIV are considered as the nodes of the vorticity network. Two nodes are connected if and only if the vorticity values at these nodes are either both positive or both negative. Similar to the acoustic power network, here also, we only

consider the nearest neighbours n_i of a node when establishing a link. The average vorticity value at the two connecting nodes is considered as the weight of the link between them. Positive values of node strength denote regions of counter clockwise vorticity and negative values of node strength denote regions of clockwise vorticity. In this way, we construct both the acoustic power and the vorticity network at every instant of time for each of the equivalence ratios as the turbulent combustor transits from combustion noise to thermoacoustic instability via intermittency.

5.2   RESULTS AND DISCUSSION

In the current study, we construct time-varying weighted local acoustic power and vorticity networks during combustion noise, intermittency and thermoacoustic instability. Using the measures from complex network theory, we first examine the spatiotemporal evolution of acoustic power sources visually and then obtain some statistical measures to quantify the dynamics.

5.2.1   Spatiotemporal Evolution of Acoustic Power Sources during Combustion Noise and Thermoacoustic Instability

We first examine the spatiotemporal evolution of the acoustic power sources during combustion noise (stable combustion) and thermoacoustic instability. The spatial distributions of the node strengths (Equation 5.1) of the acoustic power and the vorticity networks at different time instants during combustion noise are shown in figure 5.1. In the acoustic power network (figure 5.1b), the blue colour represents the local acoustic power sinks. The colourbar indicates the magnitude of node strength, which

corresponds to the local acoustic power production in the turbulent reactive flow field.

The spatial distribution of the node strength uncovers that the acoustic power
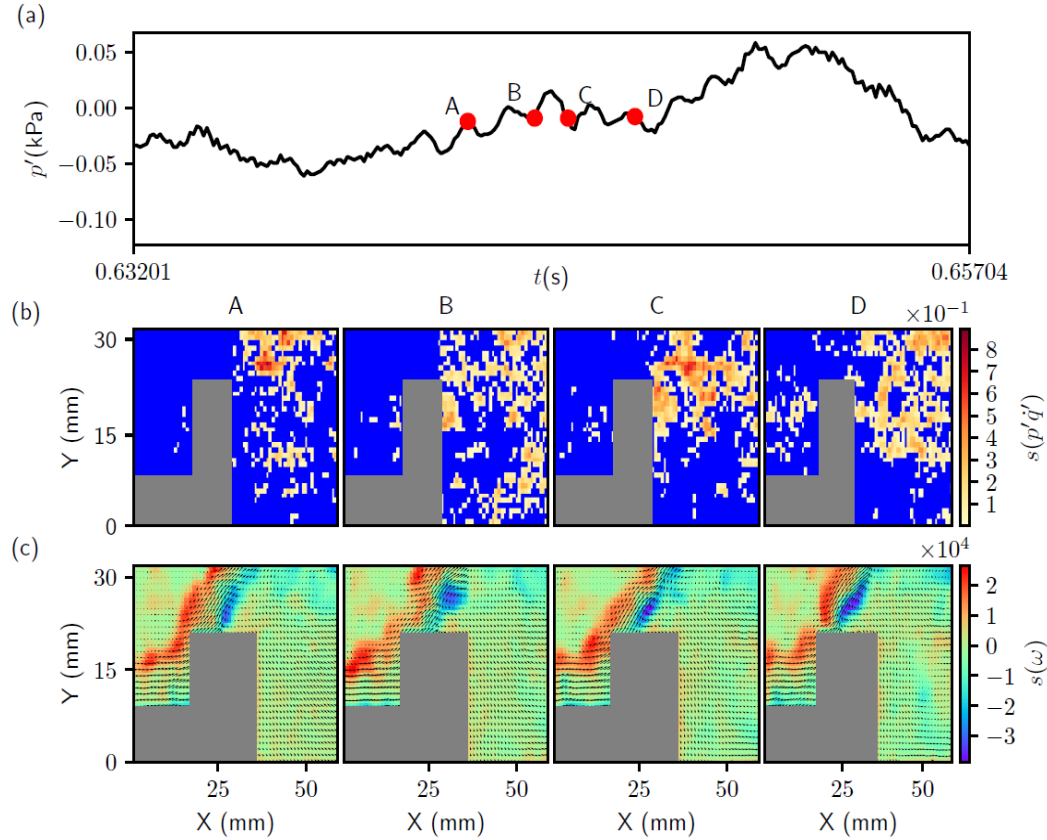
Figure 5.1. The spatial distribution of the node strengths of (b) the $p'\dot{q}'$ network and (c) the vorticity network at the corresponding time instants (A, B, C and D) marked on (a) the time series of fluctuating pressure during *combustion noise*. The blue region in the spatial distribution of the node strength of the acoustic power ($p'\dot{q}'$) network represents local acoustic power sinks. The colourbar in (b) represents the magnitude of the node strength, which indicates the average acoustic power produced in the neighbourhood of a node. The spatial distribution of the node strength shows that acoustic power production happens in small disconnected fragments during combustion noise. In the vorticity network (c), the node strength indicates the average vorticity in the neighbourhood of a node. Positive values of node strength represents vorticity distribution in the anti-clockwise direction whereas, negative node strength indicates the vorticity distribution in the clockwise direction. Velocity vectors are superimposed on the vorticity network to understand the flow field better. Small vortices are present in the outer shear layer as well as they are being shed from the tip of the bluff body. The grey colour rectangles in the subplots represent the bluff body.

production happens in small fragmented clusters during combustion noise. The distribution of the local acoustic power sources resembles small islands scattered in an ocean of acoustic power sinks. In the vorticity network (figure 5.1c), the node strength gives the average vorticity in the immediate neighbourhood of a node. Velocity vectors obtained from the analysis of PIV are superimposed on the vorticity network to understand the flow field better. High values of positive node strength (denoted by red colour) indicate the presence of a train of small discrete vortices in the outer shear layer. High values of negative node strength (denoted by blue colour) in the inner shear layer represents the small vortices shed from the tip of the bluff body. The grey colour mask in the subplots (figure 5.1b) and (figure 5.1c) represents the bluff body. The bluff body shape in (figure 5.1b) and (figure 5.1c) looks dissimilar due to the fact that in (figure 5.1b) the nodes are the pixels whereas in (figure 5.1c), the nodes are the interrogation windows used in the analysis of PIV. An interrogation window has 32×32 pixels. Hence, the area that a node occupies in (figure 5.1c) is bigger than that in (figure 5.1b). Also, in (figure 5.1c), the mask includes the region where laser reflection is high.

In figure 5.2, the spatial distributions of the node strengths of the acoustic power and the vorticity networks at different time instants during a periodic cycle of thermoacoustic instability are shown. Unlike the situation during combustion noise, the acoustic power production happens now in large clusters during thermoacoustic instability (figure 5.2b). The acoustic power production during thermoacoustic instability is around three orders of magnitude higher than that during combustion noise, as indicated by high values of node strength. High values of positive node strength in the vorticity network (at time instant *A* and *B* in figure 5.2c), coincides with the centre of the coherent structure being formed downstream of the bluff body. The coherent structure begins to form at the dump plane, when the acoustic pressure

fluctuation is near local minima (*E*). As the coherent structure convects downstream it grows in size. The formation of large coherent structures at the onset of thermoacoustic instability has been reported in earlier studies as discussed in Chapter 1. The maximum acoustic power production occurs when the large coherent structure impinges on the top combustor wall.

Figure 5.2. The spatial distribution of the node strengths of (b) the acoustic power network and (c) the vorticity network at the corresponding time instants (A, B, C, D and E) marked on (a) the time series of oscillating pressure during *thermoacoustic instability*. The spatial distribution of the node strength of the acoustic power network indicates that during thermoacoustic instability, the acoustic power production occurs in large clusters. The high values of positive node strength of the vorticity network coincide with the centre of the coherent structure formed downstream of the dump plane. The maximum acoustic power production occurs when the coherent structure impinges on the top wall of the combustor (C). The magnitude of acoustic power production during thermoacoustic instability is almost three orders of magnitude higher than that during combustion noise as indicated by the node strength of the acoustic power network.

As the coherent structure convects towards the top of the bluff body (from time instants *A* to *C* in figure 5.2c), the region between the outer and inner shear layer is compressed against the rear-end of the bluff body. This increase in the shear strain leads to local extinction (Hult *et al.* 2005). This may be the reason for almost no reaction to take place just upstream of the bluff body leading to the presence of local acoustic power sinks in the rear-end of the bluff body, above the bluff body shaft. As the coherent structure passes over the top of the bluff body, separation of the inner shear layer from the tip of the bluff body happens. This suggests the frequency of formation of the coherent structure downstream of the dump plane and the large vortex from the tip of the bluff body to be almost identical. High values of negative node strength in the vorticity network indicate the shedding of these large vortices from the tip of the bluff body. As the large vortex convects downstream of the bluff body, the region between the outer and the inner shear layer expands. This is accompanied by a flow reversal at the bluff body due to volume expansion because of intense heat release as well as the reversal of acoustic velocity. This inhibits the flow of fresh reactant mixture into the combustion zone. This is the reason why we have large clusters of acoustic power sources in the flow field when the acoustic pressure fluctuation is negative (see time instants *E* and *A* in figure 5.2b). When the pressure inside the combustion chamber becomes very low, the flow surges back into the combustion chamber. As the acoustic mode is reinforced by the intense in-phase heat release rate, the velocity fluctuation amplitude increases. This induces the formation of large coherent structure downstream of the dump plane and the cycle continues.

5.2.2 Spatiotemporal Evolution of Acoustic Power Sources during Intermittency

Next, we examine the spatiotemporal evolution of the acoustic power sources during intermittency. Intermittency can be viewed, in simple terms, as a tug of war between the acoustic driving and the acoustic damping present in the system. As the acoustic driving wins over the damping, the growth of the acoustic pressure oscillations occurs. As the damping overtakes the driving, these high amplitude acoustic pressure oscillations start to decay. It is this competition between the acoustic driving and the damping, which leads to the emergence of bursts of high amplitude periodic oscillations in the background of low amplitude aperiodic pressure oscillations during intermittency.

In this section, we will see how spatially continuous large clusters of acoustic power sources emerge at the onset of thermoacoustic instability from the small fragmented clusters of acoustic power sources observed during combustion noise. To that end, we investigate the spatial and temporal evolution of acoustic power sources during an aperiodic epoch of intermittency, a periodic epoch of intermittency, the growth of low amplitude aperiodic pressure fluctuations to high amplitude periodic oscillations and the decay of high amplitude periodic pressure oscillations to low amplitude aperiodic fluctuations. In figure 5.3, we show the spatiotemporal evolution of acoustic power sources during an aperiodic epoch of intermittency. In this case, similar to the one observed during combustion noise, the acoustic power production happens in small fragmented clusters or islands scattered in an ocean of acoustic power sinks.

Next, we examine the spatiotemporal evolution of acoustic power sources during a periodic epoch of intermittency, as shown in figure 5.4. We observe coherent structures

84
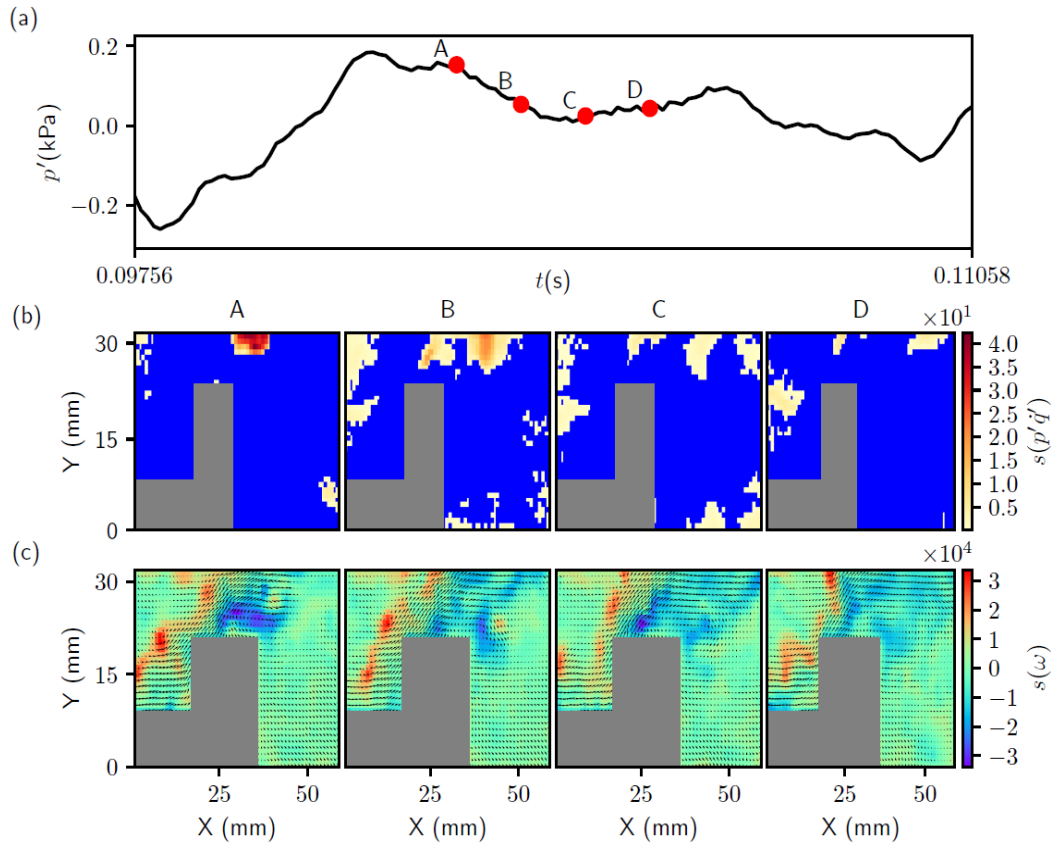
Figure 5.3. The spatial distribution of the node strengths of (b) the acoustic power network and (c) the vorticity network at the corresponding time instants (A, B, C, D and E) marked on (a) the time series of fluctuating pressure during the *aperiodic regime of intermittency*. The acoustic power production happens in small fragmented clusters as in the case of combustion noise.

downstream of the dump plane, as seen during thermoacoustic instability. However, there are a few points to be noted here. Firstly, the size and strength of the coherent structure are not as high as the one observed during thermoacoustic instability. George *et al.* (2018) has quantitatively measured the size of the coherent structures during the different stages of combustor operation using vortex detection technique. Also, the strength of the coherent structure, which is reflected in the magnitude of the positive node strength, is lower than that during thermoacoustic instability. More significantly,

85

the coherent structure impinges on the rear-end tip of the bluff body (see time instant C

in figure 5.4c) and not on the top wall of the combustor. After impingement, the
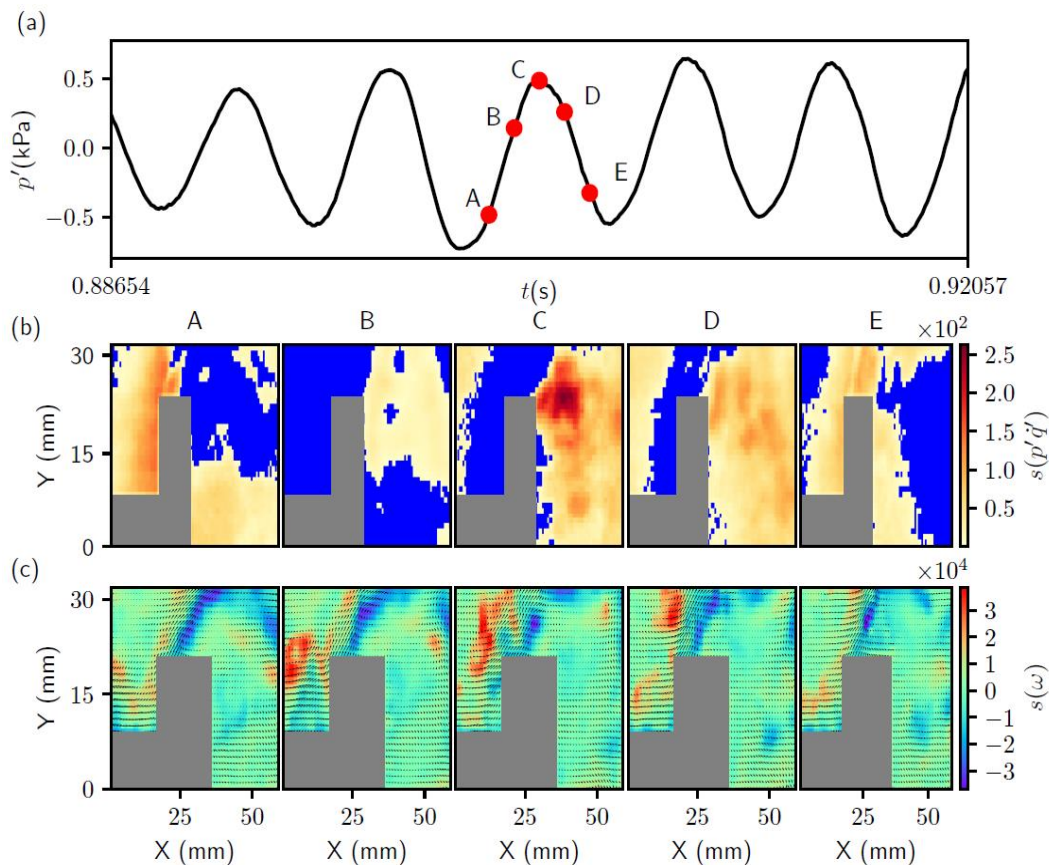
Figure 5.4. The spatial distribution of the node strengths of (b) the acoustic power network and (c) the vorticity network at the corresponding time instants (A, B, C, D and E) marked on (a) the time series of fluctuating pressure during the *periodic regime of intermittency*. The acoustic power production occurs in large clusters as in the case of thermoacoustic instability. However, unlike the case during thermoacoustic instability, the coherent structure impinges the rear-end tip of the bluff body. After impingement, the coherent structure disintegrates into small vortices that convect over the top of the bluff body.

coherent structure breaks down into small vortices. Since the area of impingement of

the coherent structure is lower, the heat release rate that follows is not as intense as in

the case of thermoacoustic instability. It is to be noted that these coherent structures are

not consistently observed during the periodic epochs of intermittency. They are mostly

observed during the high amplitude peaks of the periodic epochs of intermittency. Here also, we observe the shedding of large vortices from the tip of the bluff body. It is to be noted that the size of the cluster of the acoustic power source is not as large as that observed during thermoacoustic instability.
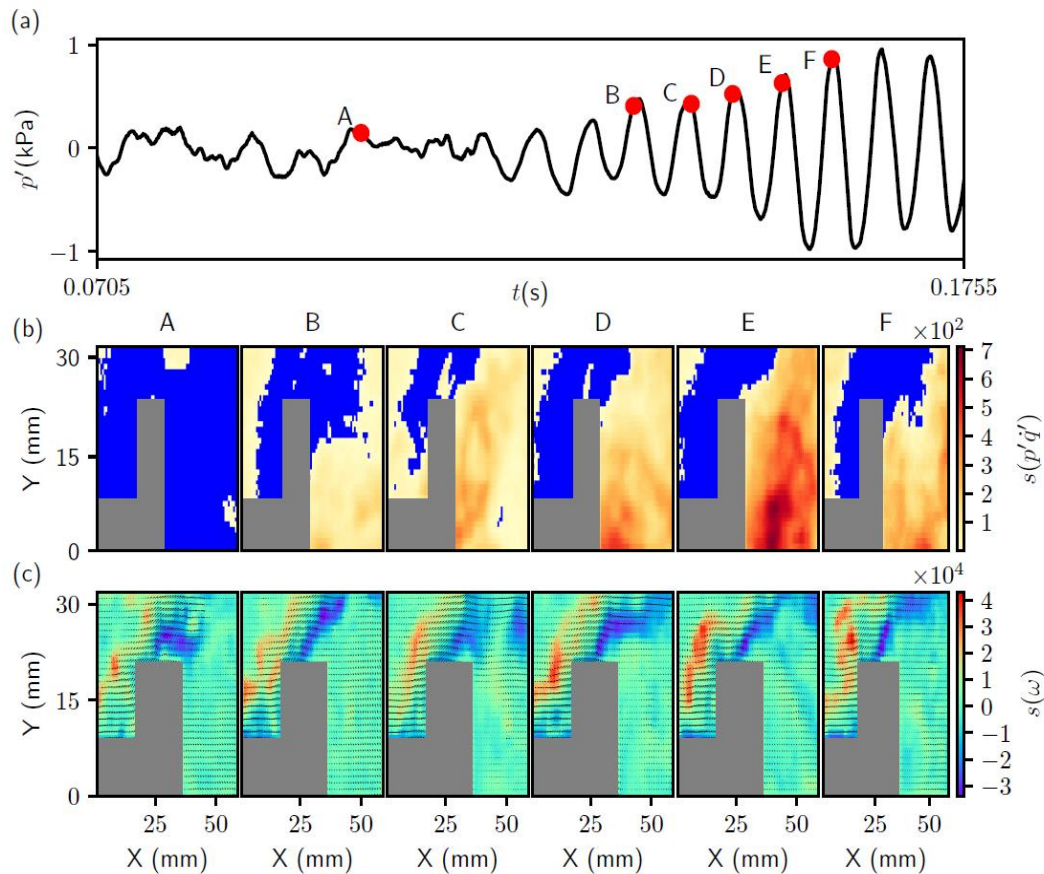
Figure 5.5. The spatial distribution of the node strengths of (b) the acoustic power network and (c) the vorticity network at the corresponding time instants (A, B, C, D, E and F) marked on (a) the time series of fluctuating pressure during the *growth of pressure oscillations observed during intermittency*. As the thermoacoustic system transits from low amplitude aperiodic oscillations to high amplitude periodic oscillations during intermittency, the acoustic power sources nucleate, coalesce and grow in size and strength of acoustic power production also increases.

In order to understand how large clusters of acoustic power sources emerge in the flow field during the periodic epoch of intermittency, we examine the spatiotemporal evolution of the acoustic power sources during the growth of low amplitude aperiodic fluctuations to high amplitude periodic oscillations, as shown in figure 5.5. As the pressure oscillations grow, we find the emergence of acoustic power sources at more number of spatial locations in the turbulent reactive flow field. We refer to this phenomenon as the nucleation of acoustic power sources in the flow field. Also, as the acoustic pressure amplitude grows, the small fragmented clusters of acoustic power sources coalesce to form large clusters, as reflected in the spatial distribution of the node strength of the acoustic power network (figure 5.5b). The mechanism behind the formation of these large clusters can be deduced by examining the vorticity network (figure 5.5c). As the acoustic pressure grows, the magnitude of the positive as well as the negative node strength increases; this denotes the increase in the strength of the vorticity field upstream and downstream of the bluff body respectively.

During the aperiodic epoch of intermittency, a train of small discrete vortices is observed in the outer shear layer downstream of the dump plane. At the same time, small vortices are shed downstream of the bluff body as the inner shear layer gets separated from the tip of the bluff body. As the perturbations near the dump plane increase, these small vortices in the outer shear layer merge to form large vortices. Merging of vortices leads to an increase in fine scale mixing that accelerates combustion (Schadow *et al.* 1987), thus causing the nucleation of acoustic power sources in the flow field. In addition, as the small vortices merge, coalescence of small fragmented clusters of acoustic power sources occurs. These large vortices convect downstream of the dump plane and impinge on the rear-end tip of the bluff body. Upon impingement, a spike occurs in the heat release rate due to the sudden increased fine

scale mixing of the reactants and hot products. This spike in the heat release rate adds energy to the acoustic field, thus acting as a kicked oscillator (Seshadri, Nair and Sujith 2016). Since the heat release rate occurs in phase with the acoustic pressure oscillation, the amplitude of the acoustic pressure increases satisfying Rayleigh criteria. This reinforcement of the acoustic mode leads to an increase in the amplitude of velocity fluctuations at the dump plane thus inducing the formation of a new vortex and the aforementioned cycle continues. When the perturbation in the flow field is high enough, a large coherent structure forms downstream of the dump plane, gets convected and impinges on the top wall of the combustor. As the large coherent structure carries with it a large pocket of unburnt reactants, upon impingement, the heat release rate is higher. Hence, the energy added to the acoustic field overcomes the damping present in the combustor and the onset of thermoacoustic instability occurs. We note that the convection of the large vortex towards the rear-end tip of the bluff body/top wall of the combustor perturbs the inner shear layer more and hence the size of the vortices shed downstream of the bluff body also increases.

Finally, we examine the spatiotemporal evolution of acoustic power sources during the decay of high amplitude periodic pressure oscillations to low amplitude aperiodic pressure fluctuations, as shown in figure 5.6. During the high amplitude periodic pressure oscillations, the acoustic power production occurs in large clusters, as evident at time instant *A*. As the acoustic damping overcomes the acoustic driving in the combustor, the amplitude of the pressure oscillation decays. As the thermoacoustic system transits from high amplitude periodic oscillations to low amplitude aperiodic fluctuations, the strength of acoustic power production diminishes and the large clusters disintegrate into small fragmented clusters.
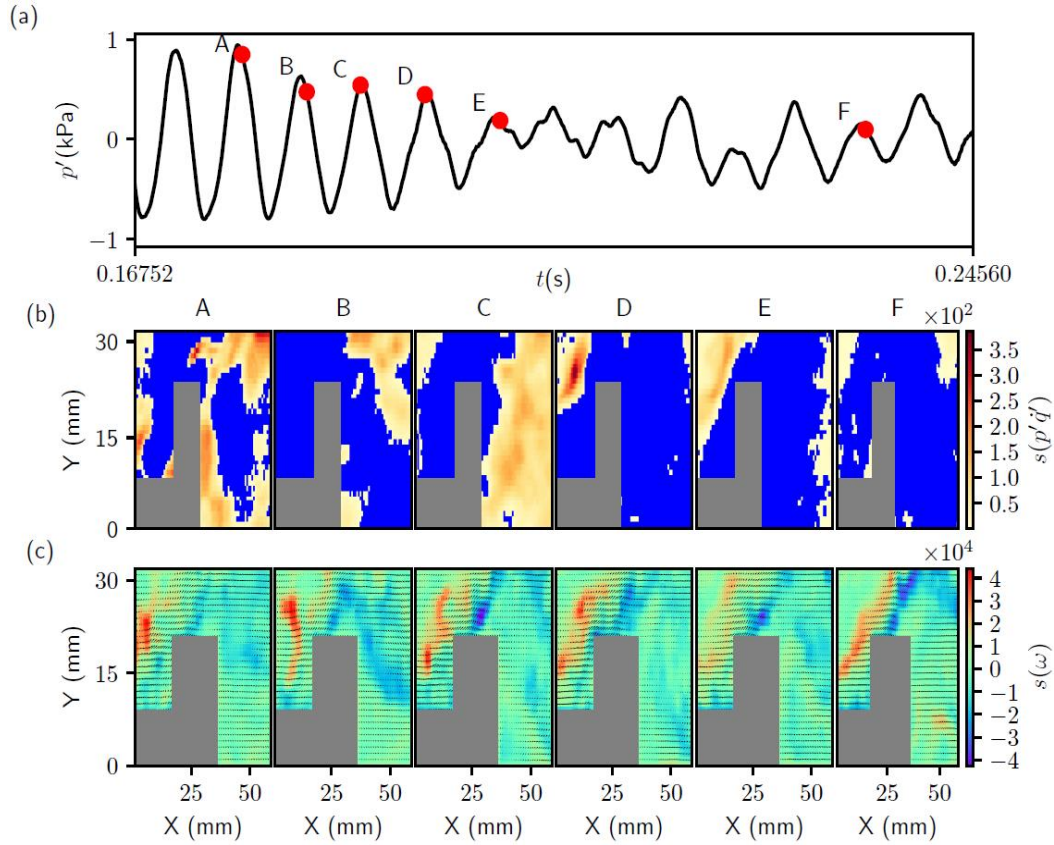
Figure 5.6. The spatial distribution of the node strengths of (b) the $p'\acute{q}'$ network and (c) the vorticity network at the corresponding time instants (A, B, C, D, E and F) marked on (a) the time series of fluctuating pressure during the *decay of pressure oscillations observed during intermittency*.

The decay of the acoustic pressure amplitude during intermittency begins to occur once the damping in the turbulent combustor starts to outweigh the acoustic driving. As the damping overcomes the driving, the roll-up of the shear layer into a large vortex, observed during the periodic epochs of intermittency, fails to happen thus ceasing the formation of large clusters of acoustic power sources. Hence, the amount of energy added to the acoustic field reduces. Henceforth, the periodic epochs of intermittency fail to persist and decay, thus preventing the onset of full blown thermoacoustic instability.

5.2.3   Statistical Analysis of the Clusters of Acoustic Power Sources

In this section, we examine a statistical analysis of the clusters of acoustic power sources as the thermoacoustic system transits from a state of combustion noise to thermoacoustic instability via intermittency. The use of complex network theory enables us to quantify the spatiotemporal evolution of the clusters of acoustic power sources. To that end, we calculate the link density (ρ), the size of the giant cluster (S) and the number of clusters (N) at different equivalence ratios as the combustor transits from combustion noise to thermoacoustic instability.

Link density refers to the fraction of the links or edges present in the network. If n represents the total number of nodes and e represents the actual number of links in the network, then, link density is given by

$$\rho = \frac{2e}{n(n-1)} \tag{5.2}$$

The value of ρ lies between 0 and 1. In simple terms, ρ reflects the number of connections among the nodes of the network. A high value of ρ implies that the network is densely connected and a low value implies that the network is sparsely connected. In the present analysis, a high value of ρ implies that acoustic power production happens in a large number of spatial locations in the flow field as we do not consider acoustic power sinks in the network construction, as explained in section 5.1.

In graph theory, a connected component of an undirected graph refers to a sub-graph in which any two nodes are connected to each other by a path, i.e., a sequence of links (Newman 2010). In the present study, the connected components refer to islands or clusters of acoustic power sources. We track the number of such clusters (N) as well

as the size of the giant cluster (S); i.e., the largest connected component of a graph, at each instant of time. In this manner, we obtain, for a given equivalence ratio, ρ, N and S at every instant of time. Thus, for each equivalence ratio, we construct 2000 acoustic power networks, corresponding to a duration of 1.0 s, as described in section 5.1.
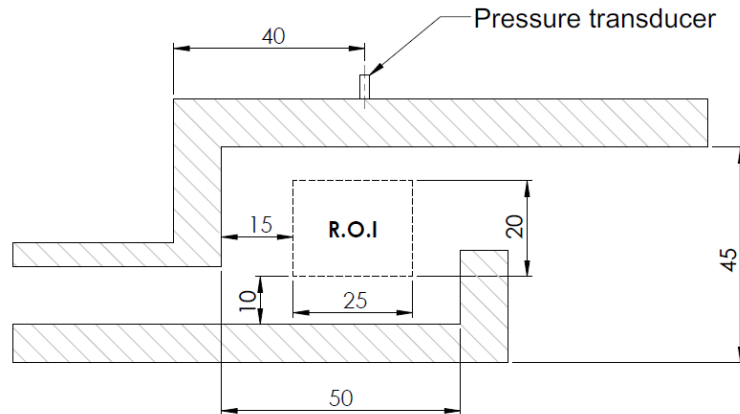
Figure 5.7. Half cross-section of the combustion chamber showing the region of interest (R.O.I), in which the acoustic power network is constructed to compute the network properties. The region of interest is chosen such that it coincides with the location of formation of coherent structures downstream of the dump plane. The pressure transducer used for the acoustic pressure measurement is located 40 mm downstream of the dump plane.

Since most of the interesting flow dynamics leading to the coalescence/disintegration of clusters happens upstream of the bluff body, we choose a rectangular region of interest (R.O.I) upstream of the bluff body for the acoustic power network construction. The chosen region of interest, at a distance of 15 mm downstream of the dump plane and 10 mm above the bluff body shaft, has a physical dimension of 25 mm in length and 20 mm in breadth (figure 5.7). The region of interest has a resolution of 225×180 pixels. Since the calculation of network properties with the original resolution will be computationally very intensive, we down-sampled the resolution to 112×90 pixels

(50% of the original resolution) using a bi-cubic interpolation (Zhnag *et al.* 2011).

Hence, the number of nodes in the network reduces from 40,500 to 10,080. Also, a

small threshold (ϵ) was introduced for the connections among the nodes to prevent the

electronic noise of the high speed camera used for chemiluminescence measurements

to creep into the calculation, especially during combustion noise. We choose the

threshold for network link connectivity as $\epsilon = 1.0$ (around 5% of the maximum

acoustic power production during combustion noise). Hence, two neighbouring nodes

are connected if the values of $p'\dot{q}'$ at these nodes are greater than 1.0 instead of 0.0

(without any threshold). The sensitivity of the network properties for different

thresholds of network link connectivity (ϵ) and the convergence of the network

properties with respect to the number of images/networks considered for their

calculation are discussed in Appendix (see figure A1 and A2). In this study, we use the

networkx python package to calculate the network properties (Hagberg, Swart and

Chult 2008).

Figure 5.8 illustrates the variation of the temporal mean of ρ (figure 5.8a), S (figure

5.8b) and N (figure 5.8c) of acoustic power sources at seven different equivalence ratios

that cover the transition of the thermoacoustic system from combustion noise to

thermoacoustic instability via intermittency. The dashed vertical lines in the plot

separate the combustor operational regime into combustion noise, intermittency and

thermoacoustic instability respectively. The variation of the root mean square (rms)

value of the acoustic pressure is also plotted along with the variation of the network

properties. As the thermoacoustic system transits from combustion noise to

thermoacoustic instability, the average ρ increases seven-fold. This implies that the

average number of links during thermoacoustic instability is around seven times that
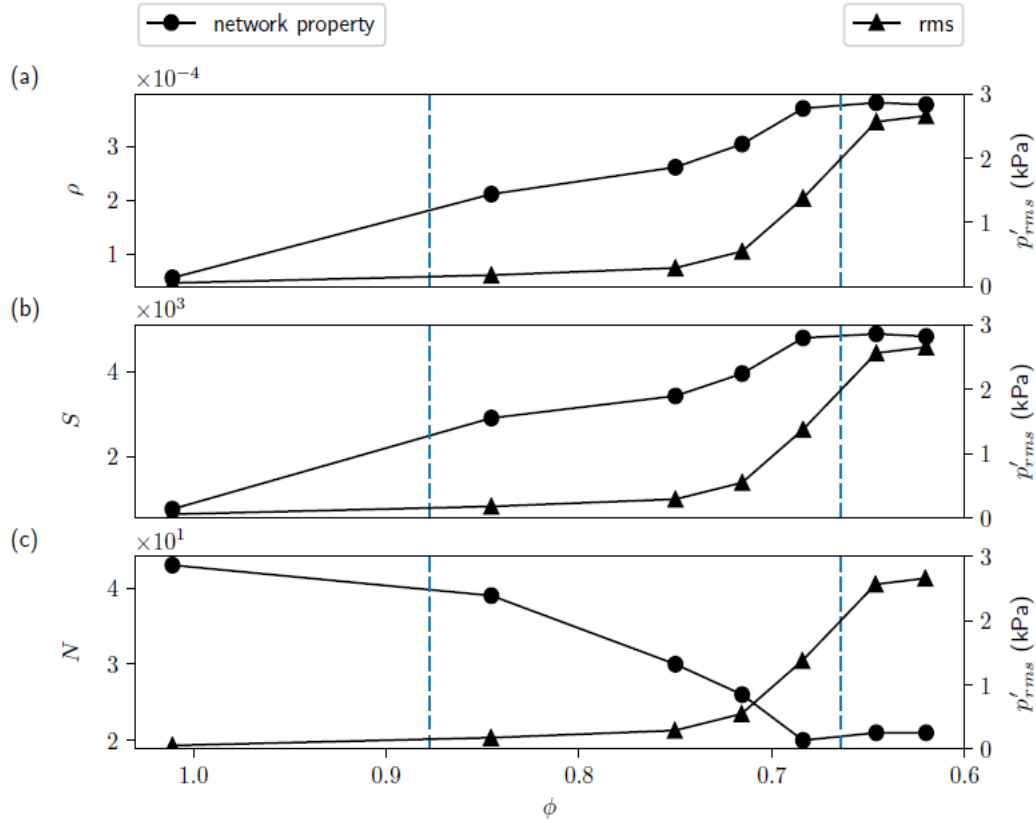
Figure 5.8. Variation of the temporal mean of the network properties (a) the link density (ρ), (b) the size of the giant cluster (S) and (c) the number of clusters (N) along with the variation of the root mean square value (rms) of the acoustic pressure as the thermoacoustic system transits from combustion noise to thermoacoustic instability via intermittency. The increase in the link density indirectly indicates the increase in the number of locations in the flow field where acoustic power production occurs. The increase in the size of the giant cluster along with the decrease in the number of clusters show that the acoustic power sources coalesce to form large clusters at the onset of thermoacoustic instability. The dashed vertical lines divide the parameter space, i.e., the equivalence ratio (φ), into regimes of combustion noise, intermittency and thermoacoustic instability respectively.

during combustion noise (Equation 5.2). A higher value of the average number of links during thermoacoustic instability implies that the acoustic power production occurs at a large number of locations in the flow field when compared to that during combustion noise. This reflects the phenomenon of nucleation of acoustic power sources occurring in the turbulent reactive flow field. The very low value of the average ρ (the maximum

value is around 0.0004) is due to the fact that only the nearest neighbours of a node are considered when establishing a link, as mentioned in section 5.1.

During combustion noise, the acoustic power production happens mostly in a large number of fragmented clusters or islands in an ocean of acoustic power sinks. This explains the presence of a large number of clusters of acoustic power sources during the occurrence of combustion noise in figure 5.8 (c). Mondal *et al.* (2017) attributed this spatial incoherence in the acoustic power production to the random distribution of instantaneous phase between the acoustic pressure and the unsteady heat release rate fluctuations during the state of combustion noise. Also, the average S (in figure 5.8b), is very small during combustion noise as the acoustic power production occurs in small fragmented clusters. The average S during thermoacoustic instability is approximately six times the value observed during combustion noise. Additionally, we observe only half the average N at the onset of thermoacoustic instability when compared to that during combustion noise. These observations clearly show that the large number of fragmented clusters of acoustic power sources observed during combustion noise coalesce to form large clusters at the onset of thermoacoustic instability.

Figure 5.9 shows the variation of the standard deviation of ρ (figure 5.9a), S (figure 5.9b) and N (figure 5.9c) of acoustic power sources along with the variation of the root mean square (rms) value of the acoustic pressure. During combustion noise, there are instances where large clusters of acoustic power sources are present in the flow field upstream of the bluff body. However, these large clusters having positive values of $p'\dot{q}'$ occur mostly when the acoustic pressure fluctuation is negative. During combustion noise, most of the reaction occurs in the recirculation zone downstream of the bluff
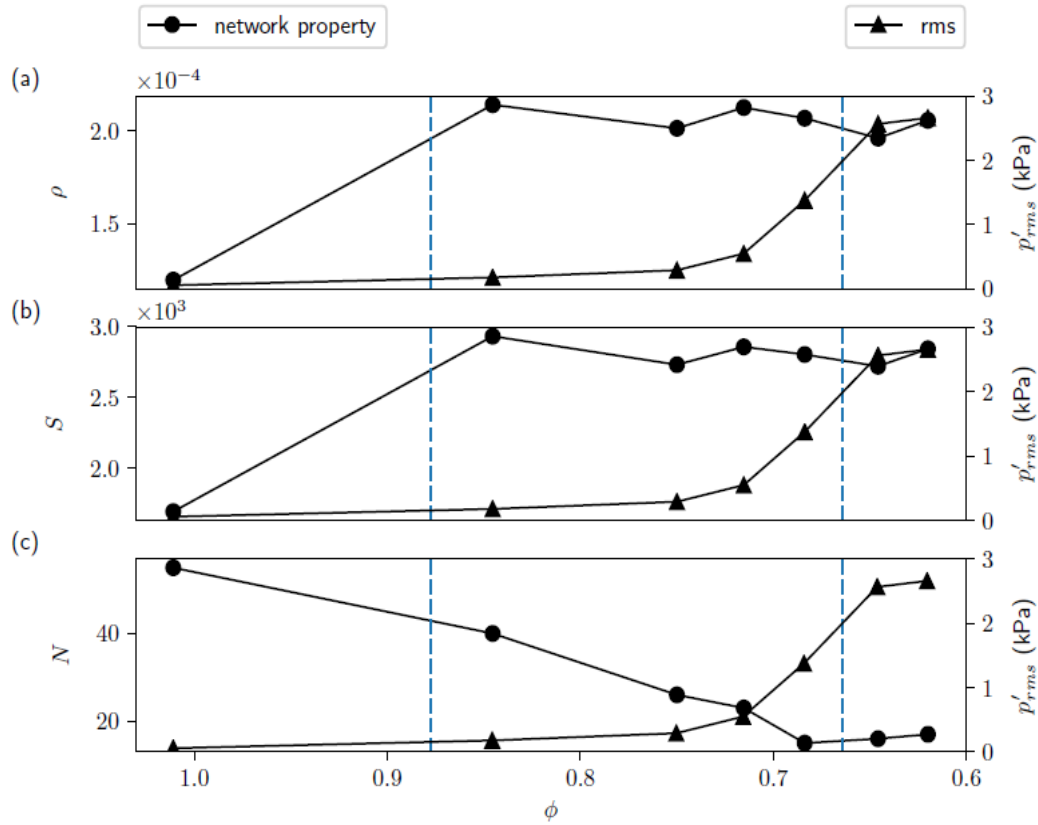
Figure 5.9. Variation of the standard deviation of the network properties (a) the link density (ρ), (b) the size of the giant cluster (S) and (c) the number of clusters (N) along with the variation of the root mean square (rms) value of the acoustic pressure as the thermoacoustic system transits from combustion noise to thermoacoustic instability via intermittency. The dashed vertical lines divide the parameter space, i.e., the equivalence ratio (φ), into regimes of combustion noise, intermittency and thermoacoustic instability respectively.

body. In the region of interest considered for the calculation of the network properties, which is upstream of the bluff body, not much reaction happens most of the time. Hence, when the acoustic pressure fluctuation (p') and the local heat release rate fluctuation ($\dot{q}'$) become negative simultaneously, we observe large clusters of acoustic power sources (positive values of $p'\dot{q}'$) upstream of the bluff body. This explains the high value of the standard deviation for ρ, S and N during combustion noise. However, we observe high values of standard deviation only for ρ and S during intermittency.

This can be attributed to the fact that we observe small fragmented clusters of acoustic power sources during the aperiodic epochs of intermittency and large clusters of acoustic power sources during the periodic epochs of intermittency. The standard deviation for the number of clusters of acoustic power sources is low during thermoacoustic instability compared to that during combustion noise (figure 5.9c). As discussed earlier, during thermoacoustic instability, the acoustic power production happens mostly in large clusters. Hence, the average number of clusters (see figure 5.8c) as well as the standard deviation (figure 5.9c) is low during thermoacoustic instability. During one acoustic cycle, when the coherent structure convects out of the region of interest, towards the top of the bluff body, there will not be much acoustic power sources inside the region of interest. This is the reason for high value of standard deviation for link density (figure 5.9a) and the size of the giant cluster (figure 5.9b) during thermoacoustic instability.

We note that the gradual change in the average network properties happens much before the rise in the root mean square (rms) of the acoustic pressure as the thermoacoustic system transits from combustion noise to thermoacoustic instability via intermittency. This suggests that the transition from small fragmented clusters to large clusters of acoustic power sources is not abrupt. In statistical physics, percolation theory is used in lattice models to study the phenomenon of phase transition. The variation of the size of the giant cluster is used as a marker to study the critical behaviour near the percolation threshold (Newman 2010, Barabasi 2016). Using complex network theory, researchers have reported percolation-like phase transitions in brain networks (Gallos, Makse and Sigman 2012; Fornito, Zalesky and Bullmore 2016), protein networks (Deb, Vishveshwara and Vishveshwara 2009; Weber and Pande 2015) and recently in climate networks (Lu, Yuan and Fu 2016). Henceforth, in the present study, the variation of

the average size of the giant cluster (see figure 5.8 b) reveals a continuous percolation-like phase transition at the onset of thermoacoustic instability in a turbulent combustor. Since the large clusters of acoustic power sources begin to form during the periodic regime of intermittency, we can hypothesize that the disruption of these large clusters might prevent the transition to an impending thermoacoustic instability in the present combustor. However, a detailed analysis is required to confirm whether this is the case in turbulent combustors with other flame stabilisation mechanisms.

5.3   CONCLUSIONS

We used time-varying spatial network analysis of the local acoustic power and the vorticity field in a turbulent combustor with a bluff body stabilised flame during the transition from combustion noise to thermoacoustic instability via intermittency. We find that during combustion noise the acoustic power production occurs in small fragmented clusters whereas, during thermoacoustic instability, the acoustic power production happens coherently in large areas. This spatial emergence of large clusters of acoustic power production occurs via nucleation, coalescence and growth of acoustic power sources as the acoustic pressure grows during intermittency. As the acoustic pressure decays, the large clusters of acoustic power sources disintegrate into small fragmented clusters. The presence of large clusters of acoustic power sources during the periodic epochs of intermittency persuades the authors to hypothesize that the disruption of these large clusters can prevent an impending thermoacoustic instability. We quantify the spatiotemporal evolution of the acoustic power sources using network measures such as the link density, the size of the giant cluster and the number of clusters of acoustic power sources. An increase in the link density as well as the size of the giant cluster along with a decrease in the number of clusters corroborate our findings. A

continuous increase in the size of the giant cluster suggests that the onset of thermoacoustic instability in a turbulent combustor can be viewed as a percolation-like phase transition. The approach presented here can be utilized to study the spatiotemporal evolution of acoustic power sources in combustors with other flame stabilization mechanisms.

CHAPTER 6

CHARACTERIZING VORTICITY INTERACTIONS DURING THE INTERMITTENCY ROUTE TO THERMOACOUSTIC INSTABILITY

The spatiotemporal dynamics of the turbulent reactive flow field is different during the different dynamical states of combustor operation. During combustion noise, we observe the presence of small vortices in the outer and inner shear layers. At the onset of thermoacoustic instability, we observe the periodic formation of coherent structures downstream of the dump plane. The aim of the present study is to characterize the vorticity interaction occurring in the flow field during the different states of combustor operation using network analysis. During combustion noise, we find that the vorticity interaction network is characterized by a weighted scale-free network. The topology of the network is scale-free during the aperiodic and periodic epochs of intermittency. However, during an acoustic cycle thermoacoustic oscillations, the vortical-interaction network oscillates between random and scale-free behaviour.

6.1   NETWORK CONSTRUCTION

In a turbulent flow, the vortical interactions take place over a large number of length and time scales. The velocity induced by these vortices makes the turbulent flow chaotic

(Tennekes and Lumley 1972; Pope 2000). Nair, Taira and Brunton (2016) used complex network theory to unmask the underlying structure of these vorticity interactions in a two-dimensional decaying isotropic turbulence. They observed that the turbulent flow has a scale-free network structure. The scale-free structure makes the turbulent network to be resilient against random attacks but, vulnerable against targeted attack on the hub vortices. This opens up a new approach for modifying the collective dynamics of turbulent flows. In the present study, we follow their work for network construction and characterisation of turbulent reactive flow field.

We divide the turbulent reactive flow field into Cartesian cells. We obtain the vorticity at each of the cells from the analysis of PIV. The velocity induced by the vorticity field is given by Biot-Savart law. The magnitude of the velocity induced by the fluid element in cell i on a fluid element in cell j is given by

$$u_{i \to j} = \frac{|\gamma_i|}{2\pi |x_i - x_j|} \qquad (6.1)$$

where $\gamma_i = \omega(x_i)\Delta x \Delta y$ is the circulation of the fluid element in cell i with Δx and Δy as the length and width of the cell. The sum of the induced velocities from all the fluid elements gives the advection velocity of the fluid element in cell j.

In order to quantify the vortical interactions occurring in the turbulent combustor, we perform a weighted time-varying spatial network analysis. For a given dynamical state of combustor operation, we construct networks at each instant of time. The fluid elements in the Cartesian cells are the nodes of the network, while the links of the network represent the vortical interactions among the fluid elements. The weight of the link quantifies the strength of these interactions. Here, we consider the mean of the induced velocities between two fluid elements i and j as the weight of the link between

101

them. Since we are considering only the magnitude of the induced velocities, the resultant network is undirected. The details of network connectivity are mathematically given in the form of a square matrix called the adjacency matrix. An element of the adjacency matrix (A_{ij}) corresponds to the weight of the link between the nodes i and j. Hence, the adjacency matrix is given as follows:

$$A_{ij} = \begin{cases} \dfrac{1}{2}\left(u_{i \to j} + u_{j \to i}\right) & if \; i \neq j \\ 0 & if \; i = j \end{cases} \qquad (6.2)$$

The diagonal elements of the adjacency matrix are zeros as the velocity induced by a fluid element upon itself is zero. Since each fluid element is connected to all other elements, the vorticity network is a complete graph. In the next section, we shall characterize the vorticity interactions during the different dynamical states of combustor operation.

Recently, Murayama *et al.* (2018) used the aforementioned approach to characterize the vorticity interaction only during thermoacoustic instability in a turbulent swirl stabilized combustor. In the present study, we characterize the vorticity interaction during the intermittency route to thermoacoustic instability in a bluff body stabilized turbulent combustor.

6.2 TRANSITION FROM COMBUSTION NOISE TO THERMOACOUSTIC INSTABILITY: SCALE-FREE TO AN OSCILLATION BETWEEN RANDOM AND SCALE-FREE

We construct time-varying weighted vorticity networks during combustion noise, an aperiodic epoch of intermittency, an periodic epoch of intermittency and during thermoacoustic instability. We now shall examine these networks one by one.

6.2.1 Vorticity Interaction during Combustion Noise

Combustion noise is characterized by low amplitude aperiodic oscillations. During combustion noise, we observe small discrete vortices in the outer shear layer. Also, small vortices are shed from the tip of the bluff body, as discussed in Chapter 4. Figure 6.1 shows (b) the vorticity field (ω) and the velocity vectors obtained from the analysis of PIV, (c) the spatial distribution of the node strength (s) of the vorticity network and (d) the node strength distribution in log-log scale at some arbitrary points (A-E) marked on (a) the time series of the acoustic pressure fluctuations during combustion noise. The colour bars in the bottom left and bottom right side of the figure show the range of ω and s, respectively. The positive values of ω correspond to anti-clockwise vorticity and the negative values correspond to clockwise vorticity, respectively. High values of positive and negative vorticity correspond to the small discrete vortices present along the outer and inner shear layers, respectively. Comparing the spatial distribution of ω (figure 6.1b) with that of s (figure 6.1c), we observe that regions of ω coincide with regions of s. Since we are considering only the magnitude of the induced velocity for network construction, s is positive throughout the flow field. Maximum value of s corresponds to the vortices being shed from the tip of the bluff body.

The power law exponent of the node strength distribution (figure 6.1d) suggests a scale-free structure for the vorticity network ($2 < \gamma < 3$, Barabasi 2016). This implies that there are a large number of vortices with weak interaction strength, i.e., they induce low velocities. However, there are a few vortices with very high interaction strength, i.e., these vortices induce high velocities. Such vortices are called the 'hubs' of the network. The vortices that are shed from the tip of the bluff body (seen as red in figure 6.1c) are the primary hubs of the network. They are strong enough, compared to other vortices,
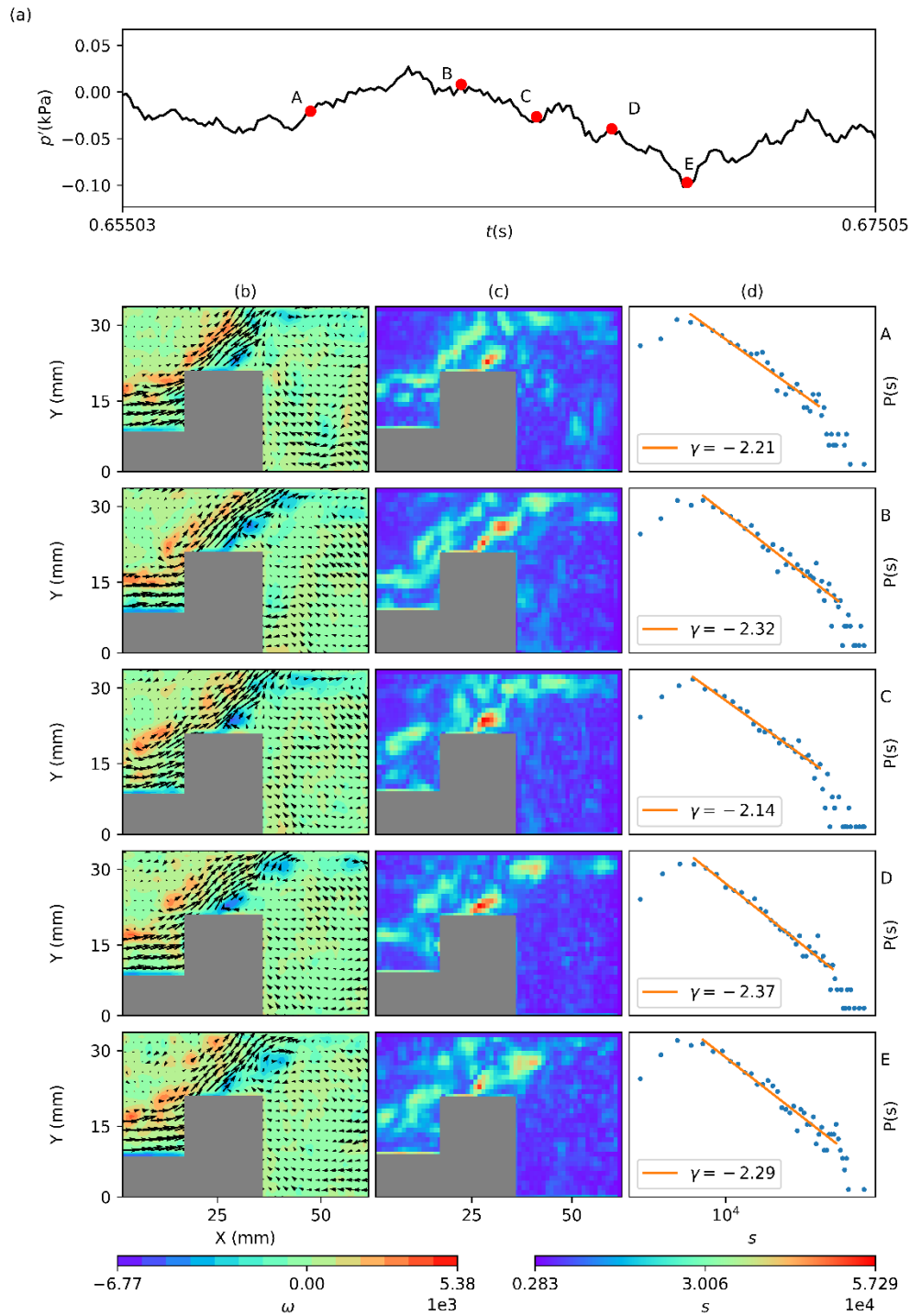
Figure 6.1: The spatial distribution of (c) the node strength (s) of the vorticity network at the corresponding time instants (A-E) marked on the (a) time series of fluctuating pressure during combustion noise. The corresponding velocity and vorticity field is shown in (b). Regions with high values of node strength coincides with regions of high vorticity at the tip of the bluff body. The power law exponent of the node strength distribution (d) implies that the vorticity interaction network during combustion noise is scale free.

104

to influence fluid elements at far away locations. The vortices present in the outer shear layer (seen as green in figure 6.1c) are the secondary hubs of the network. They are not as dominant as the primary hubs, in the sense, these moderately strong vortices induce low velocities over long distances as compared to the strong vortices. There are large number of smaller, weaker eddies (represented by blue in figure 6.1c), which have influence only in the local vicinity. Thus, we can say that the vortices shed from the tip of the bluff body play a vital role in controlling the spatiotemporal dynamics of the flow field during combustion noise. The coefficient of determinism for the curve fitting performed in all the cases reported here is $R^2 > 0.90$, as followed by Murayama *et al.* (2018).

6.2.2 Vorticity Interaction during Intermittency

Intermittency is characterized by bursts of seemingly periodic oscillations embedded amidst low amplitude aperiodic oscillations in a random manner. Here, we examine the vorticity interaction during an aperiodic epoch and a periodic epoch of acoustic pressure oscillations, respectively. Firstly, we examine the vorticity interaction during the aperiodic epoch of intermittency (figure 6.2a). We observe small discrete vortices along the outer shear layer downstream of the dump plane as well as from the bluff body tip as observed in the case of combustion noise (figure 6.2b). Comparing the colour bars of figure 6.1 and 6.2, we notice that the magnitudes of ω and s are of the same order as that during combustion noise. Consequently, the vorticity interaction is characterized by weighted scale-free networks (figure 6.2d, $2 < \gamma < 3$). Here also, the primary hubs of the network are the vortices shed from the tip of the bluff body. However, at certain time instances (figure 6.2c, at time instants D and E), we see primary hubs in the outer shear layer a well. This implies that these vortices induce velocities over long distances
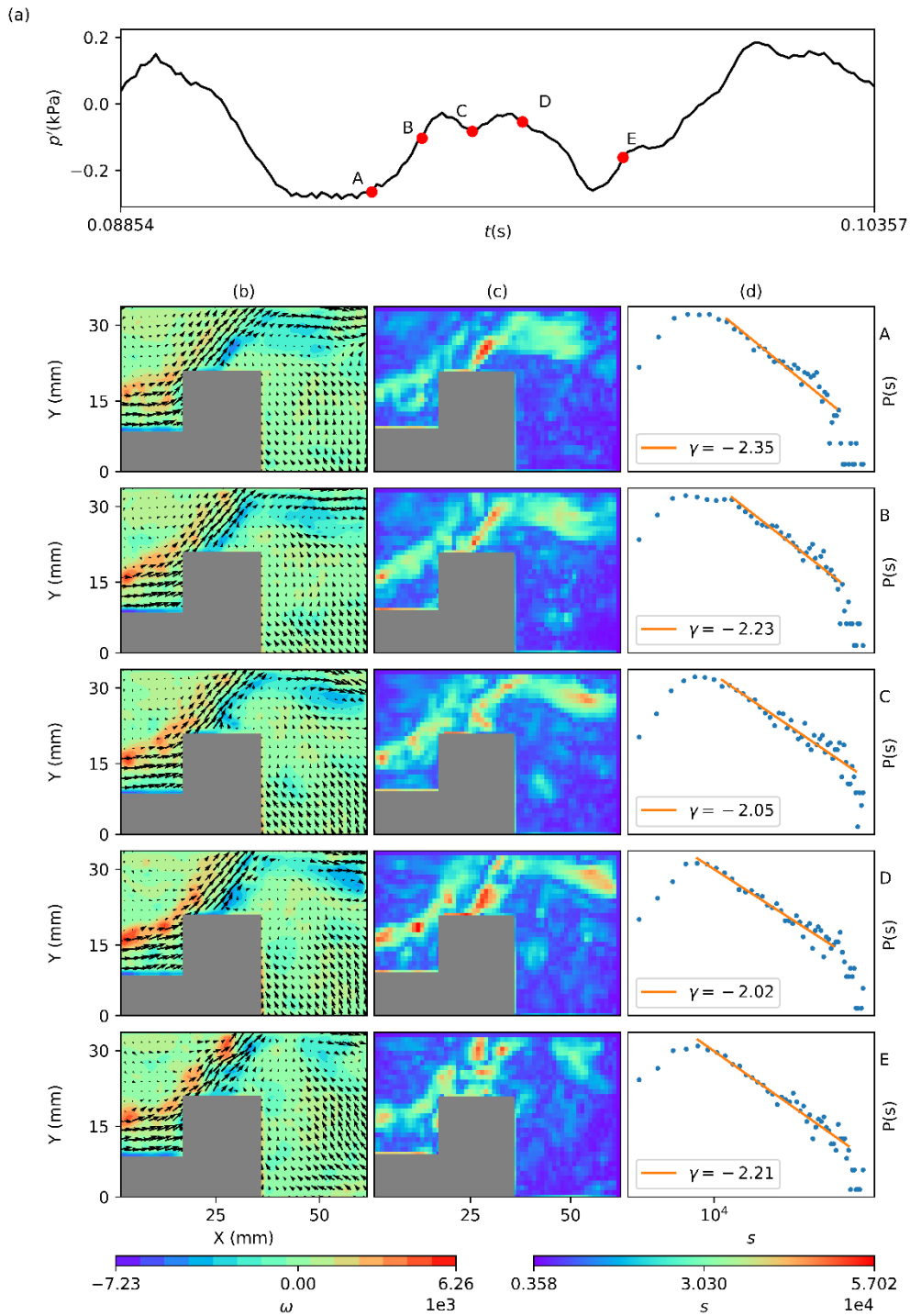
Figure 6.2. The spatial distribution of (c) the node strength (s) of the vorticity network at the corresponding time instants (A-E) marked on (a) the time series of acoustic pressure during an aperiodic epoch of intermittency. The velocity vectors and the vorticity field corresponding to the points (A-E) is shown in (b). The magnitude of the vorticity field and the node strength is comparable with that of combustion noise. The power law exponents (d) show that the vorticity interaction during the aperiodic epoch of intermittency is scale-free as in the case of combustion noise.

106
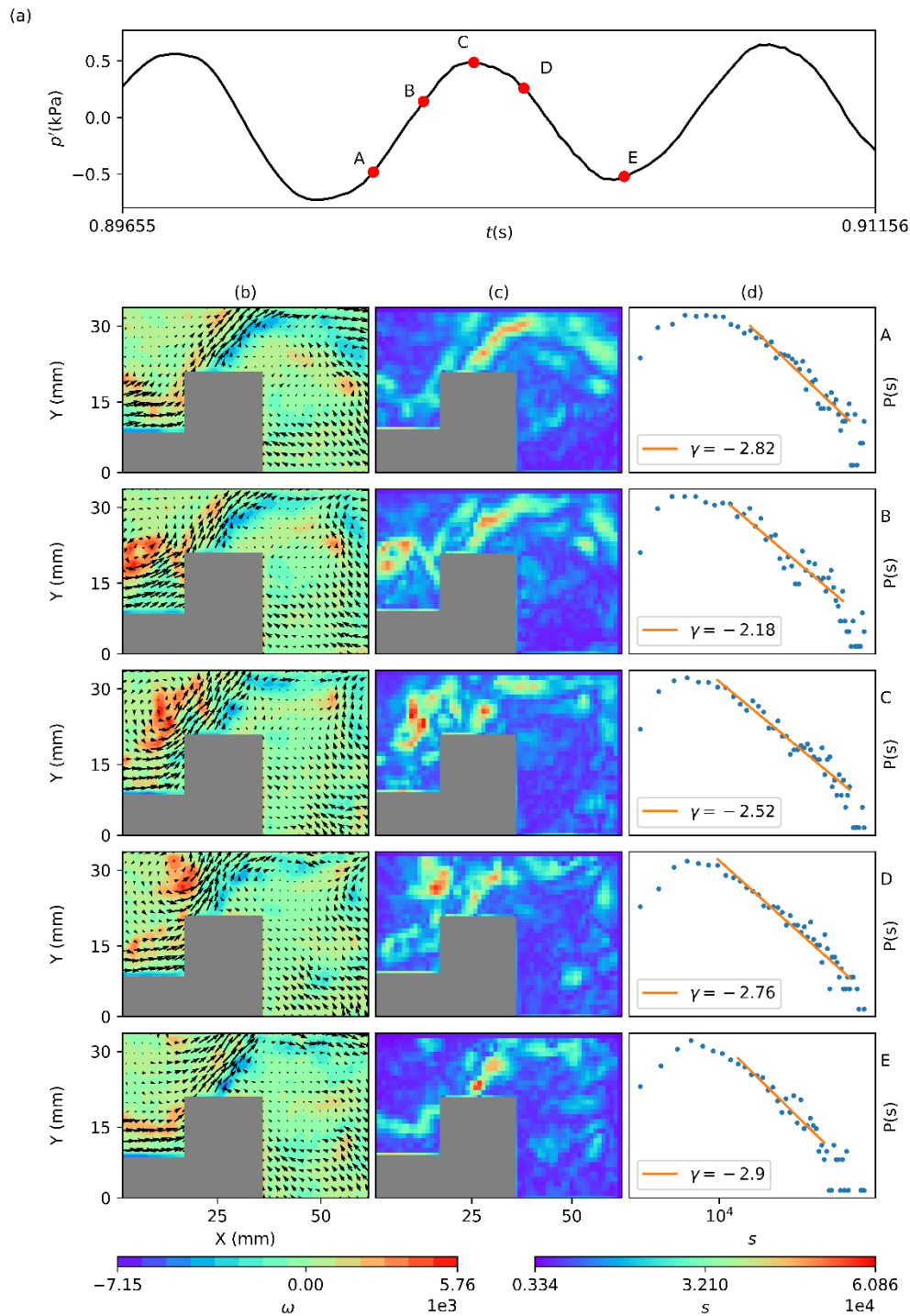
Figure 6.3. Spatial distribution of (c) the node strength (s) at the corresponding time instants (A-E) marked on (a) the time series of fluctuating pressure during an acoustic cycle of the periodic epoch of intermittency. The velocity vectors and the vorticity field shows the formation of coherent structures downstream of the dump plane (b, B to D). Regions with very high node strength coincides mainly with regions of high vorticity in these coherent structures. The power law exponents (d) suggest that the vorticity network during a high amplitude periodic burst is scale-free.

107

and hence control the spatiotemporal dynamics during the aperiodic epoch of intermittency.

Next, we examine the periodic epoch of intermittency (figure 6.3a). During this regime, we observe the formation of coherent structures downstream of the dump plane (figure 6.3b, at time instants B, C and D). It has to be noted that the magnitudes of ω and s are of the same order as that during combustion noise. The node strength distributions (figure 6.3 d) display scale-free behaviour ($2 < \gamma < 3$). This implies that the coherent structure behaves as the hub of the network (figure 6.3c at time instants B, C and D) and hence has strong influences over long distances. This scale-free behaviour is consistently observed during the high amplitude bursts. Hence, the vorticity interactions during both the aperiodic and periodic epochs of intermittency have weighted scale-free behaviour. Even though the network topologies are the same, the hubs of the vorticity networks during the two epochs are different. If it is the small vortices present in the outer and inner shear layer that control the spatiotemporal dynamics during the aperiodic epoch of intermittency, it is the coherent structures that are formed downstream of the dump plane, which control the spatiotemporal dynamics during the periodic epoch of intermittency.

6.2.3   Vorticity Interaction during Thermoacoustic Instability

Figure 6.4 shows the (b) flow field, (c) the spatial distribution of the node strength (s) and (d) the node strength distribution with the power law exponents at (a) five different time instants of an acoustic cycle during thermoacoustic instability. During thermoacoustic instability we observe periodic formation of a large coherent structure downstream of the dump plane. However, the strength and the size of these coherent

structures are higher than that observed during intermittency (George *et al.* 2018). This is evident from the comparison of the magnitude of ω and s of both the cases (figure 6.3 (b) with 6.4 (b) and figure 6.3 (c) with figure 6.4 (c)). A large vortex is also shed at almost the same frequency from the tip of the bluff body (figure 6.4b, at time instants C to D). The frequency of formation of the large coherent structure as well as the shedding of the large vortex from the bluff body tip equals the acoustic frequency during thermoacoustic instability. The magnitudes of ω and s are one order of magnitude higher than that during combustion noise.

The coherent structure forms near the local minima (at time instant *A*) of the acoustic cycle and convects towards the top combustor wall (at time instants *B* and *C*). At time instant *A*, we observe a portion of the coherent structure formed downstream of the dump plane (figure 6.4b). This is due to the fact that the field of view used for the analysis of PIV, in the current study, is slightly away from the dump plane. A power law characterizes the node strength distribution with an exponent $\gamma > 3$ (figure 6.4d, A). Such a node strength distribution is a signature of random networks (Barabasi 2016). It would be interesting to perform the current study in the region just downstream of the dump plane to capture the formation of coherent structure better.

At time instant *B*, the coherent structure convects towards the top wall of the combustor (figure 6.4). The node strength distribution (figure 6.4d, B) suggests that the vorticity network is scale-free with the coherent structure acting as the network hub. Upon impingement at the top combustor wall (at time instant *C*), the coherent structure breaks down, giving rise to a spike in the heat release rate oscillation. At the same time, a

Figure 6.4: The spatial distribution of (c) the node strength (s) of the vorticity network at different time instants (A-E) of an acoustic cycle (a) during thermoacoustic instability. The velocity vectors and the vorticity field corresponding to the points is shown in (b). The magnitude of the vorticity field and the node strength is one order of magnitude higher than that during combustion noise. Regions with high node strength corresponds to regions with high vorticity in the coherent structure (A and B) as well as in the large vortex shed from the tip of the bluff body (C and D). The power law exponents (d) suggest an oscillation between random and scale-free networks during thermoacoustic oscillations.

vortex begins to form from the tip of the bluff body. The vorticity network is scale-free at this time instant as well (figure 6.4d, C). However, at this time, it is the vortex at the tip of the bluff body, which acts as the network hub. At time instant *D*, the vortex formed at the tip of the bluff body grows in size and strength and begins to convect downstream. Even though the power law exponent is slightly greater than 3 (figure 6.4d, D), we can consider the network to behave as scale-free. At time instant E, the big vortex convects further downstream of the bluff body. But it still remains as the hub of the network, as seen from the node strength distribution (figure 6.4, E). Thus, we observe that the topology of the vorticity network periodically oscillates between random and scale-free behaviour during thermoacoustic oscillations.

Recently, Murayama *et al.* (2018) showed that the vorticity interaction during thermoacoustic instability in a turbulent swirl stabilized combustor displays a scale-free network topology. They reported that the lifetime of this scale-free topology decays with a power law exponent of -2.1. However, the authors did not characterize the vorticity interaction during combustion noise and intermittency. The current study sheds light on the topology of vorticity interaction during the intermittency route to thermoacoustic instability.

6.3   CONCLUSIONS

In this chapter, we characterized the vorticity interaction occurring in the turbulent reactive flow field as the thermoacoustic system in the turbulent combustor transitions from a state of combustion noise to thermoacoustic instability via intermittency. We constructed weighted time-varying spatial turbulent networks based on Biot-Savart law to quantify the vortical interactions during the different regimes of combustor

111

operation. We observe that the vorticity interaction during combustion noise is characterized by scale-free networks. Similar to combustion noise, the vorticity interaction during the aperiodic and periodic epochs of intermittency is also scale-free. However, during thermoacoustic instability, the network topology oscillates between random and scale-free behaviour in one acoustic cycle. As a future study, it would be interesting to relate the behaviour of the vorticity networks to the flame dynamics during the different states of combustor operation.

CHAPTER 7

ON THE EMERGENCE OF CRITICAL REGIONS AT THE ONSET OF THERMOACOUSTIC INSTABILITY

Network centrality measures such as degree, betweenness and closeness centralities are used to deduce the importance of a node in a network. Higher the value of these centrality measures, greater the importance of the node. These critical nodes play a vital role in the functioning of the network (Newman 2010, Boccaletti *et al.* 2006). In this chapter, we construct spatial networks based on the correlation between the pairs of time series of velocity obtained from the analysis of particle image velocimetry (PIV). To obtain a good spatial resolution of the velocity field, we perform PIV at two different regions in the flow field. Firstly, we examine the region around the bluff body – both the upstream and downstream regions of the bluff body. In this region of interest, we can capture the convection of the coherent structure towards the top wall of the combustion chamber as well as the shedding of a large vortex from the tip of the bluff body during thermoacoustic instability. It is the same region of interest used for vorticity network construction in Chapters 5 and 6. Secondly, we examine the region extending from the dump plane to the bluff body. In this region, we capture the formation of the coherent structure downstream of the dump plane and its convection towards the top wall of the combustor during thermoacoustic instability. We then

compute the network centrality measures and identify the critical regions, which control

the spatiotemporal dynamics during different dynamical states of combustor operation.

7.1 CRITICAL REGIONS IN THE FLOW FIELD AROUND THE BLUFF BODY

7.1.1 Network Construction

Let us first focus on the region around the bluff body. We obtain the instantaneous

velocity field from the analysis of PIV. We use Pearson's correlation to capture the

statistical relationship between the pairs of time series of velocity. Here, we consider

the magnitude of the 2-D velocity obtained from the analysis of PIV to compute the

Pearson's correlation coefficient. The interrogation windows used in the analysis of

PIV are the nodes of the network and two nodes are connected if the value of Pearson's

correlation coefficient is above a threshold. Pearson's correlation coefficient is defined

as,

$$R_p = \frac{\sum_{i=1}^n (x_i - \bar{x})(y_i - \bar{y})}{\sqrt{\sum_{i=1}^n (x_i - \bar{x})^2} \sqrt{\sum_{i=1}^n (y_i - \bar{y})^2}} \tag{7.1}$$

where x_i is the magnitude of velocity at a grid point at the time instant i and y_i is the

magnitude of velocity at a different grid point at the same instant of time. The arithmetic

means of both the time series are represented by $\bar{x}$ and $\bar{y}$ respectively. In the present

study, we choose 0.25 as the threshold Pearson's correlation coefficient. At 0.25, the

variation in the link density of the networks across combustion noise, intermittency and

thermoacoustic instability is maximum (see figure A3 in Appendix). Maximum

variation in link density ensures maximum variation in the topology of the correlation

networks. Thus, we would be able to discern the critical regions in a better way across

114

the different dynamical states of combustor operation. The elements of the adjacency

matrix (A_{ij}) for the above network construction is given by

$$A_{ij} = \begin{cases} 1, & R_p \geq 0.25 \\ 0, & R_p < 0.25 \end{cases} \tag{7.2}$$

where i and j refer to the nodes of the network. The adjacency matrix thus obtained is

a symmetric matrix since the correlation network is undirected (i.e., i connected to j

implies j connected to i). We then compute the network properties such as the degree,

the local clustering coefficient, the betweenness centrality and the closeness centrality.

7.1.2   Topology of the Spatial Correlation Network
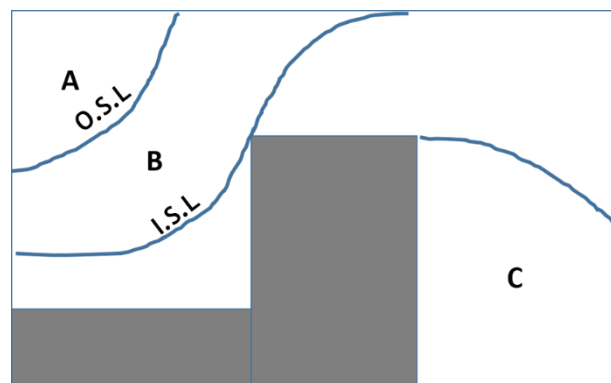
Figure 7.2: The schematic of the flow field divided into three distinct regions. 'A' represents the wake of the dump plane. The region between the outer shear layer (O.S.L) and inner shear layer (I.S.L) is marked as region 'B' and the bluff body wake is indicated as 'C'. This distinction helps one for the better description of the distribution of network measures in the flow field.

For ease of describing the distribution of complex network measures during the three

dynamical states of combustion noise, intermittency and thermoacoustic instability, we

divide the flow field into three regions, namely A-the wake of the dump plane, B-the

region between the outer shear layer and inner shear layer, called as 'shear zone' and C-the bluff body wake; as shown in figure 7.1.

The degree of a node (i.e., the grid point in the flow field) gives the number of neighbours of that particular node (grid point) in the spatial network. In the case of the spatial network constructed using Pearson correlation, a high degree implies that the correlation between the velocity fluctuations at the given grid point and that of a large number of other grid points is above the threshold. The spatial distribution of degree during the three dynamical regimes of the turbulent combustor operation is shown in figure 7.2a-c. During combustion noise, region C has the highest degree. During combustion noise, the flow recirculates in the wake of the bluff body. This coherent motion of the fluid particles in the wake of the bluff body during combustion noise gives the bluff body wake a very high degree distribution (figure 7.2a). During intermittency, the degree of region B increases when compared to that during combustion noise (figure 7.2b). During thermoacoustic instability, region B has the highest degree whereas, the degree of region C reduces (figure 7.2c). Region A has a medium degree with a region of very low degree located at the top left corner. As the turbulent combustor transitions from combustion noise to thermoacoustic instability, the degree of the bluff body wake reduces and that of the shear zone increases.

Next, the spatial distribution of local clustering coefficient during the three dynamical regimes of the turbulent combustor operation is shown in figure 7.2d-f. The local clustering coefficient of a grid point gives the idea of connectivity among the neighbours of that grid point. High values of local clustering coefficient (close to 1.0) for a grid point implies that the neighbours of the grid point are highly interconnected.
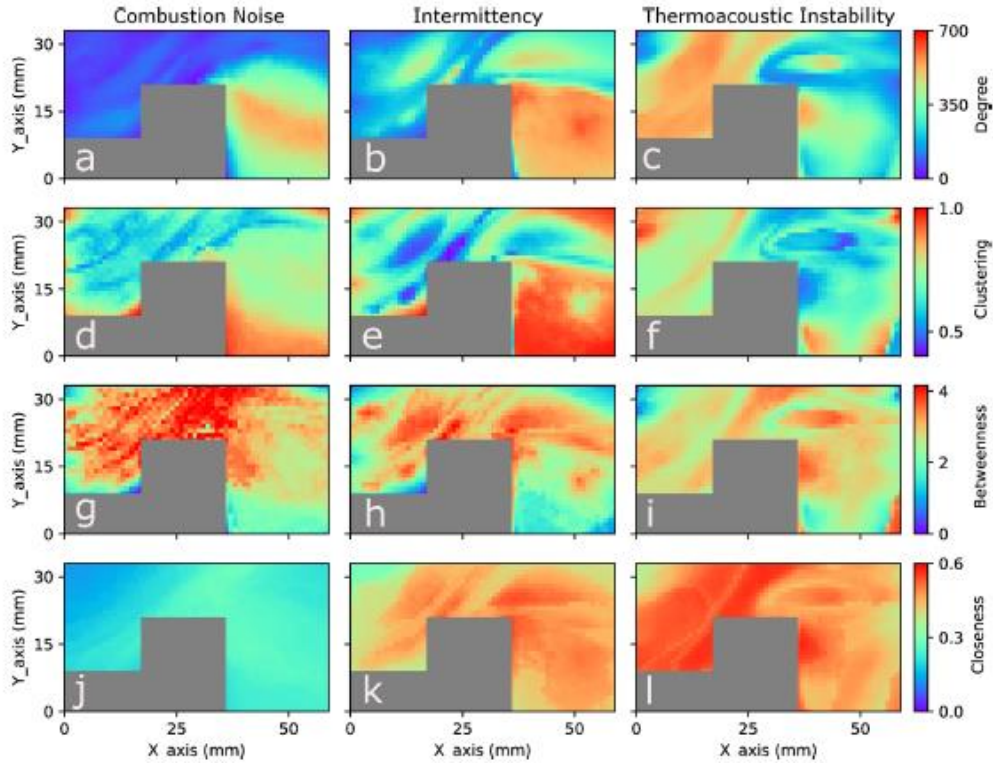
Figure 7.2: Spatial distribution of degree, local clustering coefficient, betweenness centrality and closeness centrality during combustion noise, intermittency and thermoacoustic instability. During combustion noise, the wake of the bluff body emerges as the critical region. At the onset of thermoacoustic instability, the wake of the bluff body loses its importance and the shear zone emerges as the critical region.

From a flow perspective, this implies that the correlation between the velocity fluctuations of the neighbours of a given grid point is above the threshold. If a region is having high degree and high clustering coefficient, then, we can say that the given region is spatially coherent regarding velocity fluctuations. This implies that the velocity fluctuations vary similarly amongst the nodes of that particular region. During combustion noise, region C has some patches of high local clustering coefficient. Both regions A and B have low and medium values of local clustering coefficient (figure 7.2d). During intermittency, most of the bluff body wake has very high local clustering coefficient (figure 7.2e). High values of degree and local clustering coefficient for the bluff body wake, during intermittency, implies that the nodes of the region are having

a large number of neighbours that are highly interconnected to each other. During thermoacoustic instability (figure 7.2f), region B along with some areas of region C have the lowest local clustering coefficient. Very high value of local clustering coefficient along with very low degree for the corner of dump plane wake, during thermoacoustic instability, suggests that even though this region of very low average velocity and very high average vorticity has very few neighbours, these neighbours are highly interconnected to each other. Very high value of degree and medium value of local clustering coefficient for the shear zone, during thermoacoustic instability, suggests that the nodes in the shear zone have a large number of neighbours which are moderately interconnected among themselves.

Betweenness centrality of a grid point gives the fraction of all the shortest paths for every pair of grid points in the flow field passing through the given grid point. High values of betweenness centrality for a grid point suggests that the grid point lies in between two regions of a network and a large number of shortest paths passes through that particular grid point. High values of betweenness centrality highlight the central pathways of information travel in a network if it is assumed that information propagates through shortest paths in a network. In the present analysis, regions of high betweenness centrality indicate those regions that connect different parts of the flow that are otherwise uncorrelated to each other. Considering this, regions of high betweenness centrality could be responsible for the increased correlation in the reactive flow field during an ordered behaviour seen at the onset of thermoacoustic instability.

In figure 7.2g-i, we plot the spatial distribution of the betweenness centrality, $\log_{10}(b_i + 1)$, where b_i is the betweenness centrality of a node (see equation 2.3 in Chapter 2). During combustion noise, regions of high betweenness centrality are spread

across the flow field (figure 7.2g). During intermittency, the betweenness centrality is high along the shear zone (region B) as well as in the part of the flow neighbouring the shear zone (figure 7.2h). During thermoacoustic instability, region B, along with some locations in region C, show a very high value of betweenness centrality (figure 7.2i). Very high values of degree and betweenness centrality coupled with very low value of local clustering coefficient for the shear zone (region B), during thermoacoustic instability, implies that the grid points in the shear layer have a large number of neighbours, spread across the entire flow field, with very low interconnections among them. We can thus hypothesize that the shear zone acts as a bridge, through which the flow fluctuations are transported, between the dump plane wake and the bluff body wake during thermoacoustic instability.

Closeness centrality of a grid point measures the closeness of that particular grid point to all other grid points in the flow field. It is proportional to the reciprocal of the sum of shortest paths between a grid point and all other grid points in the flow field. Any perturbation given to a grid point with the highest value of closeness centrality travels in minimum time to all other grid points of the flow field. We can observe that region C has the highest closeness centrality during combustion noise (figure 7.2j). Thus, any perturbation given to any grid points in the bluff body wake will alter the dynamics of combustion noise. With the very high value of degree and closeness, we can infer that the bluff body wake is the most critical region during combustion noise. During intermittency, the closeness centrality of the bluff body wake is similar to that of the shear zone. During thermoacoustic instability, closeness centrality of the bluff body wake is lower than that of the shear zone (figure 7.2l). The closeness centrality of the shear zone, as the turbulent combustor transitions from combustion noise to thermoacoustic instability, reaches the maximum value. The shear zone, with very high

119

values of degree and closeness centrality, emerges as the most critical region during thermoacoustic instability. We can thus hypothesize that any control measure directed towards mitigation of thermoacoustic instability will be most effective when applied to the shear zone, i.e., region B.

7.1.3 Emergence of Critical Regions at the Onset of Thermoacoustic Instability

In the past, many studies have investigated the flow pattern in the wake of the flame holder during combustion noise and thermoacoustic instability (Rogers and Marble 1956; Smith and Zukoski 1985; Poinsot *et al.* 1987, Chakravarthy *et al.* 2007). During combustion noise (stable combustion), the incoming reactant mixture separates from the surface of the flame holder and mixes with the hot products recirculating in the wake region downstream of the flame holder in a thin turbulent shear zone. This process is the key to maintaining continuous ignition and establishing a stable propagating flame. During thermoacoustic instability, the shear layer formed downstream of the flame holder is periodically perturbed by large coherent structures, which dictates the dynamics of the reactive flow field. Hence, the recirculating wake downstream of the flame holder, which is critical for the stabilisation of the turbulent flame during combustion noise (stable combustion), loses its significance in determining the dynamics of the reactive flow field observed during thermoacoustic instability.

The importance of the bluff body (flame holder) wake during combustion noise is very well captured by the spatial network analysis performed in the current study. It is reflected in the high values of degree and closeness centrality, two complex network measures that highlight the importance of nodes in a network. The reflection of this finding in the distribution of centrality measures across the flow field corroborates our

methodology of spatial network construction. As the turbulent combustor transitions to thermoacoustic instability, the bluff body wake (region C) loses its importance and the region between the outer and inner shear layer (region B) emerges as the most critical region in the flow field. During intermittency, even though the bluff body wake (region C) still has high values of degree and closeness centrality, the values of these centrality measures increase for the shear zone (region B) when compared to that during combustion noise. Hence, the spatial network analysis can capture the transition of the turbulent combustor from combustion noise to thermoacoustic instability via intermittency effectively.

The identification of the most critical regions at the onset of thermoacoustic instability is of paramount importance as it can be used for devising efficient control strategies to mitigate thermoacoustic instability. Very recent studies have investigated the efficiency of control strategies based on the identification of critical regions obtained by using network centrality measures. Russo, Russo and Siettos (2016) has applied spatial network analysis for the spatial distribution of fire breaks in heterogeneous forest landscapes for the control of wildland fires. The group of network nodes (small land patches) that favour fire propagation is identified by exploiting network centrality statistics such as betweenness centrality and Bonacich centrality. The authors, through simulations, have shown that the proposed methodology based on complex network approach outperforms the conventional forest management practices. Taira *et al.* (2016) have shown that the two-dimensional turbulence network, obtained by characterizing vortical interactions, is resilient against random perturbations, but can be significantly influenced if the forcing is targeted towards the large vortical structures which are identified as network hubs. This study highlights the advantage of using spatial network analysis for modifying the collective dynamics of vortices in the turbulent flow field as

estimating and controlling every vortical structure in a turbulent flow is most likely improbable and impractical.

Analysis of networks constructed using Pearson's correlation suggests that for effectively mitigating thermoacoustic instability in the present combustor, the passive control strategies should be aimed at the region between the outer and inner shear layers which have high values of degree, betweenness and closeness centralities. One of the popular passive control strategies is to inject micro-jets into the flow field. Such perturbations spread locally in the flow field and affect the global behaviour of the flow field. In the next section, we will further analyse the flow field to identify the topology of connectivity introduced by the local correlations in the flow field. Thus, it is important to study the local connectivity patterns of the flow field to identify such critical regions. To that end, we construct spatial networks using the dot product of the time series of velocity as against Pearson's correlation. While Pearson's correlation captures the connectivity patterns due to both local and long-range correlations induced by large-scale flow structures, dot product captures mainly the local connectivity patterns.

7.1.4 Topology of the Network Constructed Using the Dot Product

In this section, we examine the spatial distribution of the network properties based on the dot product defined as,

$$R_s = \sum_{i=1}^{n} x_i y_i \tag{7.3}$$

where x_i and y_i mean the same as in equation 7.1.

Here, two nodes are connected if the dot product of the time series of magnitude of velocity is above a threshold. We choose the threshold such that the resultant network has a link density of 50%. Unlike in the case of the network construction using Pearson's correlation, here, we fix the link density of the networks at 50%. This implies that 50% of the total possible links are present in the network corresponding to the different dynamical regimes of combustor operation. Like the fixed threshold used in Pearson's correlation coefficient approach, the fixed link density approach also ensures that the topology of the network changes as the turbulent combustor transitions from one dynamical regime to another and helps us compare and contrast the spatiotemporal dynamics across the three regimes of combustor operation. Both these approaches of constructing spatial networks help discern different aspects of the flow field.

The degree distributions during the different dynamical regimes of combustor operation are shown in figures 7.3a-c. During combustion noise, the degree is very high along the region between the outer and inner shear layer (region B) which implies that the region is locally correlated to many other grid points in the flow field (figure 7.3a). This implies that the amplitude of the velocities in the region between the outer and inner shear layer and its neighbors are correlated. Very high values of degree and medium values of local clustering coefficient between the outer and inner shear layer implies that the grid points in this region are connected to many other grid points in the flow field and these grid points are moderately interconnected to each other. During intermittency, the region between the outer and inner shear layer continues to have a high degree (figure 7.3b). During thermoacoustic instability, the area of the region between the outer and inner shear layer with a very high degree increases (figure 7.3c). This suggests that a more substantial part of the flow field has velocity fluctuations of

similar amplitude possibly due to the periodic shedding of coherent structures during thermoacoustic instability.
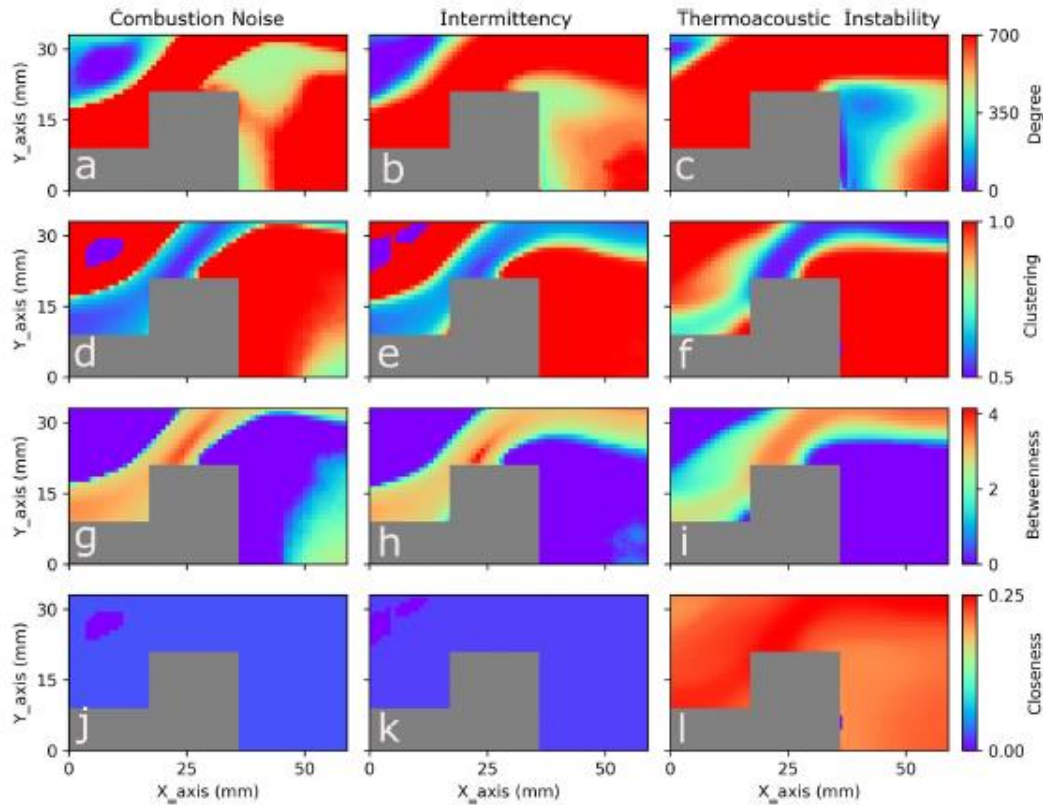
Figure 7.3: Spatial distribution of degree, local clustering coefficient, betweenness centrality and closeness centrality obtained by using dot product keeping the link density at 50%. During thermoacoustic instability, the region on top of the bluff body emerges as most the critical region.

A region with high degree and high local clustering coefficient implies that the given region is spatially coherent in velocity amplitude. During combustion noise, the local clustering coefficient is very low for a small region in the wake of the dump plane (region A) and very high downstream of the bluff body (region C) (figure 7.3d). The region between the outer and inner shear layer (region B) has medium values of local clustering coefficient. During intermittency, the medium values of local clustering

coefficient extend towards the wake of the bluff body (figure 7.3e). However, during thermoacoustic instability, the region between the outer and inner shear layer with medium values of local clustering coefficients shrinks (figure 7.3f). This implies that as the thermoacoustic system transitions from combustion noise to thermoacoustic instability, the number of grid points in the region between the outer and inner shear layer with moderately connected neighbours reduces.

The spatial distribution of the betweenness centrality ($\log_{10}(b_i + 1)$, where b_i is the betweenness centrality of a node) is shown in figure 7.3g-i. During combustion noise, the betweenness centrality is very high in the region between the outer and inner shear layers (figure 7.3g). This implies that a large number of shortest paths pass through the grid points in this region. During intermittency, the region between the outer and inner shear layer has the highest betweenness centrality (figure 7.3h). However, during thermoacoustic instability, the very high value of betweenness centrality shrinks to the part of region B on top of the bluff body (figure 7.3i).

In the case of the spatial network constructed using the dot product, the closeness centrality is very low during both combustion noise and intermittency (figure 7.3j and 7.3k). However, during thermoacoustic instability, the closeness centrality is very high (figure 7.3l). Hence, as the turbulent combustor transitions from combustion noise to thermoacoustic instability, the closeness centrality of the entire flow field increases. Thus, at thermoacoustic instability, if we give any perturbation to any of the grid points in the flow field, it may affect the entire flow field in a very short period of time.

The findings from analysing the topology of network constructed using dot product suggest that during thermoacoustic instability, the significance of region B in

determining the flow dynamics increases. Further, we can observe that betweenness centrality is maximum in the part of region B located on top of the bluff body. This suggests that this part of the region B determines the dynamics during thermoacoustic instability.

From the perspective of reactive flow, this location is where the vortices formed downstream of the dump plane impinge and produce bursts of high heat release rate (Unni and Sujith 2017). These bursts of high heat release rate translate into maximum acoustic power production in that location and also makes this region the part of the flow that separates the region of acoustic power production from the rest of the flow (figure 7.3f and 7.3i). It is well known that the acoustic power production is enabled by the oscillatory behaviour of the heat release rate. Since the region on top of the bluff body is where bursts of oscillations of heat release rate happen, it is interesting that this region also emerges as the most critical region in determining the dynamics of the reactive flow field.

7.2   CRITICAL REGIONS DOWNSTREAM OF THE DUMP PLANE

Next, we examine the other region of interest, the region extending from the downstream of the dump plane to the bluff body. This region of interest, as shown in figure 7.4, captures the formation of the coherent structure and its convection till the top of the bluff body.

7.2.1 Network Construction

Similar to the previous approach, two nodes are connected, only if the value of the Pearson's correlation coefficient is above a threshold. As discussed in Section 7.1.1, the threshold is chosen such that the variation of the link density is maximum across combustion noise, intermittency and thermoacoustic instability. In the current region of interest, the threshold correlation coefficient is 0.1. To capture the strength of the correlation between the time series of velocity at two different locations, here, we perform weighted spatial network analysis. We assign the Pearson's correlation coefficient, if it is above the threshold, as the weight of the link between the nodes. In this manner, we construct a weighted correlation network for combustion nose, intermittency and thermoacoustic instability. To identify the critical regions in the flow field during the different dynamical states, we calculate various weighted network measures, namely the node strength, weighted local clustering coefficient and weighted closeness centrality.

Node strength (s) is the counterpart of the degree in weighted networks. Node strength is defined as the sum of the weights of all the links attached to the node. Since we take the strength of interaction between the nodes into account, s gives better insight compared to the degree, which only takes into consideration the connectivity of the nodes. A node having higher s implies that the links of the given node carry higher weights. In the present study, the weight of the link is the Pearson's correlation coefficient. Hence, regions of high node strength represent areas where the velocity fluctuations are highly correlated, above the threshold, to those at other regions of the flow field.

Local clustering coefficient takes into account the connectivity of the neighbours of a node. Weighted local clustering coefficient, however, takes into account the heterogeneity in the interaction strength of the neighbours of a node. It tells how strongly the neighbours of a node are connected. Weighted local clustering coefficient ($\widetilde{C_\iota}$) of a node i is given by,

$$\widetilde{C_\iota} = \frac{\sum_{j,k} w_{ij} w_{jk} w_{ki}}{\max(w) \sum_{j,k} w_{ij} w_{ki}} \tag{7.4}$$

where j, k are the neighbours of the node i (Holme *et al.* 2007). In the above equation, $\max(w)$ refers to the maximum weight of the network. A node i with high node strength and high weighted local clustering coefficient implies that the links emanating from i have large weights and the neighbours of node i are interconnected among themselves. In the present study, a region with high values of node strength and weighted local clustering coefficient implies that the time series of velocities at the nodes in the given region are highly correlated among themselves. Hence, the given region represents a spatially coherent velocity field.

Closeness centrality ($\widetilde{c_\iota}$) is used to identify the nodes, which could reach all other nodes quickly. In that sense, $\widetilde{c_\iota}$ can be considered as the inverse of farness, which, in turn, is the sum of distances to all other nodes. Weighted closeness centrality (*w.c.c*) of a node i is given by,

$$\widetilde{c_\iota} = \sum_{j=1, j \neq i}^{n} 2^{-d_w(i,j)} \tag{7.5}$$

where $d_w(i,j)$ is the least costly path between the nodes i and j. For weighted network analysis, the least costly path is considered the shortest path between two nodes. The sum of the minimum costs of the paths from a node to all other nodes is the measure of farness: the higher the sum, the more it costs a node to reach all other nodes. Hence, the

inverse of the sum gives the closeness of a node to all other nodes. Here, Pearson's correlation coefficient is the weight of the link. Perturbations travel faster via highly correlated paths. Hence, we consider the cost of a link as the inverse of the Pearson's correlation coefficient. Higher the values of Pearson's correlation coefficient for the paths from a node to all other nodes, lesser the costs and hence quicker the disturbances travel to all other nodes in the network.

7.2.2 Emergence of Critical Regions Downstream of Dump Plane

The spatial distribution of the weighted network properties such as (a) the node strength (S), (b) the weighted local clustering coefficient ($w.l.c.c$) and (c) the weighted closeness centrality ($w.c.c$) during combustion noise, intermittency and thermoacoustic instability is illustrated in figure 7.4. The grey rectangular region in the bottom right corner of the subplots is the bluff body. The colour bars gives the range of the respective network properties. Very high values of s are only seen during thermoacoustic instability, near the dump plane, above the bluff body shaft. The node strength is two orders of magnitude higher than that during combustion noise and intermittency. The region also has very high weighted clustering coefficient. Hence, we can say that the velocity fluctuations in the region are highly correlated among themselves. In other words, the region near the dump plane, above the bluff body shaft, is spatially coherent regarding the variation in velocity fluctuations. Also, we can see that the region as mentioned above has high values of weighted closeness centrality. Hence, any perturbation given to the region above the bluff body shaft will reach all other parts of the flow field quickly. Thus, from the high values of spatial distribution of node strength and weighted closeness centrality (the network centrality measures), we can conclude that as the thermoacoustic system in a turbulent combustor transitions from combustion noise to

thermoacoustic instability via intermittency, the region on top of the bluff body shaft, just downstream of the dump plane, emerges as the most critical region in the current region of interest. This region is part of the shear zone, which was identified as the critical region using spatial correlation network analysis around the bluff body (Section 7.1.2).
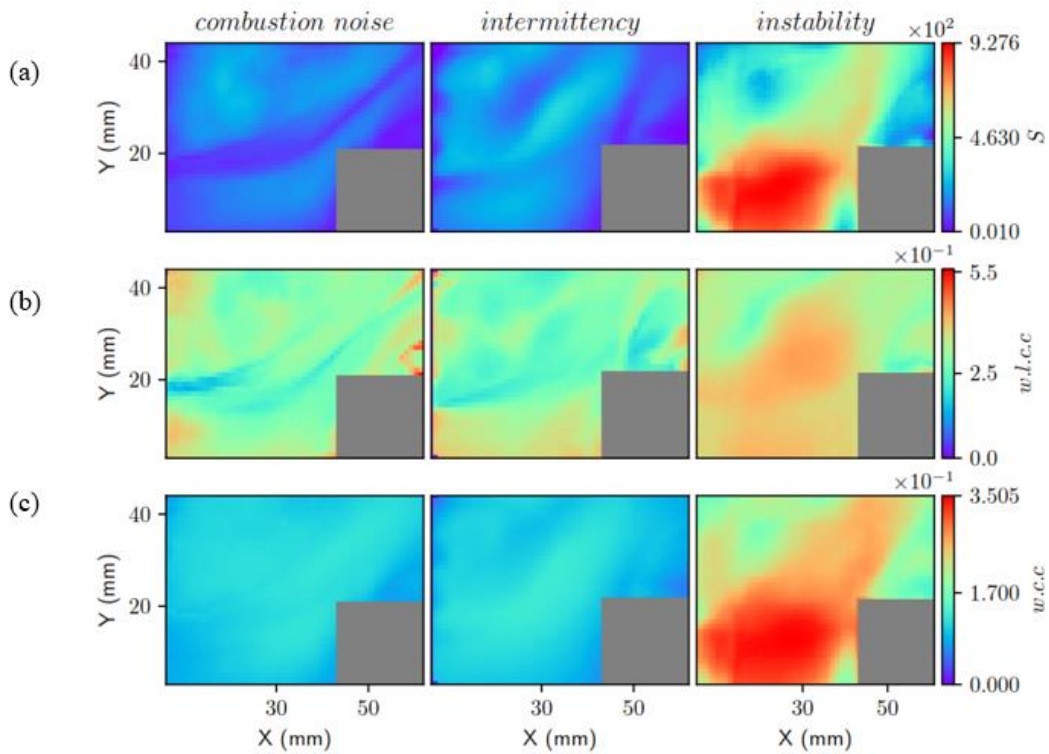
Figure 7.4: The spatial distribution of node strength, the weighted clustering coefficient and the weighted closeness centrality obtained by constructing weighted correlation networks. The region above the bluff body shaft with high values of s and $w.c.c$ emerges as the critical region at the onset of thermoacoustic instability.

7.3   CONCLUSIONS

In this chapter, we used spatial network analysis based on Pearson's correlation coefficient as well as the dot product between the time series of magnitude of velocity

to identify the critical regions that control the spatiotemporal dynamics of the turbulent reactive flow field during thermoacoustic instability. We identified two critical regions – (1) the region downstream of the dump plane, on top of the bluff body shaft and (2) the region on top of the bluff body. These two critical regions are part of the shear zone (see figure 7.1), the region between the outer and inner shear layer. While the former critical region captures the rollup of the shear layer leading to the formation of large scale coherent structures during thermoacoustic instability, the latter separates the region of maximum acoustic power production from the rest of the flow field. Hence, we can hypothesize that these two regions are the ideal locations for injection of micro-jets to control thermoacoustic instability. We shall test this hypothesis in the next chapter.

CHAPTER 8

A SMART AND EFFECTIVE WAY TO CONTROL THERMOACOUSTIC INSTABILITY

"Combustion instability was one of the biggest challenges of the Apollo programme. If we didn't come up with a solution, we weren't going to the moon", remarked Saverio 'Sonny' F. Morea, F1 engine project director[1]. His words reflect the significance of control of thermoacoustic instability. It is said that the engineers performed around 2000 full-scale tests, probably the most intensive and expensive programme ever devoted to solving the problem of thermoacoustic instability, to come up with a stable liquid rocket motor configuration (Oelefein and Yang 1993).

In this chapter, using complex networks, we propose a smart and effective approach to mitigate thermoacoustic instability. We have, in Chapter 7, identified two critical regions that control the spatiotemporal dynamics during thermoacoustic instability. We inject air micro-jets (also referred, here, as control air) at these critical regions and see if we could suppress thermoacoustic instability.

8.1   MODIFICATIONS IN THE EXPERIMENTAL SETUP

To inject air micro-jets, we modify the top and bottom plates of the combustion chamber. A schematic of the top plate with eight ports for micro-jet injection is shown

---

[1]The quote is taken from an image showing the F1 engine injector baffle, which is kept at the U.S. Space and Rocket Center, Huntsville, AL (http://heroicrelics.org/ussrc/engines-f-1-injector-baffle/dsc79618.jpg.html)

in figure 8.1. A similar plate is assembled at the bottom wall of the combustion chamber as well. We number the ports as 1, 2, …, 7 and 8 starting from the port situated near the dump plane. All the eight ports are equally spaced along the length of the combustor.
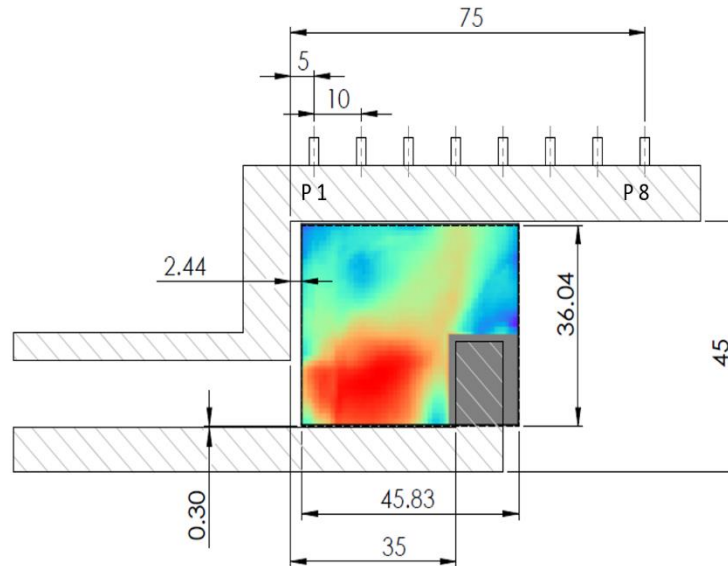
Figure 8.1: Top half of the combustion chamber showing the location of the eight micro-jet injection holes with respect to the spatial distribution of the node strength during thermoacoustic instability. The ports are numbered one (P1) to eight (P8) for reference. Ports 2 and 3 are above the critical region.

During the experiment, we inject the control air at the top as well as at the bottom. The air used for micro-jet injection is at the same pressure and temperature as the main air to the combustion chamber. The flow through these ports is choked (the pressure ratio is around 0.3). The top sectional view of the combustion chamber with the modified top plate along with the spatial distribution of the node strength during thermoacoustic instability is shown in figure 8.1. Ports 2 and 3 are above the critical region identified by the network analysis in section 7.2. Port 5 is above the bluff body, the other critical region identified by the network analysis in section 7.1.

8.2   RESULTS AND DISCUSSIONS
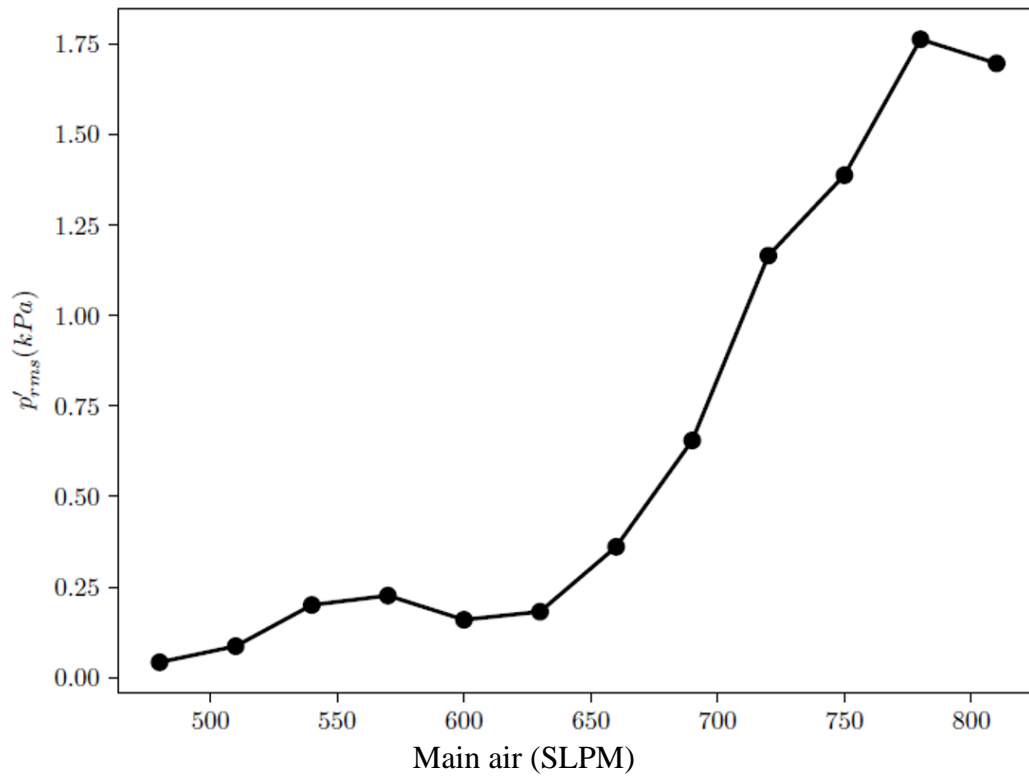
Figure 8.2: The variation of p'_{rms} with respect to the main air SLPM. We fix the fuel flow rate at 30 SLPM and increase the main air flow rate from 480 to 810 SLPM. The combustor dynamics transitions to thermoacoustic instability at 720 SLPM.

Firstly, we characterize the intermittency route to thermoacoustic instability in the present combustor. We fix the fuel flow rate constant at 30 SLPM and increase the air flow rate from 480 to 810 SLPM. When the main air flow rate is increased to 720 SLPM, the combustor dynamics transitions to thermoacoustic instability. Figure 8.2 shows the variation of p'_{rms} with the main air flow rate. We chose to pot the variation of p'_{rms} with main air flow rate to compare the effect of control air injection on thermoacoustic oscillations, which is shown in figure 8.3.
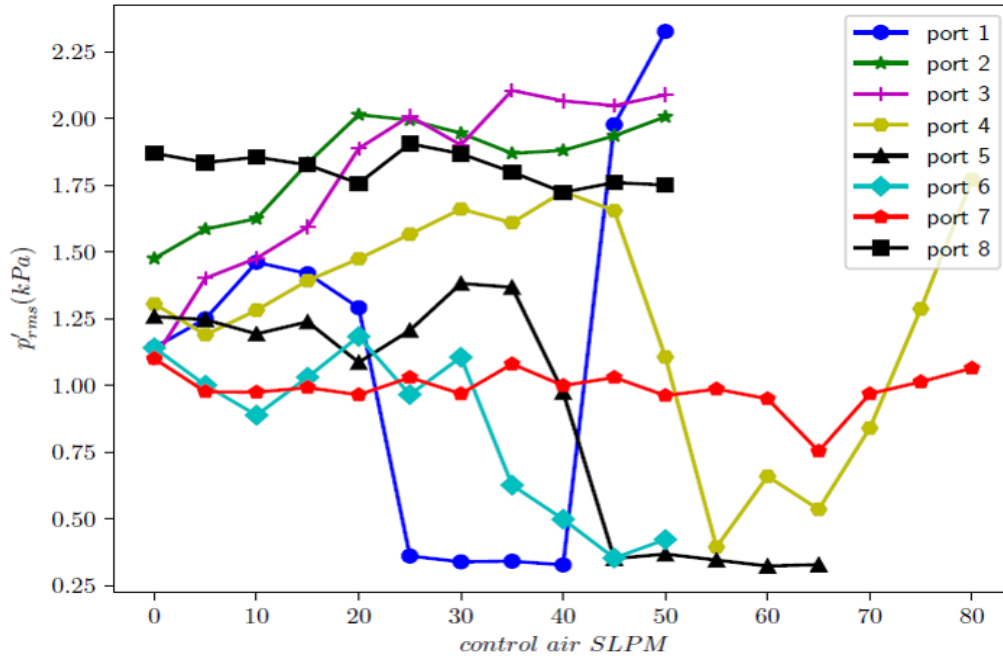
Figure 8.3: The variation of the rms of the acoustic pressure oscillations (p'_{rms}) with respect to the SLPM of the control air. The situation corresponding to 0 SLPM of control air corresponds to thermoacoustic oscillations.

Next, we see the effect of micro-jet injection through these ports. Firstly, we investigate the effect of micro-jet injection in all the eight ports one by one. We inject air at each port, both at the top and bottom of the combustion chamber, during thermoacoustic instability. We then measure p'_{rms} from the acquired time signal. Figure 8.3 illustrates the effect of micro-jet injection, at all the eight ports, on thermoacoustic oscillations. In the figure, a value of zero SLPM of the control air refers to the baseline case, i.e., thermoacoustic instability in the absence of any control air injection (main air flow rate is 720 SLPM). We observe suppression of thermoacoustic oscillations with micro-jet injection at ports 1(71%), 4 (57%), 5 (75%) and 6 (70%). The values in the parenthesis give the amount of reduction in p'_{rms}.

135

When we inject air at port 1, we are targeting the base of the shear layer. Hence, we prevent the formation of the coherent structure with injection at port 1, leading to the suppression of thermoacoustic instability. However, what causes the increase in p'_{rms} at higher flow rates of the control air is unknown. Enhancement of thermoacoustic oscillations occur with injection at ports 2 and 3. The reason for this behaviour is not known. It could be possible that the micro-jet oscillation (the situation here corresponds to jet in cross flow) could have coupled with thermoacoustic oscillation leading to an increase in the amplitude of acoustic pressure oscillation. We get suppression of thermoacoustic instability with micro-jet injection at ports 4, 5 and 6. These ports are located near the bluff body, where coherent structures impinge, leading to a spike in heat release rate. Hence, we can speculate that the coherent structures may be impinging against these jets. The fine-scale mixing that may happen because of this impingement against the jets may not be as efficient as the impingement against the combustor walls. Hence, the heat release rate would be lower and may be out of phase with the acoustic oscillations, leading to the suppression of thermoacoustic oscillations. However, the reason for the increase in p'_{rms} at higher flow rates is unknown. We observe neither suppression nor enhancement of thermoacoustic oscillations with micro-jet injection at ports 7 and 8, which are situated far downstream of the bluff body. A detailed investigation involving high-speed flame imaging along with PIV may be needed to know the physical mechanisms behind these observations. Nevertheless, it has to be noticed that we observe suppression of thermoacoustic oscillations in the case of micro-jet injection at port 5 even at higher flow rates of the control air (above 60 SLPM). When we consider these high values of control air flow rate along with the main air flow rate (720 SLPM), p'_{rms} of thermoacoustic oscillations is enhanced, as seen in figure 8.2. Thus, we can say that port 5, situated above the bluff body, is an ideal location for injection of micro-jet to suppress thermoacoustic instability.

We note that the critical region situated on top of the bluff body shaft is a large area encompassing the region below ports 2 and 3 (figure 8.1). Hence, we next examine the effect of simultaneous injection at ports 2 and 3. We first inject air only in port 3, in steps of 5 SLPM, up to 25 SLPM. Next, we keep the flow rate through port 3 fixed at 25 SLPM and start injecting air in port 2, in steps of 5 SLPM. The variation of p'_{rms} and $\dot{q}'_{rms}$ with the total air flow rate in ports 2 and 3 is shown in figure 8.4. As observed in figure 8.3, p'_{rms} increases when we inject control air at port 3 alone, up to 25 SLPM.
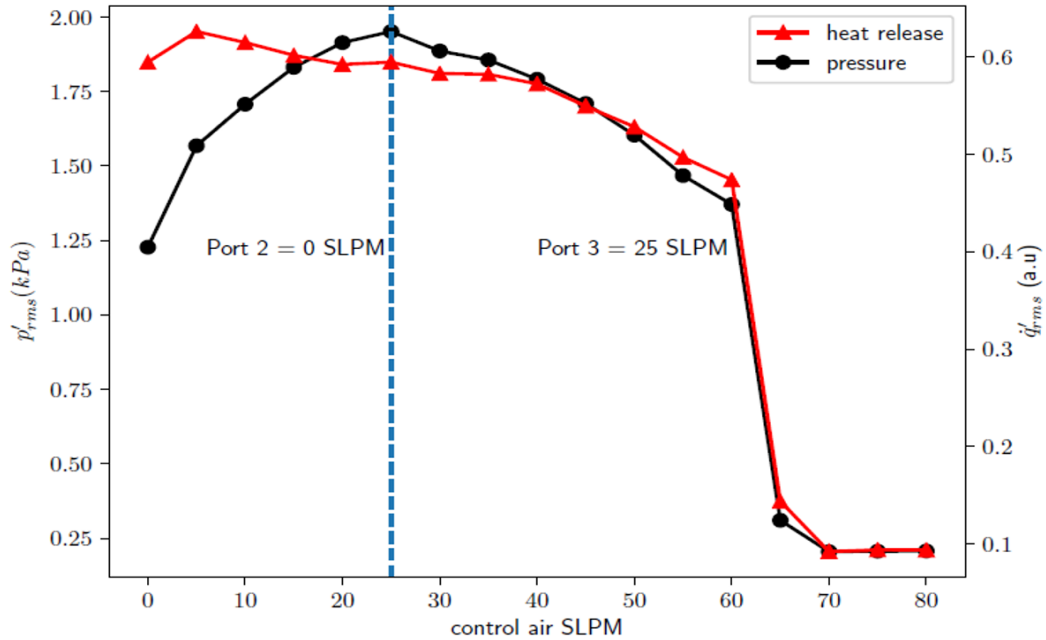
Figure 8.4: The variation of p'_{rms} and $\dot{q}'_{rms}$ with respect to the total air flow rate in ports 2 and 3. We observe around 85% reduction in p'_{rms} at 70 SLPM of control air (port 2: 45 SLPM and port 3: 25 SLPM).

Once we start to inject air at port 2, p'_{rms} begins to decrease. This implies that the spatiotemporal dynamics with simultaneous micro-jet injection at ports 2 and 3 is different from that with injection at port 3 alone. At 65 SLPM of the total control air,

we observe an abrupt reduction in p'_{rms}. We observe a reduction of around 85% in p'_{rms} at 70 SLPM.
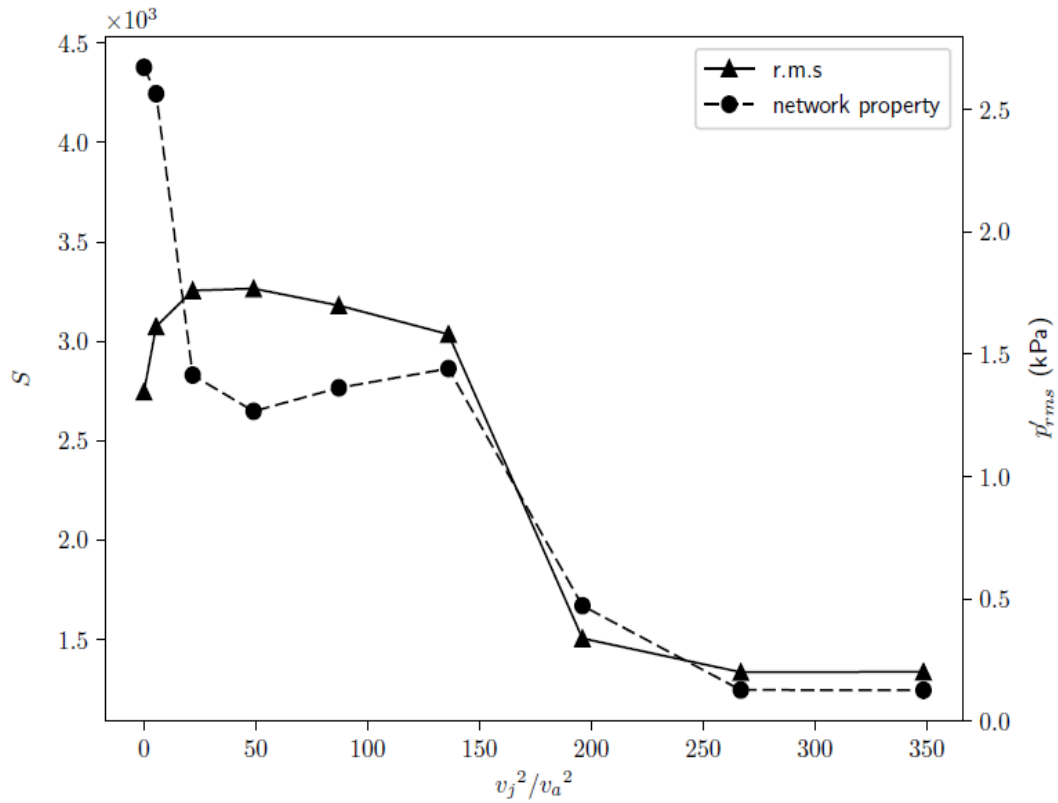
Figure 8.5: The variation of the temporal mean of the size of the largest cluster (S), marked as filled circles with respect to the total momentum flux ratio (v_j^2/v_a^2). The variation of p'_{rms} is also shown with filled triangles. A value of zero total momentum flux ratio corresponds to the baseline case, i.e., thermoacoustic instability with no micro-jet injection. The suppression of thermoacoustic instability happens due to the disintegration of large clusters of acoustic power sources into small ones.

To understand the physical mechanism causing the reduction in p'_{rms}, we perform simultaneous acoustic pressure and high-speed chemiluminescence measurements with injection at ports 2 and 3. We then perform time-varying local acoustic power network, as discussed in Chapter 4. We perform the network analysis in a region of interest of length 22 mm and width 20 mm covering the critical region on top of the bluff body shaft. Here also, we down-sample the resolution to 50% of the original resolution and

138

use a threshold of 1.0 for link connectivity between two nodes. This implies that two neighbouring nodes are connected if and only if the value of $p'\dot{q}'$ at the two nodes are above 1.0. After down-sampling, the number of nodes in the network is 8536. We compute the size of the largest cluster (S) of the acoustic power sources present in the region of interest, at each instant of time. Thus, at each value of the control air SLPM, there are 2000 networks and consequently 2000 values of S. In figure 8.5, we plot the variation of the temporal mean of S with respect to the total momentum flux ratio (v_j^2/v_a^2). Here, v_j is the total velocity of the jet through ports 2 and 3 and v_a is the velocity of the main air. We observe a sharp reduction in p'_{rms} when $v_j^2/v_a^2 \approx 200$. This is accompanied by a reduction in the temporal mean of S. Hence, the average size of the largest cluster of acoustic power source reduces as p'_{rms} plummets. This implies that suppression of thermoacoustic oscillations happen when large clusters of acoustic power sources disintegrates into small fragmented ones with optimum momentum flux ratio of micro-jet injection.

8.3   CONCLUSIONS

We perform passive control experiments by injecting air micro-jets at different locations along the length of the combustor. We find effective suppression of thermoacoustic oscillations with injection at port 5 (75% suppression) and simultaneous injection with ports 2 and 3 (85% suppression). These injection locations are located above the critical regions, on top of the bluff body and above the bluff body shaft just downstream of the dump plane respectively, identified by spatial correlation network analysis in Chapter 7. Hence, we can say that correlation network analysis helps one in identifying the optimal locations for injection of micro-jets to suppress the thermoacoustic oscillations. Traditionally, the ideal location for injection of control air

is determined by a large number of trials, investing a tremendous amount of money and time. The present approach using complex network analysis provides a smart and effective way to mitigate thermoacoustic oscillations.

CHAPTER 9

CONCLUSIONS AND SCOPE FOR FUTURE WORK

In the current thesis, we investigated the spatiotemporal dynamics of a turbulent thermoacoustic system during the transition to thermoacoustic instability from a state of combustion noise (the stable state of combustor operation) via intermittency. The turbulent thermoacoustic system used in the present study is a laboratory scale bluff body stabilized combustor. Such a turbulent thermoacoustic system can be considered as a complex system. Complex network is one of the popular tools to study complex systems. We use complex networks to explore the spatiotemporal dynamics during combustion noise, intermittency and thermoacoustic instability. To that end, we performed simultaneous acoustic pressure measurement, high-speed chemiluminescence of the flame dynamics and high-speed particle image velocimetry measurements at different equivalence ratios (control parameter) as the combustor dynamics transitions from combustion noise to thermoacoustic instability via intermittency.

During combustion noise, we observe small discrete vortices in the outer shear layer. During intermittency, as the amplitude of acoustic pressure fluctuation grows, these small vortices merge to form larger vortices. Merging of vortices accelerates combustion, leading to the proliferation of acoustic power sources in the flow field, which we call as the nucleation of acoustic power sources. The small fragmented clusters or islands of acoustic power sources thus coalesce to form larger clusters. As the damping in the system overcomes the acoustic driving, formation of large coherent

structures ceases and disintegration of large clusters into small fragmented ones occur. When the acoustic driving outweighs the damping, the onset of thermoacoustic instability occurs, which is characterized by large clusters of acoustic power sources. We constructed time-varying local acoustic power network to characterise the emergence of these large clusters of acoustic power sources at the onset of thermoacoustic instability. Using network measures such as link density, the size of the largest cluster and the number of clusters, we quantified the phenomenon of nucleation, coalescence and growth of acoustic power sources. The variation in the average size of the largest cluster of acoustic power sources suggests a percolation-like phase transition in the present combustor.

Next, we characterised the vorticity interactions of the turbulent reactive flow field during the three different dynamical states of combustor operation namely, combustion noise, intermittency and thermoacoustic instability. Here, we constructed time-varying weighted spatial networks based on Biot-Savart law. We observed that the topology of the vorticity network during combustion noise is scale-free. The hubs of the network corresponded to the small vortices present in the outer shear layer and the ones shed from the tip of the bluff body. The topology remains scale-free during the aperiodic and periodic epochs of intermittency. However, the hubs of the network that controls the spatiotemporal dynamics during the two epochs are different. During the aperiodic epochs of intermittency, the hubs of the network are the vortices present in the outer shear layer as well as the vortices shed from the tip of the bluff body, as observed during combustion noise. However, during the periodic epochs of intermittency, the coherent structures formed downstream of the dump plane acts as the hubs. During an acoustic cycle of thermoacoustic oscillations, the topology of the network oscillates between random and scale-free networks. Both the large coherent structure and the large vortex

142

that is shed from the tip of the bluff body act as the hubs of the vorticity network during one acoustic cycle. Hence, we observe that as the turbulent combustor dynamics transitions from combustion noise to thermoacoustic instability, the topology of the vorticity network transitions from scale-free to an oscillation between random and scale-free.

We constructed spatial networks, based on the correlation between the time series of velocity, during combustion noise, intermittency and thermoacoustic instability. Based on the spatial distribution of the network centrality measures, we identified critical regions in the flow field that control the spatiotemporal dynamics during the different dynamical states of combustor operation. During combustion noise, the bluff body wake is the most critical region. This finding is reinforced by the fact that the recirculation zone helps in the stabilization of the flame in the wake of the bluff body. During intermittency, the bluff body wake retains its importance. We identify two critical regions during thermoacoustic instability, namely, (a) the region on top of the bluff body shaft, just downstream of the dump plane and (b) the region on top of the bluff body.

Finally, we performed experiments to mitigate thermoacoustic instability by injecting air micro-jets at the top and the bottom walls of the combustion chamber. We obtained efficient suppression of thermoacoustic oscillations with injection at the above mentioned critical regions. The maximum suppression of thermoacoustic oscillations, around 85% reduction in p'_{rms}, is observed with injection at the critical region above the buff body shaft, downstream of the dump plane. Hence, we propose that complex networks provides a smart and effective way to mitigate thermoacoustic instability by helping in identifying the ideal location for injection of micro-jets, which are otherwise

143

chosen based on lot of trials. We find that the suppression of thermoacoustic oscillations at the critical region on top of the bluff body shaft happen due to the disruption of the large clusters of acoustic power sources.

Scope for future work

Complex network provides immense scope for the investigation of spatiotemporal analysis of thermoacoustic systems. Our study is the first step in this direction. Time-varying local acoustic power network analysis has helped us to unmask the physical mechanism behind the emergence of large clusters of acoustic power sources at the onset of thermoacoustic instability in the present combustor. The approach can be extended to characterize the spatiotemporal evolution of acoustic power sources in turbulent combustors with other flame holding mechanisms such as a swirler.

Turbulence network construction, using Biot-Savart law, has helped to uncover the nature of vorticity interaction during the different dynamical states of combustor operation in the present combustor. Using the same approach, recently, Murayama *et al.* (2018) constructed vorticity networks in a swirl stabilized turbulent combustor during thermoacoustic instability. They also reported the presence of scale-free behaviour. Further, they applied community detection (Newman 2006) on the vorticity network and observed that the detected communities of the network coincided with the vortices in the flow field. This opens up a possibility of exploring community detection as a tool for vortex detection. It would be interesting to apply the same during the intermittency route to thermoacoustic instability and obtain a scaling law for the size of the vortices, obtained from the size of the communities, during the different dynamical states of combustor operation.

Unni and Sujith (2017) investigated the flame dynamics during the dynamical states of combustion noise, intermittency and thermoacoustic instability. They observed the roll up the flame along the outer shear by the ring vortices and the large coherent structure during the periodic epochs of intermittency and thermoacoustic instability respectively. It would be interesting to examine the behaviour of the vorticity network topologies with respect to the flame dynamics during the different states of combustor operation.

So far, researchers have examined the local acoustic power field and the velocity field separately during the different states of the combustor operation. Multilayer network analysis (Boccaletti *et al.* 2014) is one promising approach that can provide insight into the interaction of these two fields as the combustor dynamics transitions from the state of combustion noise to thermoacoustic instability via intermittency.

In the present study, we have identified the critical regions in the flow field by constructing spatial networks based on Pearson's correlation. Pearson's correlation takes into account only the linear relationship between two variables. In a turbulent thermoacoustic system, the interaction amongst the hydrodynamics, the acoustic field and the flame dynamics is highly nonlinear. Hence, it would be interesting to perform the analysis with a statistical measure that takes into account the nonlinear relationship between the variables. Mutual information (Donges *et al.* 2009) and transfer entropy (Tung *et al.* 2007) looks promising in this aspect. Hence, spatial network analysis using the abovementioned two measures may improve the identification of critical regions in the flow field during the different states of combustor operation. Smart and effective suppression of thermoacoustic oscillation by injecting micro-jets at the critical regions identified from network analysis opens up a new avenue in the area of control of other fluid mechanical instabilities involving turbulent flow.

Further, it would be interesting to see what happens to the critical region once thermoacoustic oscillations are suppressed. To that end, we have to perform spatial network analysis during thermoacoustic instability with injection of micro-jets at the critical region. With micro-jet injections at the top and bottom walls of the present combustor, it is impossible to perform high-speed particle image velocimetry. This issue can be circumvent by modifying the dump plane of the combustor. In future, we plan to inject micro-jets at the dump plane in an inclined manner, targeting the critical region. We hypothesize that the region on top of the bluff body shaft, which was identified as the critical region, will not be critical (the region will not have high values of network centrality measures) with suppression of thermoacoustic instability.

Like thermoacoustic instability, another phenomenon, which is undesirable for both aircraft and land-based gas turbine engines is lean blowout (Shanbhogue, Husain and Lieuwen 2009). The methodology adopted in the present study can be used to investigate the spatiotemporal dynamics during the transition to lean blowout in turbulent combustors.

APPENDIX

A. SENSITIVITY OF NETWORK PROPERTIES WITH RESPECT TO THE THRESHOLD OF NETWORK LINK CONNECTIVITY (ϵ)
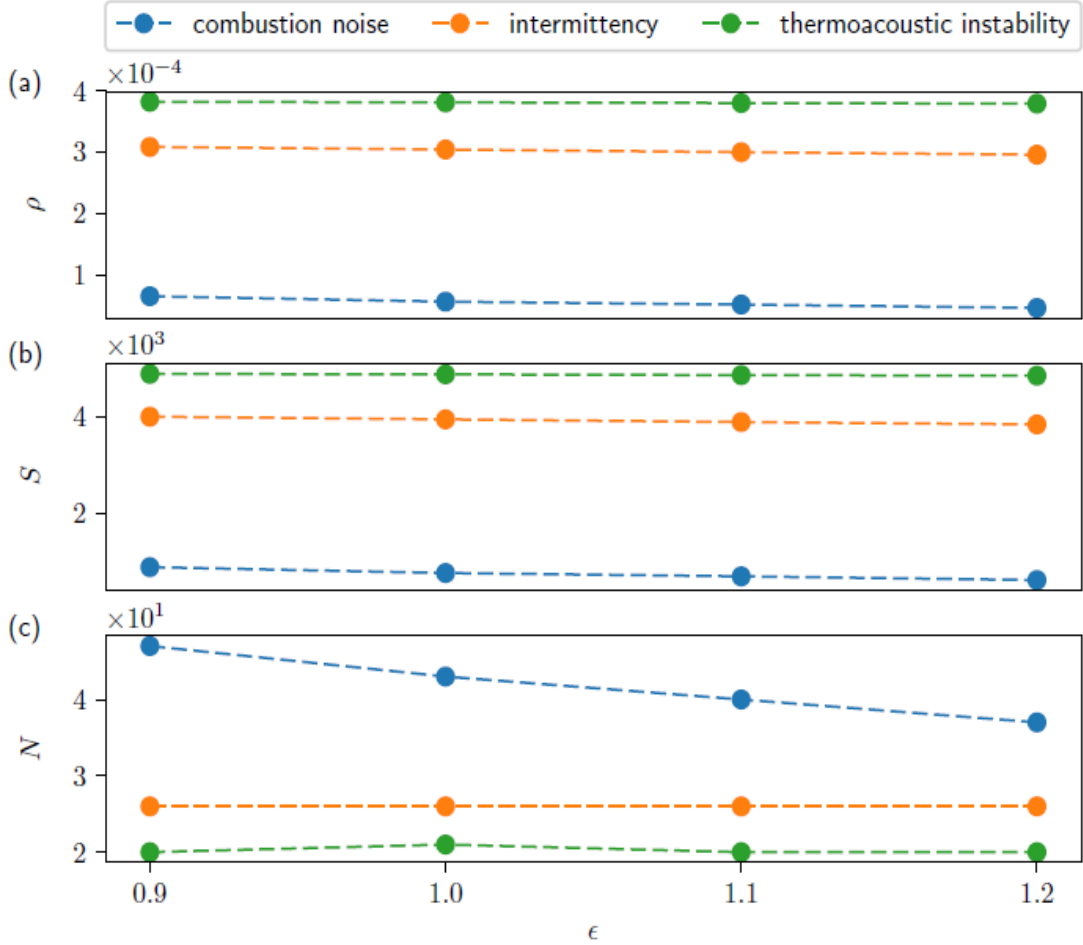
FIGURE A1. Variation of the temporal mean of the network properties (a) the link density (ρ), (b) the size of the giant cluster (S) and (c) the number of clusters (N) with respect to different thresholds of network link connectivity for a case of combustion noise ($\varphi = 1.01$), intermittency ($\varphi = 0.72$) and thermoacoustic instability ($\varphi = 0.64$). Here, the temporal mean is calculated over 2000 images/networks. We observe that the variation in the temporal mean of the network properties for a threshold of 1.0 and above is negligible.

Figure A1 shows the variation of the temporal mean of the network properties namely, ρ (figure A1a), S (figure A1b) and N (figure A1c) with respect to different thresholds of network link connectivity (ϵ) for a case of combustion noise ($\varphi = 1.01$),

intermittency ($\varphi = 0.72$) and thermoacoustic instability ($\varphi = 0.64$). The temporal mean is calculated over 2000 images/networks. The average link density and the average size of the giant cluster remain almost a constant for combustion noise, intermittency and thermoacoustic instability for different thresholds of network link connectivity. For the case of combustion noise, we observe a decrease of around 7 % and 7.5% in the average number of clusters of acoustic power sources when ϵ is increased from 1.0 to 1.1 and from 1.1 to 1.2 respectively. Nevertheless, the average number of clusters of acoustic power sources do no change for intermittency and thermoacoustic instability for $\epsilon \geq 1.0$. This justifies the use of $\epsilon = 1.0$ for the network link connectivity in the current analysis.

B.   CONVERGENCE OF NETWORK PROPERTIES WITH RESPECT TO THE NUMBER OF IMAGES/NETWORKS

Figure A2 shows the variation of the temporal mean of the network properties namely, ρ (figure A2a), S (figure A2b) and N (figure A2c) calculated over different number of images/networks for a case of combustion noise ($\varphi = 1.01$), intermittency ($\varphi = 0.72$) and thermoacoustic instability ($\varphi = 0.64$). The average link density and the size of the giant cluster remain nearly a constant for combustion noise, intermittency and thermoacoustic instability when calculated over the entire range of number of images/networks. The average number of clusters of acoustic power sources saturates for combustion noise, intermittency and thermoacoustic instability when computed over 1500 images/networks and above. This justifies the choice of 2000 images/networks for the computation of the statistical measures of the network properties.
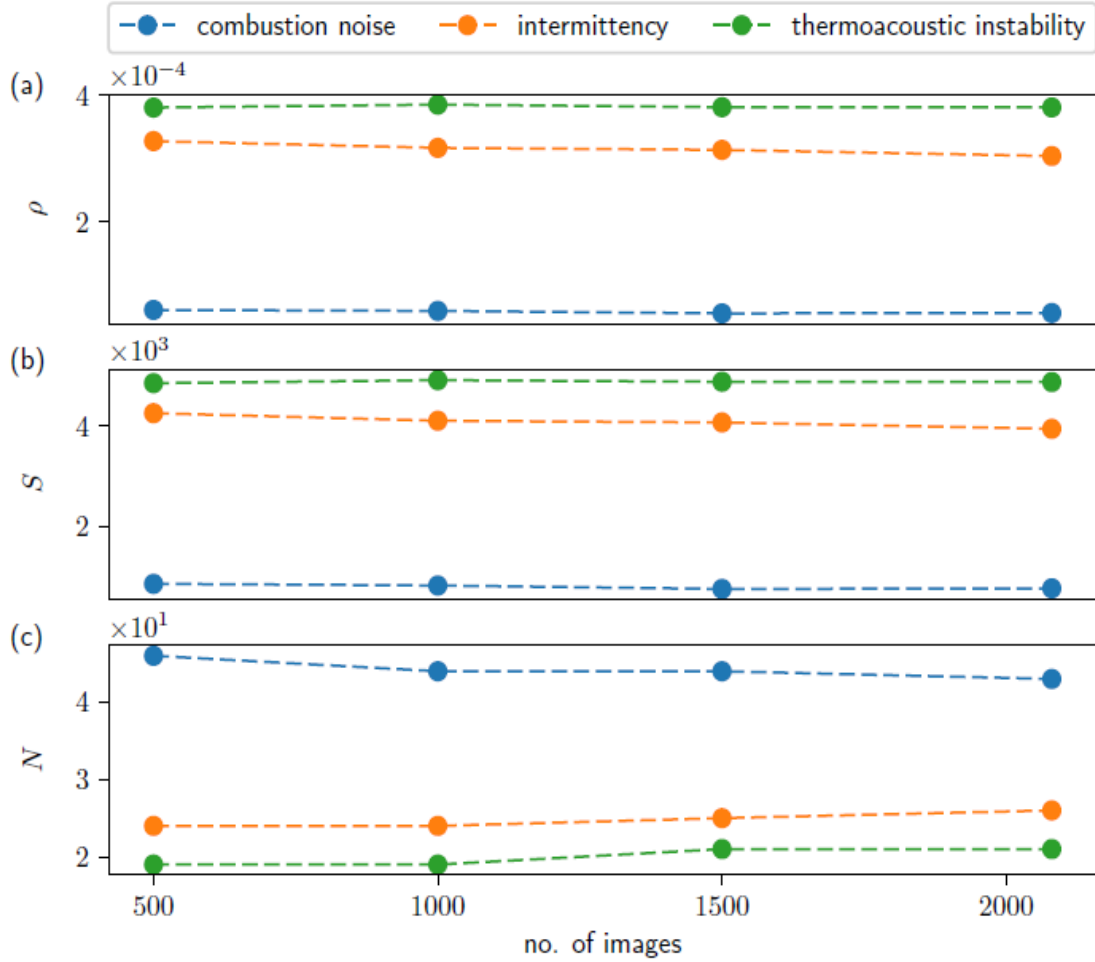
FIGURE A2. Variation of the temporal mean of the network properties (a) the link density (ρ), (b) the size of the giant cluster (S) and (c) the number of clusters (N) calculated over 500, 1000, 1500 and 2080 images/networks for a case of combustion noise ($\varphi = 1.01$), intermittency ($\varphi = 0.72$) and thermoacoustic instability ($\varphi = 0.64$). Here, the threshold for the connectivity of links in the acoustic power network is fixed at 1.0. We observe that the temporal mean of all the network properties for combustion noise, intermittency and thermoacoustic instability remains almost a constant when computed over a total of 1500 images/networks and above.

C. SELECTION OF PEARSON'S CORRELATION COEFFICIENT THRESHOLD FOR NETWORK CONSTRUCTION
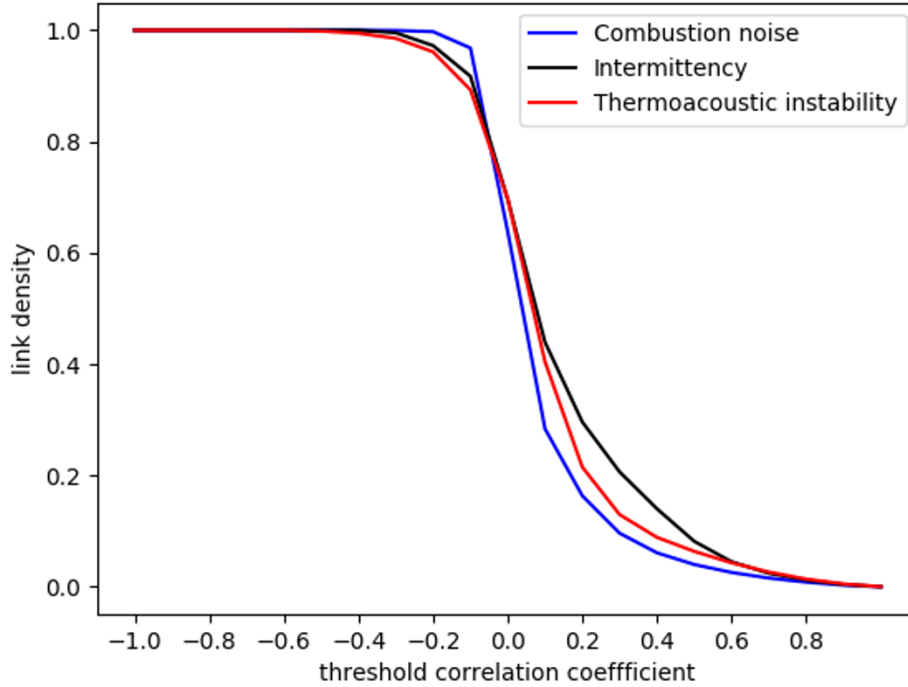
Figure A3: The variation of link density at different values of threshold Pearson's correlation coefficient for combustion noise, intermittency and thermoacoustic instability. We chose 0.25 as the threshold Pearson's correlation coefficient for network construction as at this value of Pearson's correlation coefficient, the variation in link density across the three states of combustor operation is maximum. Maximum variation in link density ensures maximum variation in the spatial distribution of network properties thus helping us to discern the critical regions during the three states of combustor operation.

We construct a spatial network for combustion noise ($\varphi = 1.01$), intermittency ($\varphi = 0.72$) and thermoacoustic instability ($\varphi = 0.64$) for different values of the threshold correlation coefficient ranging from -1 to 1. At each of the threshold correlation coefficient, we compute the link densities of the networks thus obtained. In figure A3,

we plot the variation of the link density with respect to the threshold correlation coefficient. We observe that the maximum variation of link density across combustion noise, intermittency and thermoacoustic instability occurs at 0.25. Maximum variation in link density ensures maximum variation in the topology of the network. Maximum variation in network topology will be reflected in the spatial distribution of the network properties across the different dynamical states of combustor operation as well.

REFERENCES

1. **Abarbanel, H.** *Analysis of observed chaotic data*. Springer-Verlag New York, Inc., (1996).

2. **Abugov, D. I.,** and **Obrezkov, O. I.** (1978). Acoustic noise in turbulent flames. *Combustion, Explosion and Shock Waves*, **14**(5), 606-612.

3. **Albert, R.,** and **Barabási, A. L.** (2002) Statistical mechanics of complex networks. *Reviews of modern physics*, **74**(1), 47.

4. **Albert, R., Jeong, H.,** and **Barabási, A. L.** (1999). Internet: Diameter of the world-wide web. *Nature*, **401**(6749), 130.

5. **Altay, H. M., Hudgins, D. E., Speth, R. L., Annaswamy, A. M.,** and **Ghoniem, A. F.** (2010). Mitigation of thermoacoustic instability utilizing steady air injection near the flame anchoring zone. *Combustion and Flame*, **157**(4), 686-700.

6. **Ananthkrishnan, N., Deo, S.,** and **Culick, F. E.** (2005) Reduced-order modeling and dynamics of nonlinear acoustic waves in a combustion chamber. *Combustion Science and Technology*, **177**(2), 221-248.

7. **Anderson, W. E., Miller, K. L., Ryan, H. M., Pal, S., Santoro, R. J.,** and **Dressler, J. L.** (1998). Effects of periodic atomization on combustion instability in liquid-fueled propulsion systems. *Journal of Propulsion and Power*, **14**(5), 818-825.

8. **Balachandran, R., Ayoola, B. O., Kaminski, C. F., Dowling, A. P.,** and **Mastorakos, E**. (2005). Experimental investigation of the nonlinear response of turbulent premixed flames to imposed inlet velocity oscillations. *Combustion and Flame*, **143**(1-2), 37-55.

9. **Balasubramanian, K.,** and **Sujith, R. I.** (2008*a*). Non-normality and nonlinearity in combustion–acoustic interaction in diffusion flames. *Journal of Fluid Mechanics*, **594**, 29-57.

10. **Balasubramanian, K.,** and **Sujith, R. I.** (2008*b*). Thermoacoustic instability in a Rijke tube: Non-normality and nonlinearity. *Physics of Fluids*, **20**(4), 044103.

11. **Barabási, A. L.** (2011). The network takeover. *Nature Physics*, **8**(1), 14.

12. **Barabasi, A. L.** *Linked: How everything is connected to everything else and what it means for business, science, and everyday life*. Basic Books, New York, 2003.

13. **Barabási, A. L.** *Network science*. Cambridge university press, 2016.

14. **Barabási, A. L.,** and **Albert, R.** (1999) Emergence of scaling in random networks. *Science*, **286**(5439), 509-512.

15. **Barabási, A. L.,** and **Bonabeau, E.** (2003). Scale-free networks. *Scientific American*, **288**(5), 60-69.

16. **Barthélemy, M.** (2011). Spatial networks. *Physics Reports*, **499**(1-3), 1-101.

17. **Bar-Yam, Y**. *Dynamics of complex systems* (Vol. 213). Reading, MA: Addison-Wesley, 1997.

18. **Bellows, B. D., Bobba, M. K., Forte, A., Seitzman, J. M.,** and **Lieuwen, T.** (2007). Flame transfer function saturation mechanisms in a swirl-stabilized combustor. *Proceedings of the combustion institute*, **31**(2), 3181-3188.

19. **Birbaud, A. L., Durox, D., Ducruix, S.,** and **Candel, S.** (2007). Dynamics of confined premixed flames submitted to upstream acoustic modulations. *Proceedings of the Combustion Institute*, **31**(1), 1257-1265.

20. **Bloxsidge, G. J., Dowling, A. P.,** and **Langhorne, P. J.** (1988). Reheat buzz: an acoustically coupled combustion instability. Part 2. Theory. *Journal of fluid mechanics*, **193**, 445-473.

21. **Boccaletti, S., Bianconi, G., Criado, R., Del Genio, C. I., Gómez-Gardenes, J., Romance, M., Sendina-Nadal, I., Wang, Z.,** and **Zanin, M.** (2014). "The structure and dynamics of multilayer networks." *Physics Reports,* **544**(1), 1-122.

22. **Boccaletti, S., Latora, V., Moreno, Y., Chavez, M.,** and **Hwang**, D. U. (2006) Complex networks: Structure and dynamics. *Physics reports*, **424**(4-5), 175-308.

23. **Boers, N., Bookhagen, B., Barbosa, H. M., Marwan, N., Kurths, J.,** and **Marengo, J. A.** (2014). Prediction of extreme floods in the eastern Central Andes based on a complex networks approach. *Nature communications*, **5**, 5199.

24. **Bollobas, B.** *Modern Graph Theory*. Springer Science and Business Media, 1998.

25. **Burnley, V. S.,** and **Culick, F. E. C.** (2000). Influence of random excitations on acoustic instabilities in combustion chambers. *AIAA journal*, **38**(8), 1403-1410.

26. **Cabral, J., Kringelbach, M. L.,** and **Deco, G.** (2017) Functional connectivity dynamically evolves on multiple time-scales over a static structural connectome: Models and mechanisms. *NeuroImage*.

27. **Candel, S.** (2002) Combustion dynamics and control: Progress and challenges. *Proceedings of the combustion institute*, **29**(1), 1-28.

28. **Cao, L.** (1997). Practical method for determining the minimum embedding dimension of a scalar time series. *Physica D: Nonlinear Phenomena*, **110**(1-2), 43-50.

29. **Chakravarthy, S. R., Shreenivasan, O. J., Boehm, B., Dreizler, A.,** and **Janicka, J.** (2007). Experimental characterization of onset of acoustic instability in a nonpremixed half-dump combustor. *The Journal of the Acoustical Society of America*, **122**(1), 120-127.

30. **Charakopoulos, A. K., Karakasidis, T. E., Papanicolaou, P. N.,** and **Liakopoulos, A.** (2014). The application of complex network time series analysis in turbulent heated jets. *Chaos: An Interdisciplinary Journal of Nonlinear Science*, **24**(2), 024408.

31. **Chiocchini, S., Pagliaroli, T., Camussi, R.,** and **Giacomazzi, E.** (2017). Chaotic and linear statistics analysis in thermoacoustic instability detection. *Journal of Propulsion and Power*, **34**(1), 15-26.

32. **Chishty, W. A.** (2005). *Effects of thermoacoustic oscillations on spray combustion dynamics with implications for lean direct injection systems*, Ph.D. thesis, Virginia Tech.

33. **Clavin, P., Kim, J. S.,** and **Williams, F. A.** (1994) Turbulence-induced noise effects on high-frequency combustion instabilities. *Combustion Science and Technology*, **96**(1-3), 61-84.

34. **Coats, C. M.** (1996) Coherent structures in combustion. *Progress in Energy and Combustion Science*, **22**(5), 427-509.

35. **Conrad, T., Bibik, A., Lee, J. Y., Lubarsky, E.,** and **Zinn, B.** (2003). Control of Combustion Instabilities by Fuel Spray Modification Using Smart Fuel Injector. In *39th AIAA/ASME/SAE/ASEE Joint Propulsion Conference and Exhibit* (p. 4937).

36. **Correa, S. M.** (1993). A review of NOx formation under gas-turbine combustion conditions. *Combustion science and technology*, **87**(1-6), 329-362.

37. **Crocco, L.,** and **Cheng, S. I.** *Theory of combustion instability in liquid propellant rocket motors*. Princeton Univ Nj, 1956.

38. **Culick, F. E. C,** (1988). Combustion Instabilities in Liquid-Fuelled Propulsion Systems—An Overview, In *AGARD Conference on Combustion Instabilities in Liquid-Fuelled Propulsion Systems, Bath, AGARD-CP-450* (pp. 1-1).

39. **Culick, F. E. C.** (1994). Some recent results for nonlinear acoustics in combustion chambers. *AIAA journal*, **32**(1), 146-169.

40. **Culick, F. E. C.,** and **Kuentzmann, P.** (2006) *Unsteady motions in combustion chambers for propulsion systems*. Technical report. NATO Research and Technology Organization Neuilly-Sur-Seine (France).

41. **Culick, F. E. C.,** and **Yang, V.** (1995). Overview of combustion instabilities in liquid-propellant rocket engines. *Liquid Rocket Engine Combustion Instability*, **169**, 3-37.

42. **Datta, S., Mondal, S., Mukhopadhyay, A., Sanyal, D.,** and **Sen, S.** (2009). An investigation of nonlinear dynamics of a thermal pulse combustor. *Combustion Theory and Modelling*, **13**(1), 17-38.

43. **Davidsen, J., Ebel, H.,** and **Bornholdt, S.** (2002). Emergence of a small world from local interactions: Modeling acquaintance networks. *Physical Review Letters*, **88**(12), 128701.

44. **Deb, D., Vishveshwara, S.,** and **Vishveshwara, S.** (2009). Understanding protein structure from a percolation perspective. *Biophysical journal*, **97**(6), 1787-1794.

45. **Deshmukh, N. N.,** and **Sharma, S. D.** (2017). Suppression of thermo-acoustic instability using air injection in horizontal Rijke tube. *Journal of the Energy Institute*, **90**(3), 485-495.

46. **Dickinson L. A.,** (1962). Command initiation of finite wave axial combustion instability in solid propellant rocket engines. *ARS J*, **32**, 643-644.

47. **Dimitriadis, S. I., Laskaris, N. A., Tsirka, V., Vourkas, M., Micheloyannis, S.,** and **Fotopoulos, S.** (2010) Tracking brain dynamics via time-dependent network analysis. *Journal of neuroscience methods*, **193**(1), 145-155.

48. **Domen, S., Gotoda, H., Kuriyama, T., Okuno, Y.,** and **Tachibana, S.** (2015). Detection and prevention of blowout in a lean premixed gas-turbine model combustor using the concept of dynamical system theory. *Proceedings of the Combustion Institute*, **35**(3), 3245-3253.

49. **Donges, J. F., Zou, Y., Marwan, N.,** and **Kurths, J.** (2009) Complex networks in climate dynamics. *The European Physical Journal Special Topics*, **174**(1), 157-179.

50. **Donner, R. V., Zou, Y., Donges, J. F., Marwan, N.,** and **Kurths, J.** (2010). Recurrence networks—a novel paradigm for nonlinear time series analysis. *New Journal of Physics*, **12**(3), 033025.

51. **Doron, K. W., Bassett, D. S.,** and **Gazzaniga, M. S.** (2012) Dynamic network structure of interhemispheric coordination. *Proceedings of the National Academy of Sciences*, **109**(46), 18661-18668.

52. **Dowling, A. P.** (1995). The calculation of thermoacoustic oscillations. *Journal of sound and vibration*, **180**(4), 557-581.

53. **Dowling, A. P.** (1997). Nonlinear self-excited oscillations of a ducted flame. *Journal of fluid mechanics*, **346**, 271-290.

54. **Dowling, A. P.,** and **Ffowcs Williams**, **J. E.** *Sound and sources of sound*. Horwood, 1983.

55. **Dowling, A. P.,** and **Morgans, A. S.** (2005). Feedback control of combustion oscillations. *Annu. Rev. Fluid Mech.*, **37**, 151-182.

56. **Ducruix, S., Durox, D.,** and **Candel, S.** (2000). Theoretical and experimental determinations of the transfer function of a laminar premixed flame. *Proceedings of the combustion institute*, **28**(1), 765-773.

57. **Ebi, D., Denisov, A., Bonciolini, G., Boujo, E.,** and **Noiray, N.** (2018). Flame Dynamics Intermittency in the Bistable Region Near a Subcritical Hopf Bifurcation. *Journal of Engineering for Gas Turbines and Power*, **140**(6), 061504.

58. **Elias, I.** (1959). Acoustical Resonances Produced by Combustion of a Fuel-Air Mixture in a Rectangular Duct. *The Journal of the Acoustical Society of America*, **31**(3), 296-304.

59. **Emerson, B., O'Connor, J., Juniper, M.,** and **Lieuwen, T.** (2012) Density ratio effects on reacting bluff-body flow field characteristics. *Journal of Fluid Mechanics*, **706**, 219-250.

60. **Ffowcs-Williams, J. E.** (1984). Review Lecture-Anti-sound. *Proc. R. Soc. Lond. A*, **395**(1808), 63-88.

61. **Fleifil, M., Annaswamy, A. M., Ghoneim, Z. A.,** and **Ghoniem, A. F.** (1996). Response of a laminar premixed flame to flow oscillations: A kinematic model and thermoacoustic instability results. *Combustion and flame*, **106**(4), 487-510.

62. **Fornito, A., Zalesky, A.,** and **Bullmore, E.** *Fundamentals of brain network analysis*. Academic Press, 2016.

63. **Fraser, A. M.,** and **Swinney, H. L.** (1986). Independent coordinates for strange attractors from mutual information. *Physical review A*, **33**(2), 1134.

64. **Frish, U.,** and **Parisi, G.** On the singularity structure of fully developed turbulence. In **Gil, R**. **B. M.** and **Parisi, G.** (eds.), Turbulence and Prediction in Geophysical Fluid Dynamics. North-Holland, 84-88, 1985.

65. **Gallos, L. K., Makse, H. A.,** and **Sigman, M.** (2012). A small world of weak ties provides optimal global integration of self-similar modules in functional brain networks. *Proceedings of the National Academy of Sciences*, **109**(8), 2825-2830.

66. **George, N. B., Unni, V. R., Raghunathan, M.,** and **Sujith, R. I.** (2018) Pattern formation during transition from combustion noise to thermoacoustic instability via intermittency. *Journal of Fluid Mechanics*, **849**, 615-644.

67. **Ghenai, C., Smith, O.,** and **Karagozian, A.** (2001). Acoustical excitation of burning fuel droplets. In *39th Aerospace Sciences Meeting and Exhibit* (p. 328).

68. **Godavarthi, V., Unni, V. R., Gopalakrishnan, E. A.,** and **Sujith, R. I.** (2017) Recurrence networks to study dynamical transitions in a turbulent combustor. *Chaos: An Interdisciplinary Journal of Nonlinear Science*, **27**(6), 063113.

69. **Gopalakrishnan, E. A.,** and **Sujith, R. I.** (2015). Effect of external noise on the hysteresis characteristics of a thermoacoustic system. *Journal of Fluid Mechanics*, **776**, 334-353.

70. **Gopalakrishnan, E. A., Sharma, Y., John, T., Dutta, P. S.,** and **Sujith, R. I.** (2016). Early warning signals for critical transitions in a thermoacoustic system. *Scientific reports*, **6**, 35310.

71. **Gotoda, H., Amano, M., Miyano, T., Ikawa, T., Maki, K.,** and **Tachibana, S.** (2012) Characterization of complexities in combustion instability in a lean premixed gas-turbine model combustor. *Chaos: An Interdisciplinary Journal of Nonlinear Science*, **22**(4), 043128.

72. **Gotoda, H., Kinugawa, H., Tsujimoto, R., Domen, S.,** and **Okuno, Y.** (2017) Characterization of Combustion Dynamics, Detection, and Prevention of an Unstable Combustion State Based on a Complex-Network Theory. *Physical Review Applied*, **7**(4), 044027.

73. **Gotoda, H., Nikimoto, H., Miyano, T.,** and **Tachibana, S.** (2011) Dynamic properties of combustion instability in a lean premixed gas-turbine combustor. *Chaos: An Interdisciplinary Journal of Nonlinear Science*, **21**(1), 013124.

74. **Gotoda, H., Shinoda, Y., Kobayashi, M., Okuno, Y.,** and **Tachibana, S.** (2014) Detection and control of combustion instability based on the concept of dynamical system theory. *Physical Review E*, **89**(2), 022910.

75. **Gutmark, E., Schadow, K. C., Parr, T. P., Hanson-Parr, D. M.,** and **Wilson, K. J.** (1989). Noncircular jets in combustion systems. *Experiments in Fluids*, **7**(4), 248-258.

76. **Hagberg, A., Swart, P.,** and **S Chult, D.** (2008). *Exploring network structure, dynamics, and function using NetworkX* (No. LA-UR-08-05495; LA-UR-08-5495). Los Alamos National Lab.(LANL), Los Alamos, NM (United States).

77. **Heckl, M. A.** (1988). Active control of the noise from a Rijke tube. *Journal of Sound and Vibration*, **124**(1), 117-133.

78. **Hegde, U. G., Reuter, D., and Zinn, B. T**. (1988) Sound generation by ducted flames. *AIAA journal*, **26**(5), 532-537.

79. **Higgins, B.** (1802). On the sound produced by a current of hydrogen gas passing through a tube. *Journal of natural philosophy, chemistry and the arts*, **1**(129-131), 2.

80. **Holme, P.,** and **Saramäki, J.** (2012). Temporal networks. *Physics reports*, **519**(3), 97-125.

81. **Huang, Y.,** and **Yang, V.** (2009). Dynamics and stability of lean-premixed swirl-stabilized combustion. *Progress in energy and combustion science*, **35**(4), 293-364.

82. **Hult, J., Meier, U., Meier, W., Harvey, A.,** and **Kaminski, C. F.** (2005) Experimental analysis of local flame extinction in a turbulent jet diffusion flame by high repetition 2-D laser techniques and multi-scalar measurements. *Proceedings of the Combustion Institute*, **30**(1), 701-709.

83. **Hurle, I. R., Price, R. B., Sugden, T. M.,** and **Thomas, A.** (1968). Sound emission from open turbulent premixed flames. *Proc. R. Soc. Lond. A*, **303**(1475), 409-427.

84. **Iyengar, V., Simmons, H., Ransom, D.,** and **Holzschuh, T.** (2010). Flash Atomization: A New Concept to Control Combustion Instability in Water Injected Gas Turbines. In *ASME Turbo Expo 2010: Power for Land, Sea, and Air* (pp. 313-322). American Society of Mechanical Engineers.

85. **Jahnke, C. C.,** and **Culick, F. E. C.** (1994). Application of dynamical systems theory to nonlinear combustion instabilities. *Journal of propulsion and power*, **10**(4), 508-517.

86. **Jegadeesan, V.,** and **Sujith, R. I.** (2013). Experimental investigation of noise induced triggering in thermoacoustic systems. *Proceedings of the Combustion Institute*, **34**(2), 3175-3183.

87. **Juniper, M. P.** (2011). Triggering in the horizontal Rijke tube: non-normality, transient growth and bypass transition. *Journal of Fluid Mechanics*, **667**, 272-308.

88. **Juniper, M. P.,** and **Sujith, R. I.** (2018) Sensitivity and nonlinearity of thermoacoustic oscillations. *Annual Review of Fluid Mechanics*, **50**, 661-689.

89. **Kabiraj, L.,** and **Sujith, R. I.** (2012). Nonlinear self-excited thermoacoustic oscillations: intermittency and flame blowout. *Journal of Fluid Mechanics*, *713*, 376-397.

90. **Kabiraj, L., Saurabh, A., Wahi, P.,** and **Sujith, R. I.** (2012). Route to chaos for combustion instability in ducted laminar premixed flames. *Chaos: An Interdisciplinary Journal of Nonlinear Science*, *22*(2), 023129.

91. **Kabiraj, L., Sujith, R. I.,** and **Wahi, P.** (2012). Bifurcations of self-excited ducted laminar premixed flames. *Journal of Engineering for Gas Turbines and Power*, *134*(3), 031502.

92. **Kantelhardt, J. W., Koscielny-Bunde, E., Rego, H. H., Havlin, S.,** and **Bunde, A.** (2001). Detecting long-range correlations with detrended fluctuation analysis. *Physica A: Statistical Mechanics and its Applications*, **295**(3-4), 441-454.

93. **Kantelhardt, J. W., Zschiegner, S. A., Koscielny-Bunde, E., Havlin, S., Bunde, A.,** and **Stanley, H. E.** (2002). Multifractal detrended fluctuation analysis of nonstationary time series. *Physica A: Statistical Mechanics and its Applications*, **316**(1-4), 87-114.

94. **Kashinath, K., Hemchandra, S.,** and **Juniper, M. P.** (2013). Nonlinear thermoacoustics of ducted premixed flames: the influence of perturbation convection speed. *Combustion and Flame*, **160**(12), 2856-2865.

95. **Kashinath, K., Waugh, I. C.,** and **Juniper, M. P.** (2014). Nonlinear self-excited thermoacoustic oscillations of a ducted premixed flame: bifurcations and routes to chaos. *Journal of Fluid Mechanics*, **761**, 399-430.

96. **Kaskan, W. E.,** and **Noreen, A. E.** (1955). High-frequency oscillations of a flame held by a bluff body. *ASME Transactions*, **77**(6), 855-891.

97. **Ken, H. Y., Trouve, A.,** and **Daily, J. W.** (1991). Low-frequency pressure oscillations in a model ramjet combustor. *Journal of Fluid Mechanics*, **232**, 47-72.

98. **Kheirkhah, S., Cirtwill, J. M., Saini, P., Venkatesan, K.,** and **Steinberg, A. M.** (2017) Dynamics and mechanisms of pressure, heat release rate, and fuel spray coupling during intermittent thermoacoustic oscillations in a model aeronautical combustor at elevated pressure. *Combustion and Flame*, **185**, 319-334.

99. **Kochenburger, R. J.** (1950). A frequency response method for analyzing and synthesizing contactor servomechanisms. *Transactions of the American Institute of Electrical Engineers*, **69**(1), 270-284.

100. **Koffel, W. K., Smolak, G. R.,** and **Trout, A. M.** (1956). Investigation of afterburner combustion screech and methods of its control at high combustor pressure levels.

101. **Komarek, T.,** and **Polifke, W**. (2010). Impact of swirl fluctuations on the flame response of a perfectly premixed swirl burner. *Journal of Engineering for Gas Turbines and Power*, **132**(6), 061503.

102. **Krebs, Werner, Sven Bethke, Joachim Lepers, Patrick Flohr, Bernd Prade, Cliff Johnson,** and **Stan Sattinger.** *Thermoacoustic design tools and passive control: Siemens power generation approaches*. Chapter 5 in: Lieuwen, T. and Yang, V., editors. *Combustion Instabilities in Gas Turbine Engines Operational Experience, Fundamental Mechanisms and Modeling*, 2005.

103. **Kulkarni, R., Balasubramanian, K.,** and **Sujith, R. I.** (2011). Non-normality and its consequences in active control of thermoacoustic instabilities. *Journal of Fluid Mechanics*, **670**, 130-149.

104. **Lacasa, L., Luque, B., Ballesteros, F., Luque, J.,** and **Nuno, J. C.** (2008). From time series to complex networks: The visibility graph. *Proceedings of the National Academy of Sciences*, **105**(13), 4972-4975.

105. **Lacasa, L., Luque, B., Luque, J.,** and **Nuno, J. C.** (2009). The visibility graph: A new method for estimating the Hurst exponent of fractional Brownian motion. *EPL (Europhysics Letters)*, **86**(3), 30001.

106. **Landau, L. D.** (1944). On the theory of slow combustion. *Acta Physicochim (USSR)*, **19**, 77-85.

107. **Langhorne, P. J.** (1988). Reheat buzz: an acoustically coupled combustion instability. Part 1. Experiment. *Journal of Fluid Mechanics*, **193**, 417-443.

108. **Langhorne, P. J., Dowling, A. P.,** and **Hooper, N.** (1990). Practical active control system for combustion oscillations. *Journal of Propulsion and Power*, **6**(3), 324-333.

109. **Latora, V.,** and **Marchiori, M.** (2001). Efficient behaviour of small-world networks. *Physical review letters*, **87**(19), 198701.

110. **Lee, J. G.,** and **Santavicca, D. A.** (2003). Experimental diagnostics for the study of combustion instabilities in lean premixed combustors. *Journal of propulsion and power*, **19**(5), 735-750.

111. **Lei, S.,** and **Turan, A.** (2009). Nonlinear/chaotic behaviour in thermo-acoustic instability. *Combustion Theory and Modelling*, **13**(3), 541-557.

112. **Lepers, J., Krebs, W., Prade, B., Flohr, P., Pollarolo, G.,** and **Ferrante, A.** (2005). Investigation of thermoacoustic stability limits of an annular gas turbine combustor test-rig with and without Helmholtz-resonators. In *ASME Turbo Expo 2005: Power for Land, Sea, and Air* (pp. 177-189). American Society of Mechanical Engineers.

113. **Lieuwen, T. C.** (2005). Online combustor stability margin assessment using dynamic pressure data. *J. Eng. Gas Trbines Power*, **127**, 478-482.

114. **Lieuwen, T. C.** (2002) Experimental investigation of limit-cycle oscillations in an unstable gas turbine combustor. *Journal of Propulsion and Power*, **18**(1), 61-67.

115. **Lieuwen, T. C.,** and **Banaszuk, A.** (2005) Background noise effects on combustor stability. *Journal of Propulsion and Power*, **21**(1), 25-31.

116. **Lieuwen, T. C.,** and **Neumeier, Y.** (2002). Nonlinear pressure-heat release transfer function measurements in a premixed combustor. *Proceedings of the Combustion Institute*, **29**(1), 99-105.

117. **Lieuwen, T. C., Neumeier, Y.,** and **Zinn, B. T.** (1998). The role of unmixedness and chemical kinetics in driving combustion instabilities in lean premixed combustors. *Combustion Science and Technology*, **135**(1-6), 193-211.

118. **Lieuwen, T. C., Torres, H., Johnson, C.,** and **Zinn, B. T.** (1999). A mechanism of combustion instability in lean premixed gas turbine combustors. In *ASME 1999 International Gas Turbine and Aeroengine Congress and Exhibition* (pp. V002T02A001-V002T02A001). American Society of Mechanical Engineers.

119. **Lieuwen, T., C.,** and **Yang**, **V.** eds. *Combustion instabilities in gas turbine engines: operational experience, fundamental mechanisms, and modeling*. American Institute of Aeronautics and Astronautics, 2005.

120. **Liu, C., Zhou, W. X.,** and **Yuan, W. K.** (2010). Statistical properties of visibility graph of energy dissipation rates in three-dimensional fully developed turbulence. *Physica A: Statistical Mechanics and its Applications*, **389**(13), 2675-2681.

121. **Lu, Z., Yuan, N.,** and **Fu, Z.** (2016). Percolation Phase Transition of Surface Air Temperature Networks under Attacks of El Niño/La Niña. *Scientific reports*, **6**, 26779.

122. **Lubarsky, E., Shcherbik, D., Bibik, A.,** and **Zinn, B.** (2004). Open loop control of severe combustion instabilities by fuel flow modulation at non resonant frequencies. In *42nd AIAA Aerospace Sciences Meeting and Exhibit* (p. 634).

123. **Lubarsky, E., Shcherbik, D., Zinn, B., McManus, K., Fric, T.,** and **Srinivasan, S.** (2003). Active control of combustion oscillations by non-coherent fuel flow modulation. In *9th AIAA/CEAS Aeroacoustics Conference and Exhibit* (p. 3180).

124. **Luque, B., Lacasa, L., Ballesteros, F.,** and **Luque, J.** (2009). Horizontal visibility graphs: Exact results for random time series. *Physical Review E*, **80**(4), 046103.

125. **Macquisten, M. A.,** and **Dowling, A. P.** (1993). Low-frequency combustion oscillations in a model afterburner. *Combustion and flame*, **94**(3), 253-264.

126. **Macquisten, M.,** and **Dowling, A. P.** (1995). Combustion oscillations in a twin-stream afterburner. In *15th Aeroacoustics Conference* (p. 4392).

127. **Malik, N., Bookhagen, B., Marwan, N.,** and **Kurths, J**. (2012) Analysis of spatial and temporal extreme monsoonal rainfall over South Asia using complex networks. *Climate dynamics*, **39**(3-4), 971-987.

128. **Mariappan, S., Schmid, P.** and **Sujith, R. I.,** (2010). Role of transient growth in subcritical transition to thermoacoustic instability in a horizontal Rijke tube. In *16th AIAA/CEAS Aeroacoustics Conference* (p. 3857).

129. **Matveev, K. I.** (2003). *Thermoacoustic instabilities in the Rijke tube: experiments and modeling* (Ph.D. thesis, California Institute of Technology).

130. **McManus, K. R., Poinsot, T.,** and **Candel, S. M.** (1993) A review of active control of combustion instabilities. *Progress in energy and combustion science*, **19**(1), 1-29.

131. **Mitchell, C. E., Crocco, L.,** and **Sirignano, W. A.** (1969). Nonlinear longitudinal instability in rocket motors with concentrated combustion. *Combustion Science and Technology*, **1**(1), 35-64.

132. **Molkenthin, N., Rehfeld, K., Marwan, N.,** and **Kurths, J.** (2014) Networks from flows-from dynamics to topology. *Scientific reports*, **4**, 4119.

133. **Monasson, R.** (1999). Diffusion, localization and dispersion relations on "small-world" lattices. *The European Physical Journal B-Condensed Matter and Complex Systems*, **12**(4), 555-567.

134. **Mondal, S., Unni, V. R.,** and **Sujith, R. I.** (2017) Onset of thermoacoustic instability in turbulent combustors: an emergence of synchronized periodicity through formation of chimera-like states. *Journal of Fluid Mechanics*, **811**, 659-681.

135. **Montroll, E. W.,** and **Shlesinger, M. F.** (1982). On 1/f noise and other distributions with long tails. *Proceedings of the National Academy of Sciences*, **79**(10), 3380-3383.

136. **Murayama, S., Kinugawa, H., Tokuda, I. T.,** and **Gotoda, H.** (2018). Characterization and detection of thermoacoustic combustion oscillations based on statistical complexity and complex-network theory. *Physical Review E*, **97**(2), 022223.

137. **Murugesan, M.,** and **Sujith, R. I.** (2015) Combustion noise is scale-free: transition from scale-free to order at the onset of thermoacoustic instability. *Journal of Fluid Mechanics*, **772**, 225-245.

138. **Murugesan, M.,** and **Sujith, R. I.** (2016). Detecting the onset of an impending thermoacoustic instability using complex networks. *Journal of Propulsion and Power*, **32**(1), 707-712.

139. **Nair, V.,** and **Sujith, R. I.** (2013). Identifying homoclinic orbits in the dynamics of intermittent signals through recurrence quantification. *Chaos: An Interdisciplinary Journal of Nonlinear Science*, **23**(3), 033136.

140. **Nair, V.,** and **Sujith, R. I.** (2014). Multifractality in combustion noise: predicting an impending combustion instability. *Journal of Fluid Mechanics*, **747**, 635-655.

141. **Nair, V., Thampi, G.,** and **Sujith, R. I.** (2014) Intermittency route to thermoacoustic instability in turbulent combustors. *Journal of Fluid Mechanics*, **756**, 470-487.

142. **Nair, V., Thampi, G., Karuppusamy, S., Gopalan, S.,** and **Sujith, R. I.** (2013) Loss of chaos in combustion noise as a precursor of impending combustion instability. *International journal of spray and combustion dynamics*, **5**(4), 273-290.

143. **Nair, V., Thampi, G., Sulochana, K., Sarvana, G.,** and **Sujith, R. I.** (2012). System and method for predetermining the onset of impending oscillatory instabilities in practical devices. *Provisional patent, filed Oct*, *1*.

144. **Newman, M. E.** (2000). Models of the small world. *Journal of Statistical Physics*, **101**(3-4), 819-841.

145. **Newman, M. E.** (2003). The structure and function of complex networks. *SIAM review*, **45**(2), 167-256.

146. **Newman, M. E.** (2006). Modularity and community structure in networks. *Proceedings of the national academy of sciences*, **103**(23), 8577-8582.

147. **Newman, M. E.** *Networks*. Oxford university press, 2010.

148. **Nicosia, V., Tang, J., Musolesi, M., Russo, G., Mascolo, C.,** and **Latora, V.** (2012). Components in time-varying graphs. *Chaos: An interdisciplinary journal of nonlinear science*, **22**(2), 023101.

149. **Nicoud, F., Benoit, L., Sensiau, C.,** and **Poinsot, T.** (2007). Acoustic modes in combustors with complex impedances and multidimensional active flames. *AIAA journal*, **45**(2), 426-441.

150. **Noiray, N.,** and **Schuermans, B.** (2013*a*). Deterministic quantities characterizing noise driven Hopf bifurcations in gas turbine combustors. *International Journal of Non-Linear Mechanics*, **50**, 152-163.

151. **Noiray, N.,** and **Schuermans, B.** (2013*b*). On the dynamic nature of azimuthal thermoacoustic modes in annular gas turbine combustion chambers. *Proc. R. Soc. A*, **469**(2151), 20120535.

152. **Noiray, N., Durox, D., Schuller, T.,** and **Candel, S.** (2006). Self-induced instabilities of premixed flames in a multiple injection configuration. *Combustion and flame*, **145**(3), 435-446.

153. **Noiray, N., Durox, D., Schuller, T.,** and **Candel, S.** (2007). Passive control of combustion instabilities involving premixed flames anchored on perforated plates. *Proceedings of the Combustion Institute*, **31**(1), 1283-1290.

154. **Noiray, N., Durox, D., Schuller, T.,** and **Candel, S.** (2008). A unified framework for nonlinear combustion instability analysis based on the flame describing function. *Journal of Fluid Mechanics*, **615**, 139-167.

155. **Noiray, N., Durox, D., Schuller, T.,** and **Candel, S.** (2009). Dynamic phase converter for passive control of combustion instabilities. *Proceedings of the Combustion Institute*, **32**(2), 3163-3170.

156. **Nori, V.,** and **Seitzman, J.** (2008). Evaluation of chemiluminescence as a combustion diagnostic under varying operating conditions. In *46th AIAA Aerospace Sciences Meeting and Exhibit* (p. 953).

157. **O'Connor, J., Acharya, V.,** and **Lieuwen, T. C.** (2015). Transverse combustion instabilities: Acoustic, fluid mechanic, and flame processes. *Progress in Energy and Combustion Science*, **49**, 1-39.

158. **Oefelein, J. C.,** and **Yang, V.** (1993). Comprehensive review of liquid-propellant combustion instabilities in F-1 engines. *Journal of Propulsion and Power*, **9**(5), 657-677.

159. **Okuno, Y., Small, M.,** and **Gotoda, H.** (2015) Dynamics of self-excited thermoacoustic instability in a combustion system: Pseudo-periodic and high-dimensional nature. *Chaos: An Interdisciplinary Journal of Nonlinear Science*, **25**(4), 043107.

160. **Orchini, A., Illingworth, S. J.,** and **Juniper, M. P.** (2015). Frequency domain and time domain analysis of thermoacoustic oscillations with wave-based acoustics. *Journal of Fluid Mechanics*, **775**, 387-414.

161. **Paschereit, C. O.,** and **Gutmark, E.** (2006). Control of high-frequency thermoacoustic pulsations by distributed vortex generators. *AIAA journal*, **44**(3), 550-557.

162. **Paschereit, C. O.,** and **Polifke, W.** (1998). Investigation of the thermoacoustic characteristics of a lean premixed gas turbine burner. In *ASME 1998 International Gas Turbine and Aeroengine Congress and Exhibition* (pp. V003T06A057-V003T06A057). American Society of Mechanical Engineers.

163. **Paschereit, C. O., Flohr, P.,** and **Gutmark, E. J.** (2006). Combustion control by vortex breakdown stabilization. *Journal of turbomachinery*, **128**(4), 679-688.

164. **Paschereit, C. O., Gutmark, E.,** and **Weisenstein, W.** (1998). Structure and control of thermoacoustic instabilities in a gas-turbine combustor. *Combustion Science and Technology*, **138**(1-6), 213-232.

165. **Paschereit, C. O., Gutmark, E.,** and **Weisenstein, W.** (1999). Coherent structures in swirling flows and their role in acoustic combustion control. *Physics of Fluids*, **11**(9), 2667-2678.

166. **Paschereit, C. O., Gutmark, E.,** and **Weisenstein, W.** (2000). Excitation of thermoacoustic instabilities by interaction of acoustics and unstable swirling flow. *AIAA journal*, **38**(6), 1025-1034.

167. **Paschereit, C. O., Schuermans, B., Polifke, W.,** and **Mattson, O.** (1999). Measurement of transfer matrices and source terms of premixed flames. In *ASME 1999 International Gas Turbine and Aeroengine Congress and Exhibition* (pp. V002T02A025-V002T02A025). American Society of Mechanical Engineers.

168. **Pastor-Satorras, R.,** and **Vespignani, A.** (2001). Epidemic spreading in scale-free networks. *Physical review letters*, **86**(14), 3200.

169. **Pawar, S. A.,** and **Sujith**, **R. I.** (2018) Transition to thermoacoustic instability in a turbulent combustor. Journal of the Combustion Society of Japan, **60**(192), 99-111.

170. **Pawar, S. A., Mondal, S., George, N. B.,** and **Sujith, R. I.** (2018). Synchronization behaviour during the dynamical transition in swirl-stabilized combustor: temporal and spatiotemporal analysis. In *2018 AIAA Aerospace Sciences Meeting* (p. 0394).

171. **Pawar, S. A., Seshadri, A., Unni, V. R.,** and **Sujith, R. I.** (2017) Thermoacoustic instability as mutual synchronization between the acoustic field of the confinement and turbulent reactive flow. *Journal of Fluid Mechanics*, **827**, 664-693.

172. **Peracchio, A. A.,** and **Proscia, W. M.** (1998). Nonlinear heat-release/acoustic model for thermoacoustic instability in lean premixed combustors. In *ASME 1998 International Gas Turbine and Aeroengine Congress and Exhibition* (pp. V003T06A022-V003T06A022). American Society of Mechanical Engineers.

173. *Perry, L*. and **J. R. Blackshear** (1993). Driving standing wave by heat addition. *Fourth International Symposium on Combustion. The Williams and Wilkins Company, Baltimore,* 553.

174. **Poinsot, T. J., Trouve, A. C., Veynante, D. P., Candel, S. M.,** and **Esposito, E. J.** (1987) Vortex-driven acoustically coupled combustion instabilities. *Journal of fluid mechanics*, **177**, 265-292.

175. **Pope, S. B.** *Turbulent flows*. Cambridge University Press, 2000.

176. **Putnam, A. A.** *Combustion driven oscillations in industry*. Elsevier Publishing Company, 1971.

177. **Quiroga, R. Q., Kreuz, T.,** and **Grassberger, P.** (2002). Event synchronization: a simple and fast method to measure synchronicity and time delay patterns. *Physical review E*, **66**(4), 041904.

178. **Raffel, M., Willert, C. E.,** and **Kompenhans, J**. *Particle image velocimetry: a practical guide*. Springer Science & Business Media, 2007.

179. **Rajaram, R.,** and **Lieuwen, T.** (2009). Acoustic radiation from turbulent premixed flames. *Journal of Fluid Mechanics*, **637**, 357-385.

180. **Rayleigh, J. W. S.** (1878). The explanation of certain acoustical phenomena. *Nature*, **18** (455), 319-321.

181. **Renard, P. H., Thevenin, D., Rolon, J. C.,** and **Candel, S.** (2000). Dynamics of flame/vortex interactions. *Progress in energy and combustion science*, **26**(3), 225-282.

182. **Richards, G. A.,** and **Janus, M. C.** (1997). Characterization of oscillations during premix gas turbine combustion. In *ASME 1997 International Gas Turbine and Aeroengine Congress and Exhibition* (pp. V002T06A033-V002T06A033). American Society of Mechanical Engineers.

183. **Richards, G. A., Janus, M.,** and **Robey, E. H.** (1999). Control of flame oscillations with equivalence ratio modulation. *Journal of Propulsion and Power*, **15**(2), 232-240.

184. **Rienstra, S. W.,** and **Hirschberg, A.** *An introduction to acoustics*. Eindhoven University of Technology, 2003.

185. **Rijke, P. L.** (1859). LXXI. Notice of a new method of causing a vibration of the air contained in a tube open at both ends. *The London, Edinburgh, and Dublin Philosophical Magazine and Journal of Science*, **17**(116), 419-422.

186. **Rogers, D. E.** and **Marble F. E.** (1956) A mechanism for high-frequency oscillation in ramjet combustors and afterburners. *Journal of Jet Propulsion*, **26**(6), 456-462.

187. **Roux, S., Lartigue, G., Poinsot, T., Meier, U.,** and **Bérat, C.** (2005). Studies of mean and unsteady flow in a swirled combustor using experiments, acoustic analysis, and large eddy simulations. *Combustion and Flame*, **141**(1-2), 40-54.

188. **Russo, L., Russo, P.,** and **Siettos, C. I.** (2016). A complex network theory approach for the spatial distribution of fire breaks in heterogeneous forest landscapes for the control of wildland fires. *PloS one*, **11**(10), e0163226.

189. **Pawar, S. A,** and **Sujith, R. I.** (2018) Transition to Thermoacoustic Instability in a Turbulent Combustor. *Journal of the Combustion Society of Japan*, **60**, 192, 99 – 111.

190. **Samarasinghe, J., Culler, W., Quay, B. D., Santavicca, D. A**., and **O'connor, J.** (2017). The effect of fuel staging on the structure and instability characteristics of swirl-stabilized flames in a lean premixed multinozzle can combustor. *Journal of Engineering for Gas Turbines and Power*, **139**(12), 121504.

191. **Sampath, R.,** and **Chakravarthy, S. R.** (2016). Investigation of intermittent oscillations in a premixed dump combustor using time-resolved particle image velocimetry. *Combustion and Flame*, **172**, 309-325.

192. **Sattelmayer, T.** (2003). Influence of the combustor aerodynamics on combustion instabilities from equivalence ratio fluctuations. *Journal of Engineering for Gas Turbines and Power*, **125**(1), 11-19.

193. **Scarsoglio, S., Iacobello, G.,** and **Ridolfi, L.** (2016) Complex networks unveiling spatial patterns in turbulence. *International Journal of Bifurcation and Chaos*, **26**(13), 1650223.

194. **Schadow K. C., Gutmark E., Wilson K. J**. and **Smith R. A.** (1990) Multistep dump combustor design to reduce combustion instabilities, *Journal of Propulsion and Power*, **6**(4), 407-411.

195. **Schadow, K. C.,** and **Gutmark, E.** (1992) Combustion instability related to vortex shedding in dump combustors and their passive control. *Progress in Energy and Combustion Science*, **18**(2), 117-132.

196. **Schadow, K. C., Gutmark, E., Parr, T. P., Parr, D. M., Wilson, K. J.,** and **Crump, J. E.** (1989). Large-scale coherent structures as drivers of combustion instability. *Combustion science and technology*, **64**(4-6), 167-186.

197. **Schuermans, B. B. H., Polifke, W.,** and **Paschereit, C. O.** (2000). Prediction of Acoustic Pressure Spectra in Gas Turbines based on Measured Transfer Matrices. In *International Gas Turbine and Aeroengine Congress and Exposition*.

198. **Schuller, T., Durox, D.,** and **Candel, S.** (2003). A unified model for the prediction of laminar flame transfer functions: comparisons between conical and V-flame dynamics. *Combustion and Flame*, **134**(1-2), 21-34.

199. **Schwing, J., Sattelmayer, T.,** and **Noiray, N.** (2011) Interaction of vortex shedding and transverse high-frequency pressure oscillations in a tubular combustion chamber. In *ASME 2011 Turbo Expo: Turbine Technical Conference and Exposition* (pp. 259-268). American Society of Mechanical Engineers.

200. **Seshadri, A., Nair, V.,** and **Sujith, R. I.** (2016). A reduced-order deterministic model describing an intermittency route to combustion instability. *Combustion Theory and Modelling*, **20**(3), 441-456.

201. **Shanbhogue, S. J.** (2008) *Dynamics of perturbed exothermic bluff-body flow-fields* (Doctoral dissertation, Georgia Institute of Technology).

202. **Shlesinger, M. F.** (1987). Fractal time and 1/f noise in complex systems. *Annals of the New York Academy of Sciences*, **504**(1), 214-228.

203. **Singh, J., Belur Vishwanath, R., Chaudhuri, S.,** and **Sujith, R. I.** (2017) Network structure of turbulent premixed flames. *Chaos: An Interdisciplinary Journal of Nonlinear Science*, **27**(4), 043107.

204. **Sirignano, W. A.** (2015). Driving mechanisms for combustion instability. *Combustion Science and Technology*, **187**(1-2), 162-205.

205. **Sivashinsky, G. I.** (1988). Nonlinear analysis of hydrodynamic instability in laminar flames—I. Derivation of basic equations. In *Dynamics of Curved Fronts* (pp. 459-488).

206. **Smith, D. A.** and **Zukoski, E.** (1985) Combustion instability sustained by unsteady vortex combustion. In *21st Joint Propulsion Conference* (p. 1248).

207. **Sondhauss, C.** (1850). Über die Schallschwingungen der Luft in erhitzten Glasröhren und in gedeckten Pfeifen von ungleicher Weite. *Annalen der Physik*, **155**(1), 1-34.

208. **Sporns, O.** *Networks of the Brain*. MIT press, 2010.

209. **Sreenivasan, K**. (1991). Fractals and multifractals in fluid turbulence. *Annual Review of Fluid Mechanics*, **23**(1), 539-604.

210. **Steele, R. C., Cowell, L. H., Cannon, S. M.,** and **Smith, C. E.** (1999). Passive control of combustion instability in lean premixed combustors. In *ASME International Gas Turbine and Aeroengine Congress and Exhibition* (pp. V002T02A004-V002T02A004). American Society of Mechanical Engineers.

211. **Steinberg, A. M., Boxx, I., Stöhr, M., Carter, C. D.,** and **Meier, W.** (2010). Flow–flame interactions causing acoustically coupled heat release fluctuations in a thermo-acoustically unstable gas turbine model combustor. *Combustion and Flame*, **157**(12), 2250-2266.

212. **Sterling, J. D.** (1993). Nonlinear analysis and modelling of combustion instabilities in a laboratory combustor. *Combustion Science and Technology*, **89**(1-4), 167-179.

213. **Strahle, W. C.** (1971). On combustion generated noise. *Journal of Fluid Mechanics*, **49**(2), 399-414.

214. **Strogatz, S. H**. (2001) Exploring complex networks. *Nature*, **410**(6825), 268.

215. **Strogatz, S. H.** *Nonlinear dynamics and chaos: with applications to physics, biology, chemistry, and engineering*. Perseus Books Group, 1994.

216. **Subramanian, P.,** and **Sujith, R. I.** (2011). Non-normality and internal flame dynamics in premixed flame–acoustic interaction. *Journal of Fluid Mechanics*, **679**, 315-342.

217. **Subramanian, P., Sujith, R. I**., and **Wahi, P.** (2013). Subcritical bifurcation and bistability in thermoacoustic systems. *Journal of Fluid Mechanics*, **715**, 210-238.

218. **Sujith, R. I., Juniper, M. P.,** and **Schmid, P. J.** (2016). Non-normality and nonlinearity in thermoacoustic instabilities. *International Journal of Spray and Combustion Dynamics*, **8**(2), 119-146.

219. **Sujith, R. I., Waldherr, G. A., Jagoda, J. I.,** and **Zinn, B. T.** (1997). An experimental investigation of the behavior of droplets in axial acoustic fields. *Journal of vibration and acoustics*, **119**(3), 285-292.

220. **Sujith, R. I., Waldherr, G. A., Jagoda, J. I.,** and **Zinn, B. T.** (2000). Experimental investigation of the evaporation of droplets in axial acoustic fields. *Journal of Propulsion and Power*, **16**(2), 278-285.

221. **Surendran, A., Heckl, M. A., Hosseini, N.,** and **Teerling, O. J.** (2017). Passive control of instabilities in combustion systems with heat exchanger. *International Journal of Spray and Combustion Dynamics*, 1756827717731486.

222. **Suresh, S.** *Fatigue of materials*. Cambridge university press, 1998.

223. **Taira, K., Nair, A. G.,** and **Brunton, S. L.** (2016) Network structure of two-dimensional decaying isotropic turbulence. *Journal of Fluid Mechanics*, *795*.

224. **Takens, F.** Detecting strange attractors in turbulence. In *Dynamical systems and turbulence, Warwick 1980* (pp. 366-381). Springer, Berlin, Heidelberg, 1981.

225. **Tang, J. K.** (2012). *Temporal network metrics and their application to real world networks* (Doctoral dissertation, University of Cambridge).

226. **Tang, J., Scellato, S., Musolesi, M., Mascolo, C.,** and **Latora, V.** (2010) Small-world behavior in time-varying graphs. *Physical Review E*, **81**(5), 055101.

227. **Tennekes, H.,** and **Lumley, J. L.** *A first course in turbulence*. MIT press, 1972.

228. **Tong, A. Y.,** and **Sirignano, W. A.** (1989). Oscillatory vaporization of fuel droplets in an unstable combustor. *Journal of Propulsion and Power*, **5**(3), 257-261.

229. **Tony, J., Gopalakrishnan, E. A., Sreelekha, E**., and **Sujith, R. I.** (2015) Detecting deterministic nature of pressure measurements from a turbulent combustor. *Physical Review E*, **92**(6), 062902.

230. **Tsonis, A. A.,** and **Roebber, P. J.** (2004). The architecture of the climate network. *Physica A: Statistical Mechanics and its Applications*, **333**, 497-504.

231. **Tung, T. Q., Ryu, T., Lee, K. H.,** and **Lee, D.** (2007). Inferring gene regulatory networks from microarray time series data using transfer entropy. In *Computer-Based Medical Systems, 2007. CBMS'07. Twentieth IEEE International Symposium on* (pp. 383-388). IEEE.

232. **Tupikina, L., Molkenthin, N., López, C., Hernández-García, E., Marwan, N.** and **Kurths, J.,** 2016. Correlation networks from flows. The case of forced and time-dependent advection-diffusion dynamics. *PloS One*, **11**(4), p.e0153703.

233. **Unni, V. R.,** and **Sujith, R. I.** (2015) Multifractal characteristics of combustor dynamics close to lean blowout. *Journal of Fluid Mechanics*, **784**, 30-50.

234. **Unni, V. R.,** and **Sujith, R. I.** (2017) Flame dynamics during intermittency in a turbulent combustor. *Proceedings of the Combustion Institute*, **36**(3), 3791-3798.

235. **Unni, V. R., Mukhopadhyay, A.,** and **Sujith, R. I.** (2015). Online detection of impending instability in a combustion system using tools from symbolic time series analysis. *International Journal of Spray and Combustion Dynamics*, **7**(3), 243-255.

236. **Urbano, A., Selle, L., Staffelbach, G., Cuenot, B., Schmitt, T., Ducruix, S**., and **Candel, S.** (2016). Exploration of combustion instability triggering using large eddy simulation of a multiple injector liquid rocket engine. *Combustion and Flame*, **169**, 129-140.

237. **Valencia, M., Martinerie, J., Dupont, S.,** and **Chavez, M.** (2008) Dynamic small-world behavior in functional brain networks unveiled by an event-related networks approach. *Physical Review E*, **77**(5), 050905.

238. **Venkataraman, K. K.** (2001). An investigation of the acoustic instability mechanism in lean premixed dump combustors. *Ph.D. Thesis*, Department of Mechanical Engineering, the Pennsylvania State University, University Park, PA.

239. **Venkataraman, K. K., Preston, L. H., Simons, D. W., Lee, B. J., Lee, J. G.,** and **Santavicca, D. A.** (1999). Mechanism of combustion instability in a lean premixed dump combustor. *Journal of Propulsion and Power*, **15**(6), 909-918.

240. **Wasserman, S.,** and **Katherine, F.** *Social network analysis: Methods and applications*. Cambridge university press, 1994.

241. **Watts, D. J.,** and **Strogatz, S. H.** (1998) Collective dynamics of 'small-world' networks. *Nature*, **393**(6684), 440.

242. **Waugh, I. C.,** and **Juniper, M. P.** (2011). Triggering in a thermoacoustic system with stochastic noise. *International journal of spray and combustion dynamics*, **3**(3), 225-241.

243. **Waugh, I., Geuß, M.,** and **Juniper, M.** (2011). Triggering, bypass transition and the effect of noise on a linearly stable thermoacoustic system. *Proceedings of the Combustion Institute*, **33**(2), 2945-2952.

244. **Weber, J. K.,** and **Pande, V. S.** (2015). Percolation-like phase transitions in network models of protein dynamics. *The Journal of chemical physics*, **142**(21), 06B607_1.

245. **Wicker, J. M., Greene, W. D., Kim, S. I.,** and **Yang, V**. (1996). Triggering of longitudinal combustion instabilities in rocket motors-nonlinear combustion response. *Journal of Propulsion and Power*, **12**(6), 1148-1158.

246. **Wilhite, J. M., Dolan, B. J., Kabiraj, L., Villalva Gomez, R., Gutmark, E. J.,** and **Paschereit, C. O.** (2016). Analysis of combustion oscillations in a staged MLDI burner using decomposition methods and recurrence analysis. In *54th AIAA Aerospace Sciences Meeting* (p. 1156).

247. **Williams, L. J., Meadows, J.,** and **Agrawal, A. K.** (2016). Passive control of thermoacoustic instabilities in swirl-stabilized combustion at elevated pressures. *International Journal of Spray and Combustion Dynamics*, **8**(3), 173-182.

248. **Worth, N. A.,** and **Dawson, J. R.** (2013). Modal dynamics of self-excited azimuthal instabilities in an annular combustion chamber. *Combustion and Flame*, **160**(11), 2476-2489.

249. **Yang, V., Kim, S. I.,** and **Culick, F. E. C.** (1990). Triggering of longitudinal pressure oscillations in combustion chambers. I: nonlinear gas dynamics. *Combustion Science and Technology*, **72**(4-6), 183-214.

250. **Zhang, Y., Zhao, D., Zhang, J., Xiong, R**., and **Gao, W.** (2011) Interpolation-dependent image downsampling. *IEEE Transactions on Image Processing*, **20**(11), 3291-3296.

251. **Zukoski, F. E.** *Afterburners.* Chapter 21. In: Oates G, editor. The aerothermodynamics of aircraft gas turbine engines. Air Force Aero Propulsion Laboratory; 1978.

LIST OF PAPERS BASED ON THESIS

Referred Journals

1. Unni, V. R., **Krishnan, A**., Manikandan, R., George, N. B., Sujith, R. I., Marwan, N., & Kurths, J. (2018) On the emergence of critical regions at the onset of thermoacoustic instability in a turbulent combustor. *Chaos: An Interdisciplinary Journal of Nonlinear Science*, 28(6), 063125.

2. **Krishnan, A.,** Sujith, R. I., Marwan, N., & Kurths, J. On the emergence of large clusters of acoustic power sources at the onset of thermoacoustic instability in a turbulent combustor. *Journal of Fluid Mechanics* (under review).

Conferences

1. **Krishnan, A.,** Sujith, R. I., Marwan, N., & Kurths, J., *Conference on Nonlinear Systems and Dynamics*, JNU, New Delhi, October 11th -14th , 2018.

2. **Krishnan, A.,** & Sujith, R. I., *International Conference on Complex Networks and their Applications*, University of Cambridge, London, U. K, December 11th – 14th, 2018 (Accepted).